Computational Study of Highway Bridges Structural Response Exposed to a Large Fire Exposure

Mohammad Nazmul Hasan Nahid

Dissertation submitted to the faculty of the Virginia Polytechnic Institute and State University in partial fulfillment of the requirements for the degree of

Doctorate of Philosophy

In

Mechanical Engineering

Brian Y. Lattimer

Robert L. West

Thomas E. Diller

Scott T. Huxtable

Elisa D. Sotelino

April 28, 2015

Blacksburg, VA

Keywords: Highway Bridge, Fire, Plate Girder, Tub Girder, Structural Analysis, Coupled Analysis, FDS, ABAQUS

Computational Study of Highway Bridges Structural Response Exposed to a Large Fire Exposure

Mohammad Nazmul Hasan Nahid

ABSTRACT

The exposure from a localized vehicle fire has been observed to produce excessive damage onto highway bridge structural elements including complete collapse of the infrastructure. The occurrence of a fire beneath a bridge can lead to significant economic expense and loss of service even if the bridge does not collapse. The focus of the current research is to assess and evaluate the effect of realistic localized fire exposures from vehicles on the bridge structural integrity and to guide future development of highway bridge design with improved fire resistance.

In this research, the bridge structural element response was predicted through a series of three loosely coupled analyses: fire analysis, thermal analysis, and structural analysis. Two different types of fire modeling methodologies were developed in this research and used to predict the thermo-structural response of bridge structural elements: one to model the non-uniform exposure due to a vehicle fire and another to predict response due to a standard uniform furnace exposure. The vehicle fire scenarios required coupling the computational fluid dynamics (CFD) code Fire Dynamics Simulator (FDS) with Abaqus while the furnace exposure scenarios were all done within Abaqus. Both methodologies were benchmarked against experimental data. Using the developed methodologies, simulations were initially performed to predict the thermo-structural response of a single steel girder-concrete deck composite assembly to different local, non-uniform fires and uniform standard furnace fire exposures. The steel girder-concrete deck composite assembly was selected since it is a common bridge design. Following this, a series of simulations were performed on unprotected highway bridges with multiple steel plate girders and steel tub girders subjected to localized fires. The analyses were used to evaluate the influence of a fire scenario on the bridge element response, identify the factors governing the failure of bridge structural elements subjected to a localized fire exposure, and provide guidance in the design of highway bridge structural elements against fire hazards.

This study demonstrates that girder geometry affected both the dynamics of the fire as well as the heat transfer to the bridge structural elements which resulted in a different structural response for the bridge. A heavy goods vehicle (heat release rate of 200 MW) and tanker fires (heat release rate of 300 MW) were predicted to cause the bridge to fail due to collapse, while smaller fires did not. The geometric features of the plate girders caused the girder elements to be exposed to higher heat fluxes from both sides of the girder resulting in collapse when exposed to a HGV fire. Conversely, the closed feature of the box girder does not allow the interior surfaces to be in direct contact with the flames and are only exposed to the internal reradiation from surfaces inside the girder. As a result, the single and double lane tub girder highway bridge structure does not fail due to a heavy goods vehicle fire exposure.

Dedication

For my parents, brother and sister, you have supported me throughout my entire academic career, from kindergarten before I had any idea of what I could become to this moment which I have dreamt to achieve for so long. And finally for my wife who support me during my final stage. Thank you.

Acknowledgements

I would like to thank everyone at Virginia Tech who has contributed to my education and to this research. In particular, I would like to thank the members of my project, Dr. Brian Lattimer, Dr. William Wright, Dr. Elisa Sotelino for their commitment and their helpful comments and suggestions. I am especially grateful to Dr. Brian Lattimer, who has been a great advisor, mentor and friend over the past few years. He gave me the opportunity to pursue a research topic that was both challenging and interesting, and I am thankful for his advice and continuous support throughout my doctoral education. I also would like to thank the other members of the EXTREME Lab both past and present for your friendship, advice, and the many discussions, both research related and non-research related, to help pass the time and turn this experience into a fruitful one in many ways.

Table of Contents

List of Figures

List of Tables

1 Introduction

1.1 Research Aim

The exposure from a localized vehicle fire has been observed to produce excessive damage onto highway bridge structural elements including complete collapse of the infrastructure. The occurrence of a fire on a bridge can lead to significant economic expense and loss of service even if the bridge does not collapse. It is very difficult to detour the traffic which affects the traffic quality and economics of that region. The focus of this research was to assess and evaluate the effect of localized fire exposures on the bridge structural elements and to guide future development of highway bridge design with improved fire resistance.

Infrastructure during its lifetime is exposed to many severe hazards including fires. Recently, a couple of incidents have occurred where highway bridge structures were severely damaged or collapsed due to fires. According to Battelle [1], the average number of vehicle fire incidents in the U.S. is 376,000 resulting in 570 civilian deaths and $1.28 billion of property losses. In building fires, the growth of the fire may be hindered due to the lack of oxygen. When the fire occurs in the vicinity of a bridge, fires have adequate supply of fuel and oxygen allowing it to grow large increasing the thermal exposure on the bridge. The New York Department of Transportation [2] has created a database documenting 1,746 cases of bridge collapse that have occurred in the U.S. This data has been collected over many years through a combination of state surveys and reviews of information obtained from the media. The majority of collapses occurred from 1960 to the present. The data included many bridge types but most were fabricated from concrete, steel, and timber. The cause of failure was reported in all but one of the incidents as shown in Figure 1-1. In this database, collapse is defined as the bridge being unusable and removed from service. Of the 1,746 collapse events, only 50 were caused by fire. Of these, half were timber bridges in remote locations that were damaged by wildfires or arson. This leaves about 25 cases nationwide where fire has caused permanent loss of the bridge. There are many more cases where fires resulted in no damage or repairable damage. Though this is not many, several recent catastrophic collapses of high use bridges in urban areas have questioned the structural stability of bridges during fires.

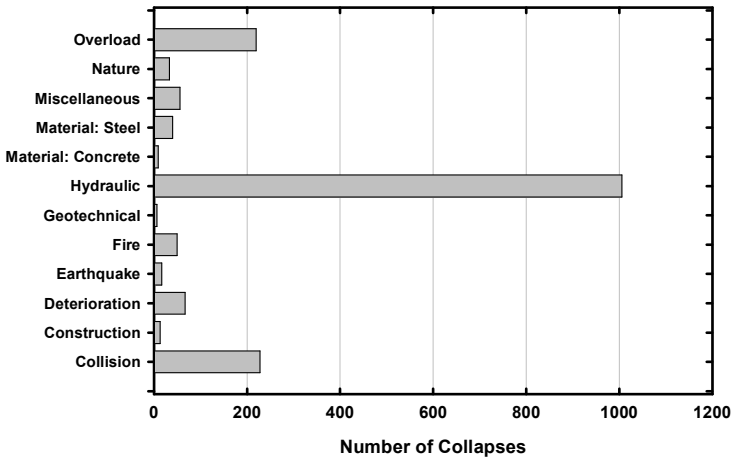

Figure 1-1: NY State database summary showing the cause of collapse [2,3].

A more recent survey conducted as part of NCHRP 12-85 [3], reported 118 significant fire events on bridges. Out of 118 events, only two events caused complete bridge collapse, the McArthur Maze interchange in Oakland, California and the Nine Mile Road Bridge over I-75 in Detroit, Michigan. There were many more cases where bridges were severely damaged and could not be returned to service. From an operational standpoint, a severely damaged bridge that requires replacement is not much different than a complete collapse.

Fire has been completely neglected as one of the primary extreme event limit states in the highway bridge design codes [4]. In AASHTO [5], there are provisions for earthquake loads, wind loads, ship collision, and scour, but no provisions exist to safe guard against fire. The American NFPA 502 [6]: Standard for Road Tunnels, Bridges and other limited access highway states that "Protection of structure –critical structural members shall be protected from collision and high temperature exposure that can result in dangerous weakening or complete collapse of the bridge or elevated highway." However, no guidelines were provided for the design of bridges from fires or high temperature exposure. Similarly, the European fire related structure standards EC-1 part 1-2 [7], EC-2 part 1-2 [8], EC-3 part 1-2 [9] and EC-4 part 1-2 [10] do not provide any guidance for the design of bridge structures against fire.

Highway bridge structures could be exposed to a wide range of fires from a smaller car fire (2-3 MW) to a very large oil tanker fire (300 MW)[11]. Some of these fires are not threatening to the structure while others may result in extreme damage. The localized fire

exposure and openness of the geometry of highway bridges makes it different than the well studied tunnel, car park, and compartment fire exposure. Bridge fire exposures are typically local type fire exposures that are not confined by walls like a building or tunnel. A local fire exposes a portion of the bridge structural elements to flames and the open nature of the fire may also allow the flames to wrap around the bridge. As a result, standard furnace uniform fire exposures developed for more enclosed building and tunnel fires (such as ASTM E119[12]) are not usually used to evaluate the structural fire performance of bridge members. Even though these fires are not confined by walls, local fire exposures onto bridges can be very severe and can exceed the heat exposure levels used in the standard furnace tests. NFPA 502 [6] "Standard for Road Tunnels, Bridges, and Other Limited Access Highways" as well as previous research in this area contains no guidance on evaluating the potential threat of different fires on bridge structural elements. The response of the bridge structural elements to a fire can be determined through large-scale testing or computer simulations. The most common highway bridges used in U.S. are composed of steel girder-concrete deck composite assembly. These bridges have a series of deep steel girders that run along the length of the concrete bridge deck. If a fire occurs underneath the bridge, flames and hot gases will impinge on the concrete deck between two adjacent girders and forced between the girders along the length of the bridge. The confinement of the flame will result in high heat fluxes to girder elements for potentially long distances depending on the size of the fire.

The prediction of the behavior of highway bridge structures subjected to fire loading involves three components: (1) prediction of the localized fire exposure, (2) prediction of the thermal response of the bridge structure during localized fire exposure, and (3) prediction of the structural response of the bridge at elevated temperatures. The majority of research on bridge thermo-structural response during fires has used uniform standard fire exposures [13, 14], while limited work has been performed to evaluate the effects of local fire exposures on bridge collapse [3, 15]. No previous work has focused on simulating the fire dynamics and exposure onto bridges from very large fires that are produced by vehicles and fuel tankers. Thus, a computational study of the structural response of bridges to different local fires with and without structural load is needed. In addition, a fundamental understanding of the fire dynamics and the effects of bridge element design on temperature response of the bridge is needed to improve structural integrity of highway bridges.

The research in this effort focused on predicting the response of steel supported concrete deck highway bridges and proposed designs that improve the bridge structural integrity during a fire. The bridge structural element response was predicted through a series of three loosely coupled analyses: fire analysis, thermal analysis, and structural analysis. Two different types of fire modeling methodologies were developed in this research and used to predict the thermo-structural response of bridge structural elements: one to model the non-uniform exposure due to a vehicle fire and another to predict response due to a standard uniform furnace exposure. The vehicle fire scenarios required coupling the computational fluid dynamics (CFD) code Fire Dynamics Simulator (FDS) with Abaqus while the furnace exposure scenarios were all done within Abaqus. Both methodologies were benchmarked against experimental data. Using the developed methodologies, simulations were initially performed to predict the thermo-structural response of single steel girder-concrete deck composite assemblies to different local, nonuniform fires and uniform standard furnace fire exposures. The steel girder-concrete deck composite assembly was selected since it is the most popular in design in the U.S. and the rest of the world. Following this, a series of simulations were performed on unprotected highway bridges with multiple steel plate girders and steel tub girders subjected to localized fires. The analyses were used to evaluate the influence of fire scenario on the bridge element response, identify the factors governing the failure of bridge structural elements subjected to localized fire exposure, and provide guidance in the design of highway bridge structural elements against fire hazard.

1.2 Research Contributions

This work is presented in the following chapters organized in the form of papers with relevant literature review of each topic included at the beginning of individual chapters. The research contribution in each chapter is provided below:

- Chapter 2 – A new methodology was formulated for modeling fire resistance furnace thermal exposures that accounts for the radiation exchange between surfaces inside of a furnace as well as the convective heat transfer. The methodology was used to predict the temperature rise of unprotected structural elements with temporally and spatially varying temperatures.
- Chapter 3 – A new approach was developed and validated to predict the fire dynamics of fires ranging from small-scale (0.1 m diameter) to large-scale (30 m diameter) using the

CFD code FDS. The methodology was benchmarked against fire and plume gas temperatures and velocities as well as the heat transfer to an object directly adjacent to the fire.

- Chapter 4 – A computational study was conducted to evaluate the effects of non-uniform local vehicle fire exposures on the thermo-structural response of highway bridge structural elements. For this, a modeling approach was developed where FDS was sequentially coupled to Abaqus through a user subroutine allowing for the FDS predicted heat fluxes onto the bridge surfaces to be mapped onto the elements in Abaqus for prediction of the thermal response. These thermal model results in Abaqus were then sequentially coupled to a structural analysis within Abaqus for predicting the structural behavior of the bridge during a local fire. The methodology was used to predict the thermo-structural response of a single unprotected steel girder-concrete deck composite assembly exposed to a range of different size vehicle fires and a tanker fire. Simulation results with a localized fire were compared with thermo-structural behavior predicted due to a uniform standard furnace exposure.
- Chapter 5 – A computational study was performed to assess improving the bridge structural integrity and preventing failure through modifying the structural steel design to limit the temperature rise of the structure. The approach to improving the design was to modify the structural design so that the fire dynamics change in a way that reduces the overall thermal exposure and limits the surface area of heat transfer. The study included a comparison of typical steel plate girders, a new tub girder design, and steel plate girders with a flame deflector.

1.3 References

[1] Battelle, "Comparative risks of hazarsdous materials and non-hazardous materials truck shipment accidents/incidents," Federal Motor Carrier Safety Administration, Washington D.C. (USA)2004.

[2] New York State Department of Transportation, "Bridge fire incidents in New York state," New York State Department of Transportation, USA 2008.

[3] W. Wright, B. Lattimer, M. Woodworth, M. Nahid, and E. Sotelino, "NCHRP Project No. 12-85: Highway Bridge Fire Hazard Assessment," Transportation Research Board of the National Academies, Washington DC,2013.

[4] M. Ghosn, F. Moses, and J. Wang, *Design of highway bridges for extreme events*: Transportation Research Board, 2003.

[5] AASHTO, "Load and Resistance Factor Design (LRFD) Bridge Design Specifications: Customary U.S. Units," AASHTO, Washington D.C.2008.
[6] N. F. P. Association, *NFPA 502, Standard for Road Tunnels, Bridges, and Other Limited Access Highways*: NFPA, 2010.
[7] European Committee for standardization (CEN), "Eurocode 1 Actions on structures, part 1-2: general actions - actions on structures exposed to fire," Brussels (Belgium): CEN,2003.
[8] European Committee for standardization (CEN), "Eurocode 2: Design of concrete structures - part 1-2: general rules - structural fire design," Brussels (Belgium): CEN2004.
[9] European Committee for standardization (CEN), "Eurocode 3: Design of steel structures - part 1-2: general rules - structural fire design," Brussels (Belgium): CEN2005.
[10] European Committee for standardization (CEN), "Eurocode 4: Design of composite steel and concrete structures - part 1-2: general rules - structural fire design," Brussels (Belgium): CEN2005.
[11] V. Babrauskas, "Heat release rates," *SFPE handbook of fire protection engineering,* vol. 3, pp. 3-1, 2002.
[12] ASTM, "E119: Standard Test Methods for Fire Tests of Building Construction and Materials," American Society for Testing and Materials: Philadelphia, PA.1995.
[13] V. Kodur, E. Aziz, and M. Dwaikat, "Evaluating fire resistance of steel girders in bridges," *Journal of Bridge Engineering,* vol. 18, pp. 633-643, 2012.
[14] I. Payá-Zaforteza and M. Garlock, "A numerical investigation on the fire response of a steel girder bridge," *Journal of Constructional Steel Research,* vol. 75, pp. 93-103, 2012.
[15] J. Alos-Moya, I. Paya-Zaforteza, M. Garlock, E. Loma-Ossorio, D. Schiffner, and A. Hospitaler, "Analysis of a bridge failure due to fire using computational fluid dynamics and finite element models," *Engineering Structures,* vol. 68, pp. 96-110, 2014.

2 Modeling Thermal Response of Steel-Concrete Floor Systems in a Furnace

[publication information: Nahid, M. & Lattimer, B.Y. (2014). Modeling thermal response of steel-concrete floor systems in a furnace. Fire Safety Journal, 68, 100-108]

2.1 Introduction

Standard time-temperature exposures inside furnaces are used to assess the fire resistance of structural elements. The fire resistance of structural elements is defined by the ability of the element to maintain structural integrity and prevent heat transmission through the assembly. The loss of structural integrity of an element is typically evaluated based on the element not exceeding a critical temperature without structural load applied [1]. For example, UL 1709 [2] requires that steel columns not exceed 500^{o}C, which is the approximate temperature at which there is a 50% reduction in mechanical properties. In addition, there have been several research based experimental studies where structural load is applied to elements during a furnace exposure to justify the use of the critical temperatures as well as provide benchmark data for thermo-structural models. Due to mechanical properties and thermal expansion varying with temperature, it is important to accurately predict the temperature rise of structural elements to support evaluating the behavior in a standard furnace test as well as predicting the thermo-structural response.

The standardized furnace exposures vary by the type of time-temperature curve prescribed. Examples include the cellulosic fire curves (ISO 834 [3], ASTM E119 [4]) as well as the more severe hydrocarbon pool fire exposures (UL 1709 [2], EC3 part1-2 [5]). Despite following the same time-temperature curve, the furnace exposure may be affected by the furnace temperature measurement technique (e.g., thermocouple, plate thermometer), furnace lining material, burner fuel, burner location relative to sample, furnace size and aspect ratio, and furnace orientation. Sultan [6-9] has performed numerous experiments quantifying the exposure from different furnaces. For gas fired furnaces lined with lower density insulation and an insulating surface at the sample location, similar heat fluxes were measured from the furnace environment independent of the furnace measurement technique or furnace size. (Cooke [10], Sultan [8]). Test specimens made of concrete and steel may thermally lag the furnace environment, which has been reported to impact the furnace temperature measurements made using thermocouples that have a view of the test specimen [11]. Plate thermometers are being

widely used to measure the furnace temperature to reduce the sample radiation effects on the furnace temperature measurement.

There are several techniques used to model the furnace exposure. A furnace environment produces mixed mode heat transfer including both convection and radiation. In general, convection is modeled using a fixed convective heat transfer coefficient with a value of 25 W/m^2-K for a cellulosic exposure and 50 W/m^2-K for a hydrocarbon pool fire exposure [1]. A wider variety of methods have been used to predict the radiation exchange inside of a furnace. Sultan and Harmathy [6, 7] developed an analytical model that included surface radiation exchange as well as gas radiation and attenuation effects. They used this model to explore the effects of fuel type and furnace geometry on the thermal exposure to a test specimen. Ghojel [12, 13] developed a model that included only gas radiation and attenuation effects for compartment fires without including surface radiation exchange. This model was used by Cedeno et al. [14] to predict the furnace exposure to floor assemblies. In furnaces with complete combustion burners, the gas emissivity is low thus reducing the effect of gas radiation and attenuation and increasing the effect of radiation exchange (Sultan [8, 9], Nahid [15]). For test specimens such as floor assemblies (I-beams beneath a concrete slab) where the test specimen can exchange radiation with itself, including surface radiation exchange becomes important. Numerous researchers [16-20] have accounted for this complex radiation exchange by specifying an effective emissivity to provide the best agreement between data and the model. For I-beams, a correction for the radiation exchange was developed using the "shadow effect" parameter (Wickstrom [11], Eurocode [5]). The "shadow effect" parameter is applied in models where the section is of uniform temperature, which is commonly not the case due to the change in cross-section thickness as well as interaction with other materials (i.e., concrete and steel).

A new furnace exposure modeling methodology is provided in this paper that accounts for the radiation exchange between surfaces inside of a furnace as well as the convective heat transfer. The predicted heat transfer to an insulated specimen is compared with available furnace data to demonstrate the ability of the model to account for furnace construction, furnace size, and time-temperature curve. The methodology is then used to predict the temperature rise of unprotected structural elements with spatially varying temperatures and compared with data.

2.2 Furnace Modeling

2.2.1 Approach

A surface radiation exchange modeling approach was developed to predict the thermal exposure from a fire resistance furnace environment onto a structural element specimen. This model is based on the radiation exchange between surfaces inside the furnace including between the furnace walls and the test specimen as well as the test specimen and itself. The furnace exposure is invoked in the model through defining the furnace wall temperature as the furnace time-temperature curve. In addition, the model does not include the attenuation of radiation between surfaces inside of the furnace due to the combustion gases inside the furnace.

The motivation for defining the wall temperature as the furnace time-temperature curve is based on experimental data from insulated furnace tests with gas burners where the wall temperatures inside the furnace were measured to agree with the time-temperature curve (Lattimer et al [21], Sultan [8, 9], Cooke[10]) after the initial 5-10 minutes of exposure. This occurs due to the insulating surface trapping the heat at the surface causing the surface temperature to be nearly equal to the gas temperature. Through the work of Sultan [7] in gas fired furnaces, heat fluxes were not measured to be affected by changing the wall boundaries from fire insulation brick to fire insulation blanket, which is the construction of most modern furnaces. Use of higher density brick materials on the interior of the furnace walls than those tested by Sultan [7, 9] may cause the wall temperatures to lag the furnace environment. As a result, this method may not be appropriate for those types of furnaces and more detailed modeling of the wall temperature rise with time may be required.

Modern furnaces commonly use clean burning, gas (such as natural gas or propane) burners to generate the furnace exposure though oil-fired burners are still in use. Gas burner fired furnaces were reported to have low gas emissivities of 0.1 – 0.2 [Sultan [6, 7], Nahid [15]], while oil-fired furnaces were stated to have a higher gas emissivity 0.3 Sultan [7]. Nahid [15] investigated the effects of combustion gas attenuation on radiation exchange between surfaces inside a furnace environment. In this work, a three surface enclosure model was developed including both radiation exchange and gas attenuation effects as well as convection on the inside of the enclosure. One surface was insulation to represent the furnace environment while the other two surfaces were steel and concrete to represent a test specimen. The insulation and gas

temperature were defined as the ISO 834 time-temperature furnace exposure while thermal predictions were performed to determine the concrete and steel temperature rise. Variation of the gas emissivity was predicted to have an impact on the steel and concrete temperatures, with the largest effect being on the steel temperature rise. Steel temperature rise is shown in Figure 2-1 for steel height to concrete width ratios of 0.1 and 10. As seen in these plots, furnaces having a gas emissivity of less than 0.3 will have a 3-10% error in the specimen temperature calculation if the radiation attenuation is neglected (i.e., emissivity of 0.0). The effect of gas emissivity on steel temperature rise is dependent on the steel height to concrete width ratio, with the lower ratio case (i.e., smaller steel beam heights relative to the concrete width) being more sensitive to the gas attenuation. This is expected since increasing the concrete width will increase the view factor between the steel and the concrete, resulting in lower temperatures. The result indicates that gas attenuation effects inside of the furnace can be ignored with minimal error on the temperature rise calculations.

The furnace exposure model was implemented into the commercial finite element software Abaqus 6.10-EF1 [22]. To implement this model, a box was constructed in the modeling framework. Five sides of the box represent the walls of the furnace while the other wall is where the test specimen is located. The five furnace walls are assigned the desired time-temperature furnace exposure while a three-dimensional analysis was performed on test specimen. The model included radiation exchange interactions and convection on the inside with the gas temperature for convection given as the time-temperature furnace exposure. The test specimen unexposed surface boundary conditions were radiation and convection loss to ambient.

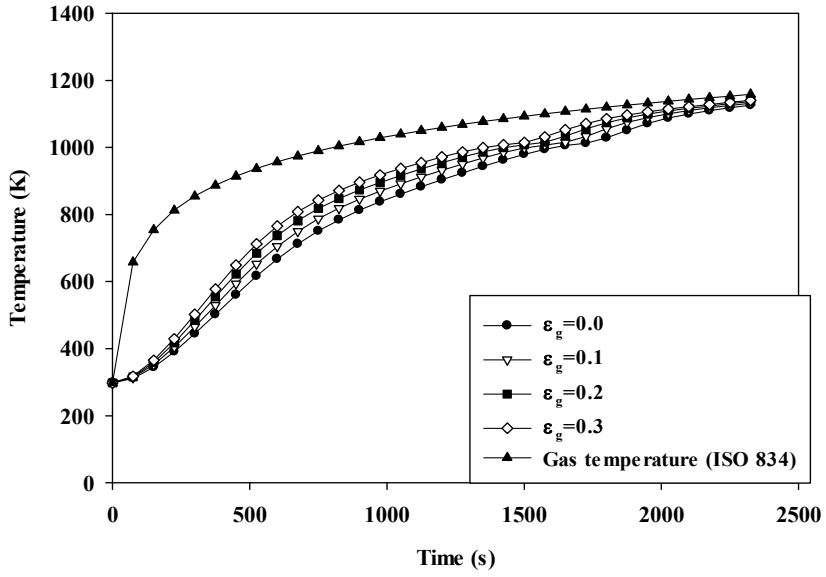

(a)

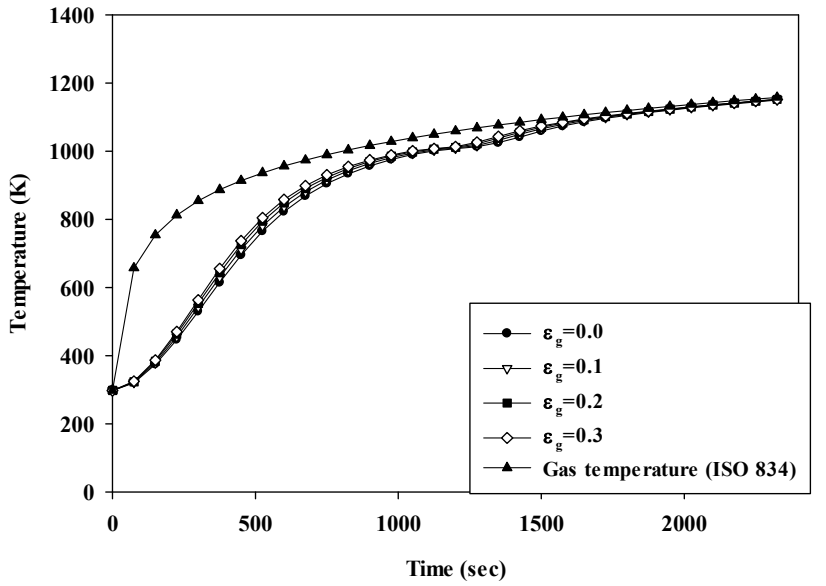

(b)

Figure 2-1: Temperature response of steel for different values of gas emissivity with steel height to concrete width ratios of a) 0.1 and b) 10.

2.2.2 Validation Cases

The furnace modeling approach was validated with heat flux measurements in a furnace without a test article as well as the temperature rise of structural element test specimens inside of a furnace. The model validation with the measured heat fluxes demonstrated the ability of the modeling approach to predict the transfer of heat from the furnace environment to the test specimen location. Test specimens within a furnace will typically have a temperature rise that lags the furnace, be constructed of different materials, and may have complex geometry that results in radiation exchange between the specimens itself as well as the furnace. As a result, two different structural element test specimens were selected to evaluate the ability of the model to predict the temperature rise of test specimens with materials having different thermal properties (i.e., steel, concrete) and complex geometry with radiation exchange between itself as well as the furnace.

2.2.2.1 Heat Fluxes from Furnace

Heat fluxes from a furnace environment have been measured in several studies to evaluate the effects of furnace size, furnace orientation, lining material inside the furnace, furnace exposure, and temperature measurement method for furnace control. For validation of the model, simulation results were compared with heat flux data taken in different size furnaces, furnaces in different orientations, furnaces with different lining materials, and tests with different furnace exposures.

Sultan [[8, 9]] made heat flux measurements in floor and wall furnaces using water-cooled Gardon heat flux gauges at five different locations distributed over the surface where the test specimen would be located. Results were reported for both intermediate and large-scale furnaces with propane gas fired burners [[8, 9]]. For comparison with the model, simulations were conducted on the 4.0 m wide, 5.0 m long, 3.0 m high floor furnace with insulated firebrick walls, the 3.6 m wide, 3.0 m high x 0.5 m deep wall furnace with ceramic blanket walls, and the 1.2 m wide, 1.8 m long, 0.5 m deep intermediate scale furnace with insulated firebrick walls tested in both vertical and horizontal orientation. All furnace exposures were in accordance with CAN/ULC-S101 (similar to ASTM E119 and ISO 834) with furnace control done using the average temperature measured using shielded thermocouples specified in CAN/ULC-S101.

Asaro et al. [[23]] reported heat flux measurements inside an intermediate scale furnace 1.22 m wide, 1.22 m long, 1.37 m high. The interior of the furnace was lined with ceramic insulation bricks with the test specimen surface covered with ceramic fiber blanket. The furnace was powered with natural gas powered burners and controlled using unshielded thermocouples as specified in ISO 834 and IMO A.754 [24]. Heat flux was measured at a single location on a furnace wall using a water-cooled Schmidt-Boelter heat flux gauge with the measurement surface mounted flush with the wall. Measurements were made with an ISO 834 fire exposure as well as a UL 1709 hydrocarbon pool fire exposure.

2.2.2.2 Temperature Rise of Concrete-Steel I-beam Floor Assembly

Wainmann and Kirby [16] conducted a series of experiments on an unprotected concrete slab floor with a single I-beam support on the fire exposure side of the concrete. In this study, measurements were made on the temperature rise of various size steel I-beams mounted below the concrete. This included temperature rise on the lower flange, web, and upper flange of the I-beam during the fire exposure. To evaluate the effect of beam size on the predictive capability of the modeling approach, the study included the four different size beams provided in Table 2-1. In all tests, the concrete slab was 125 mm thick and covered the top of the furnace. A total of 21 experiments were performed on these beams, which also provided data on the repeatability of the measurements. Based on statistical analysis of experimental data in Ref. [20], the repeatability in the temperature measurement was determined to be 5% for the web and lower flange while it was 10% for the upper flange.

The furnace was 3.0 m wide, 4.5 m high and 2.0 m deep and lined with high temperature refractory insulation. The gas temperature inside the furnace was measured using standard thermocouples as prescribed in ISO 834. Using natural gas powered burners, the furnace gas temperature was controlled to follow the ISO 834 time-temperature curve within the acceptable tolerance. Except for the initial 5-10 minutes, the gas temperature inside the furnace was equal to that measured using the furnace thermocouples [21]. With the exposure duration 25–40 minutes, the gas temperature in the furnace was taken to be equal to the ISO 834 time-temperature curve in the simulations. Figure 2-2 contains a rendering of the Abaqus model for the furnace with a slice view showing the steel I-beam mounted below the concrete slab.

Table 2-1: Steel beam cross-section details.

Section Serial Size (mm)	Mass per Meter (kg/m)	Width of Section (mm)	Depth of Section (mm)	Thickness		Beam Section Factor (1/m)
				Web	Flange	
356 X 171	67.0	172.0	363.0	9.22	15.30	142
254 X 146	42.7	147.3	259.6	7.30	12.70	169
406 X 178	59.8	173.0	403.0	8.28	12.83	173
305 X 165	46.0	165.7	307.1	6.70	11.80	184

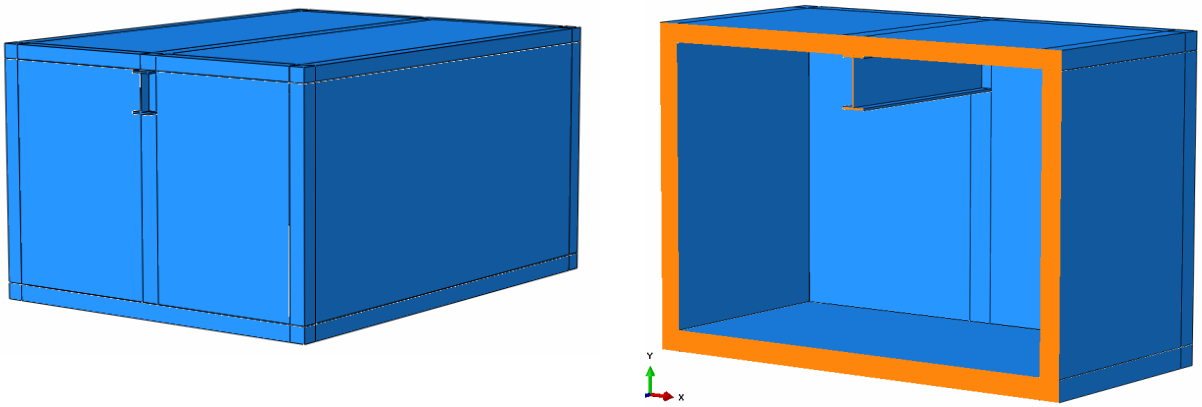

(a) Exterior view (b) Interior view

Figure 2-2: Abaqus model of the Wainmann and Kirby [16] steel-concrete floor furnace test.

2.2.2.3 Temperature Rise of Steel I-beam Assembly

Liu et al. [25] performed a series of furnace tests on a steel I-beam assembly shown in Figure 2-3. The details of the beams and columns are given in Table 2-2. The lower flange and the web of the 178x102x19 UB section beams were unprotected. The upper flange was protected

with 50 mm thick ceramic fiber blanket to simulate the heat sink effect of concrete. The columns of 152x152x30 UC section along with connections were protected with ceramic fiber blanket.

Table 2-2: Steel beam and column cross-section details.

Section Serial Size (mm)	**Mass per Meter (kg/m)**	**Width of Section (mm)**	**Depth of Section (mm)**	**Thickness**	
				Web	**Flange**
178 X 102	19.0	101.2	177.8	4.8	7.9
152 X 152	30.0	152.9	157.6	6.5	9.4

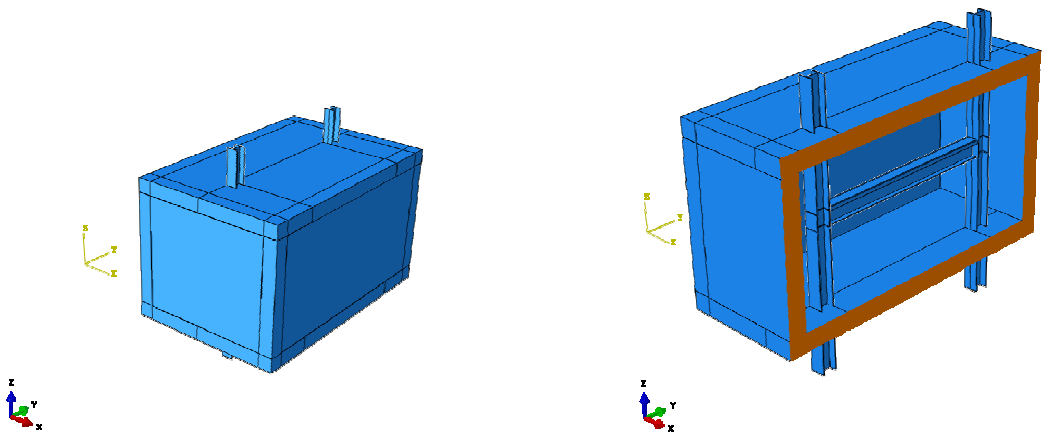

(a) Exterior view (b) Interior view

Figure 2-3: Abaqus model of the Liu et al. [25] I-beam assembly furnace test.

The furnace was 1.8 m wide, 3.0 m high and 3.0 m deep and lined with 200 mm thick ceramic fiber blanket. The burners were compartmented with ceramic fiber brick to provide a uniform heating exposure to the structural element and to prevent direct flame exposure. The furnace gas temperature was controlled to follow the ISO 834 time-temperature curve using unshielded thermocouples.

2.3 Simulation Details

Three-dimensional thermal analysis simulations were conducted using Abaqus 6.10-EF1. For this, a rectangular furnace enclosure was constructed similar to that shown in Figures 2-2 and 2-3. Five interior surfaces of the enclosure represented the furnace walls while the other surface was where the test specimen was placed. The five furnace walls were insulated surfaces with an assigned interior surface temperature that followed the desired time-temperature fire exposure curve. Three-dimensional thermal analysis was performed on the sixth surface to predict the temperature rise of the test specimen. The temperature rise of the test specimen was conducted using quadratic solid elements (DC3D20). In the model, thermal resistance between contact surfaces was not considered and the surfaces in thermal contact were forced to have the same temperature using TIE constraints. Analysis was performed using the nonlinear setting with a time step not exceeding 10 s.

The test specimen boundary conditions on the exposed side included convection with furnace gases, radiation exchange between surfaces on the inside of the furnace, and reradiation. The convection with the furnace gases was implemented using a convection heat transfer coefficient of 25 W/m^2-K as recommended in Eurocode 1 [1] and using a gas temperature equal to the time-temperature fire exposure curve. Radiation exchange between surfaces inside the furnace was performed using the Abaqus built-in radiation exchange model. For this, the furnace walls were divided into 150 mm size square elements while the test specimen was divided into element sizes appropriate to capture the temperature variation of the specimen and converged results. A furnace wall element size sensitivity study confirmed the selected wall element size produced in converged results. The view factor between an element inside the furnace and all other elements was calculated at the beginning of the simulation. Using these view factors and the instantaneous surface temperatures of elements inside the furnace, the radiation exchange inside the furnace was calculated at each time step. This approach assumes that the attenuation through the furnace gases is negligible, which was previously discussed to be appropriate for furnaces with clean burning furnace burners. Reradiation from the specimen surface was determined based on the interior element surface temperature.

The unexposed side of the test specimen included boundary conditions for convection and radiation exchange with the laboratory surroundings. The convection boundary condition

used a laboratory gas temperature of 298K and a convective heat transfer coefficient of 10 W/m^2-K [8]. The radiation exchange was determined using the element surface temperature on the unexposed side and a laboratory gas temperature of 298K.

The thermal analysis on the test specimen was conducted using temperature dependent thermal properties for steel, concrete, and ceramic fiber insulation. The properties used in the analysis given in Table 2-3 were taken from Eurocode 3 [23] for steel, Eurocode 2 [24] for concrete, and from the manufacturer for the ceramic fiber insulation [25]. The value of emissivity for concrete, steel, ceramic fiber, and furnace walls were 0.94, 0.9, 0.9 and 0.75; respectively [26].

2.4 Results

Simulation results are provided in the following sections and compared with experimental data from the literature. This was performed to benchmark the model with available data from furnace testing as well as demonstrate the modeling approach.

2.4.1 Predicted Heat Flux from Furnace

Predicted and measured heat fluxes from a furnace environment are provided in Figures 2-4 and 2-5. The comparison in Figure 2-4 is for large scale furnace experiments conducted by Sultan [9] in a floor furnace with insulation brick and a wall furnace with ceramic blanket. The model agrees well with the data up to about half way through the experiment, at which time the model over predicts the data. This deviation is attributed to measuring the heat flux with water-cooled Gardon gages. In environments with convection, Gardon gages are known to be produce heat fluxes less than the actual heat flux (Diller [27], Kuo [28]). Based on the analysis of Kuo [28] and the convection heat transfer value in furnace experiments, the Gardon is expected to be 20% low.

Table 2-3: Thermal and physical properties of test specimen materials.

	Concrete			Steel		Ceramic Fiber	
Temperature (K)	k (W/mK)	c_p (J/kgK)	ρ (Kg/m^3)	k (W/mK)	cp (J/kg-K)	k (W/mK)	cp (J/kg-K)
293	1.95	900	2400	53.34	441.15	3.7e-2	
373	1.76	900	2400	50.67	521.42	3.83e-2	819.18
453	1.59	980	2363	48.0	631.84	5.23e-2	850.93
533	1.43	930	2330	45.34	779.24	6.88e-2	881.40
613	1.29	970	2301	42.68	970.44	8.80e-2	910.59
693	1.16	1100	2276	40.01	1212.25	1.09e-1	938.51
773	1.04	1100	2259	37.35	1511.5	1.34e-1	965.14
853	0.94	1100	2242	34.69	1875.0	1.61e-1	990.49
933	0.85	1100	2225	32.02	832.69	1.90e-1	1014.60
1013	0.77	1100	2209	29.36	2525	2.22e-1	1037.4
1093	0.71	1100	2192	27.3	745.22	2.57e-1	1058.9
1173	0.66	1100	2175	27.3	435	2.94e-1	1079.1
1253	0.63	1100	2158	27.3	650	3.33e-1	1098.1
1333	0.61	1100	2141	27.3	650	3.75e-1	1115.7
1413	0.60	1100	2125	27.3	650	4.20e-1	1132.1
1493	0.60	1100	2108	27.3	650	4.67e-1	1147.2

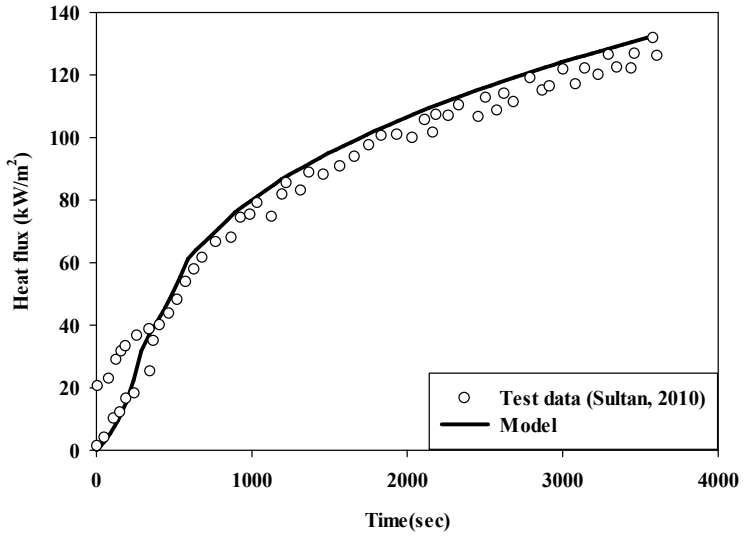

(a)

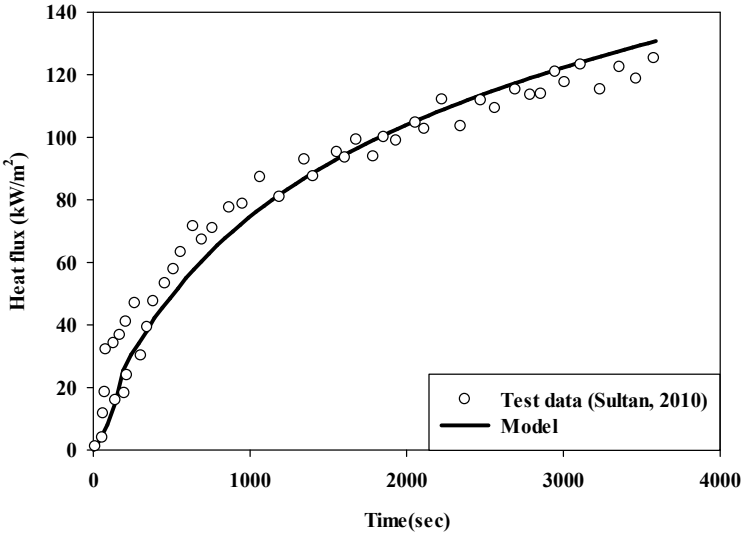

(b)

Figure 2-4: Heat flux predictions of a CAN/ULC-S101 (similar to ASTM E119 and ISO 834) furnace exposure compared with data measured by Sultan [9] in a furnace lined with a) fire insulation brick and b) ceramic fiber blanket.

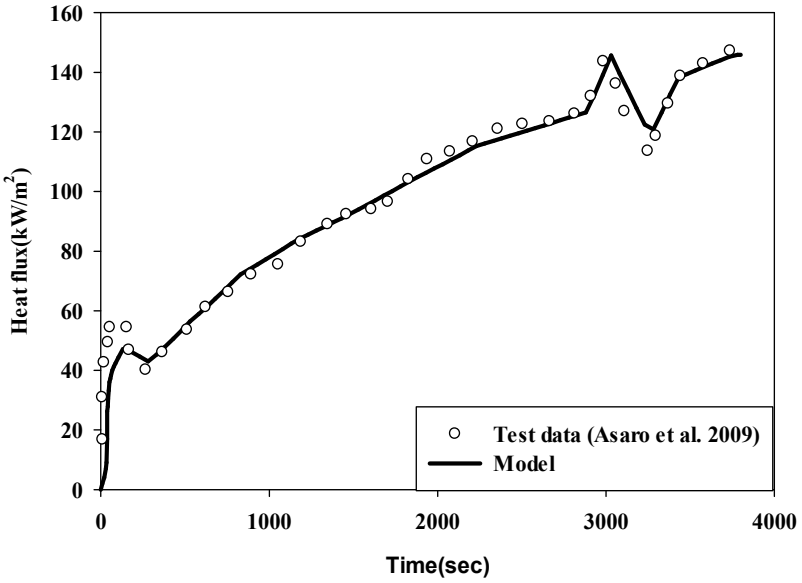

(a)

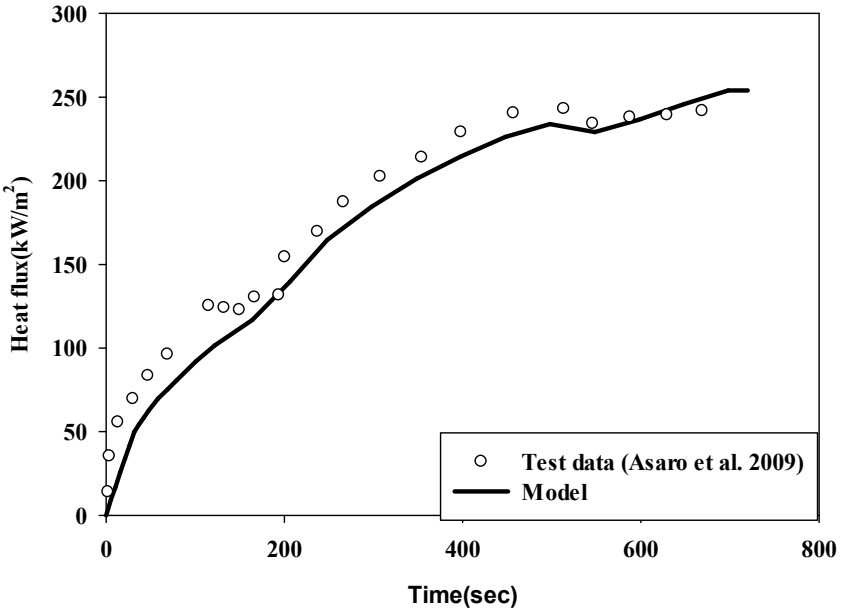

(b)

Figure 2-5: Heat flux predictions from a) an IMO A.754(18) and b) a UL 1709 furnace exposure compared with data measured by Asaro et al. [23]

Figure 2-5 contains a comparison experiments performed in an intermediate scale furnace two different furnace exposures : i) IMO A. 754 [24] which is similar to ISO 834 and ii) UL 1709 hydrocarbon pool fire exposure. The predicted heat fluxes agree well with the data. This is in part due to the heat flux measurements being made in this case using Schmidt-Boelter heat flux gages which are not as prone to error in exposure environments with convection.

2.4.2 Temperature Rise of Concrete-Steel I-Beam Floor Assembly

A series of simulations were performed to predict the temperature rise of unprotected concrete-steel I-beam floor assemblies tested by Wainman and Kirby [12]. Simulations were conducted on different size I-beams described in Table 2-3 with all assemblies exposed to an ISO 834 time-temperature furnace fire exposure.

Thermal response predictions for the 254 x 146 beam are provided in Figure 2-8. As seen in Figure 2-8a, the temperature response was within 10% for all parts of the beam for the duration of the exposure. The temperature distribution inside the furnace is shown in Figure 2-8b for the 254x146 beam after an exposure duration of 1200s. The distribution plot shows the difference in temperatures between the concrete slab on top of the furnace, the steel I-beam beneath the concrete, and the furnace walls. In addition, note the temperature variation along the height of the I-beam and through the thickness of the concrete slab. In the structural response of these members, these variations in temperature along the height of the beam and through the concrete thickness will produce thermally induced moments that will cause bending in the test specimen. Therefore, it is important to accurately predict these temperature gradients to ensure the correct structural response.

Figure 2-9 contains the thermal response predictions compared with data for the other three size I-beams mounted below the concrete. From results in Figures 2-8 and 2-9, the model predicts the temperature response of the web and lower flange within 5% and within 10% of the upper flange temperature data. Based on statistical analysis of experimental data in Ref [12], the repeatability in the temperature measurement was determined to be 5% for the web and lower flange while it was 10% for the upper flange. As a result, the deviation in the model and the data was attributed to the uncertainty in the experimental data.

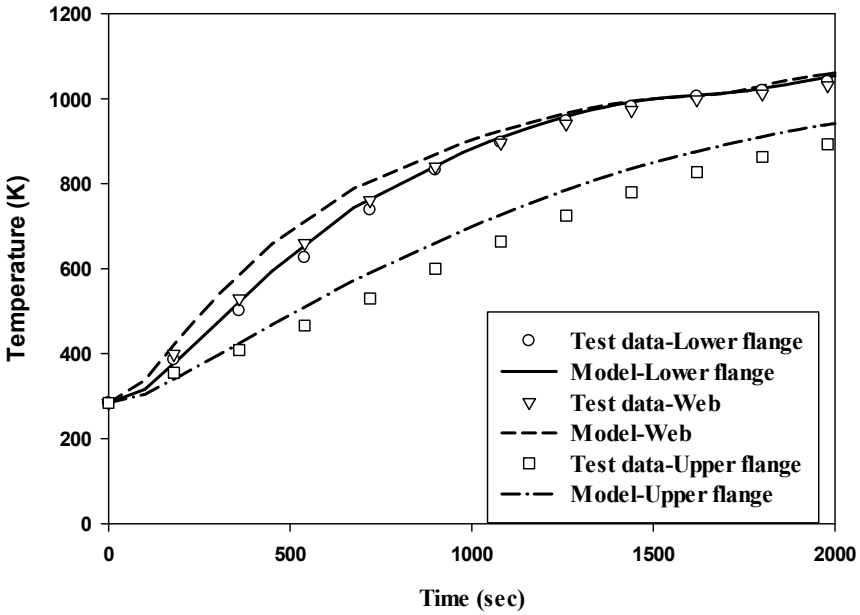

(a)

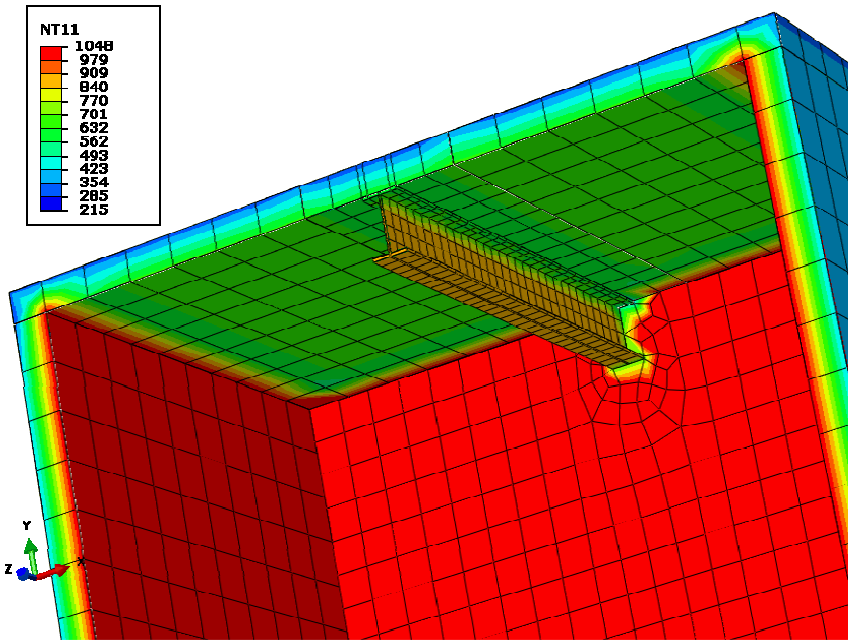

(b)

Figure 2-6: Temperature response of 254x146 steel I-beam mounted below the concrete slab a) as a function of time and b) spatial distribution after exposure duration of 1200s.

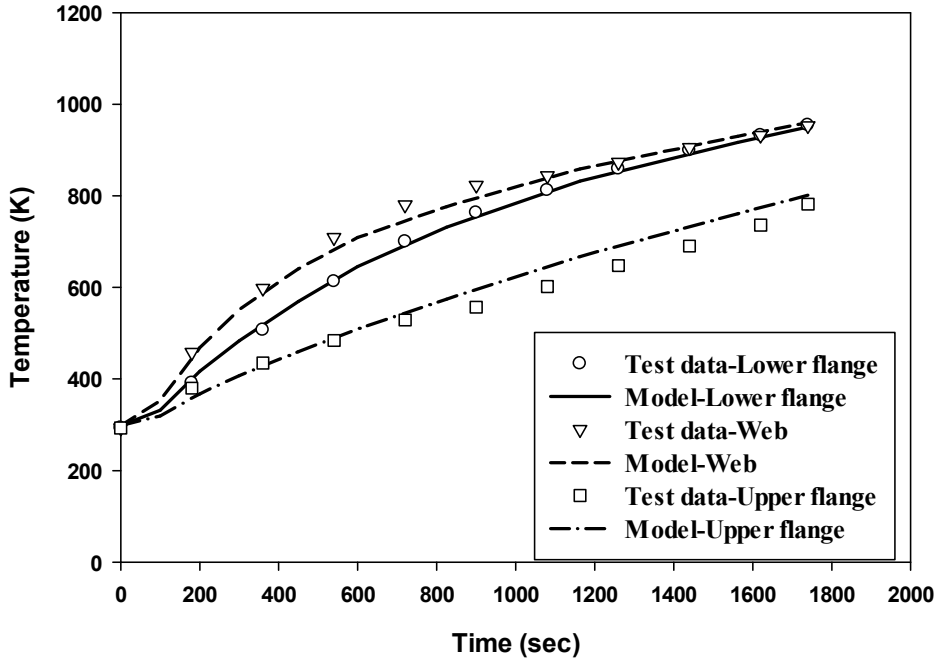
Temperature (K)
Time (sec)
0
200
400
600
800
1000
1200
1400
1600
1800
2000
Test data-Lower flange
Model-Lower flange
Test data-Web
Model-Web
Test data-Upper flange
Model-Upper flange

(a)

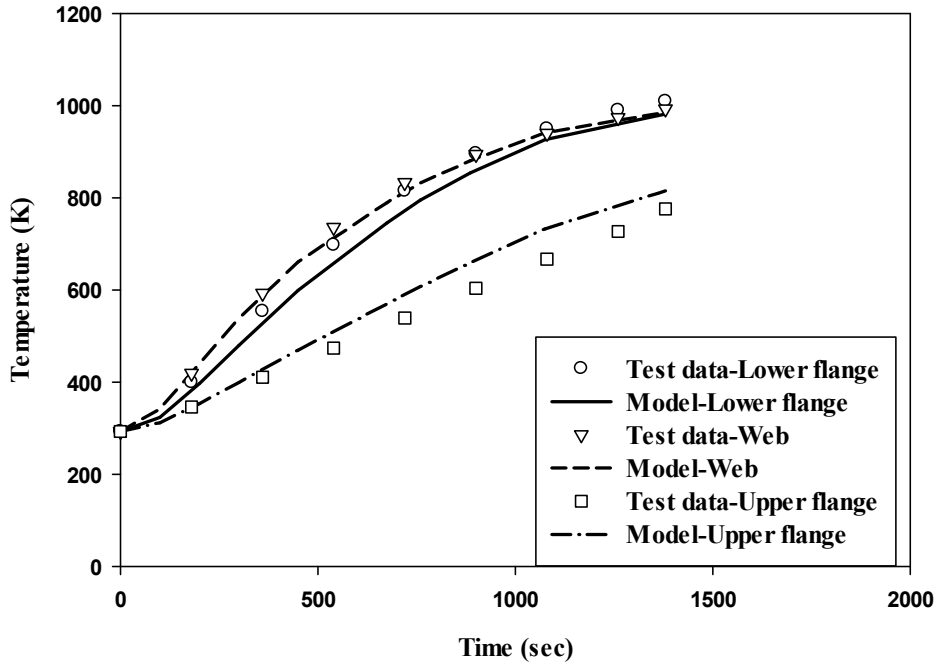
Temperature (K)
Time (sec)
0
200
400
600
800
1000
1200
500
1500
2000
Test data-Lower flange
Model-Lower flange
Test data-Web
Model-Web
Test data-Upper flange
Model-Upper flange

(b)

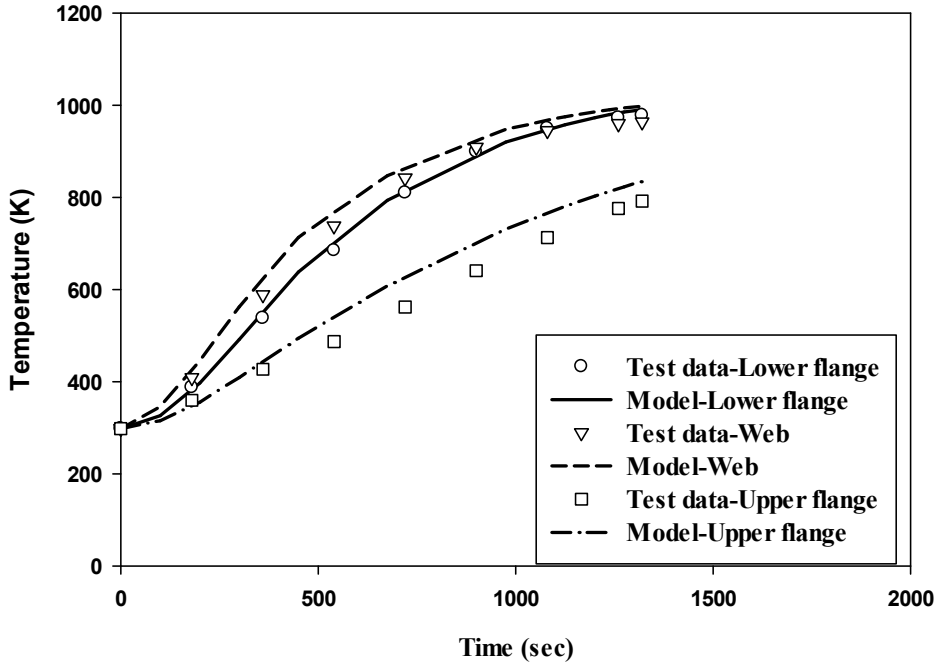

(c)

Figure 2-7: Prediction of thermal response of beams with dimensions of a) 356 x 171, b) 406 x 178, and c) 305 x 165 in comparison with other experimental data.

2.4.3 Temperature Rise of Steel Beam Assembly

Liu et al. [25] measured temperatures on the lower flange, the web, and the upper flange of a steel I-beam axially restrained by two steel columns on both sides during a furnace exposure. In total, 20 tests were performed with two different types of connections and three different levels of load. A 178 X 102 X 19UB (S275) steel I-beam section was used in the tests. Thermal response predictions for the restrained steel I-beam are provided in Figure 2-10. As seen in Figure 2-10b, the temperature response was within 10% of the data for all parts of the beam for the exposure duration. The spatial temperature distribution inside the furnace is provided in Figure 2-10a for the restrained steel I-beam after an exposure duration of 1175s. The Figure shows the difference in temperatures between the two columns on both sides of the beam, the restrained steel I-beam, and the furnace walls. The top of the columns are cooler since they extend outside the furnace and are not directly exposed to the furnace environment.

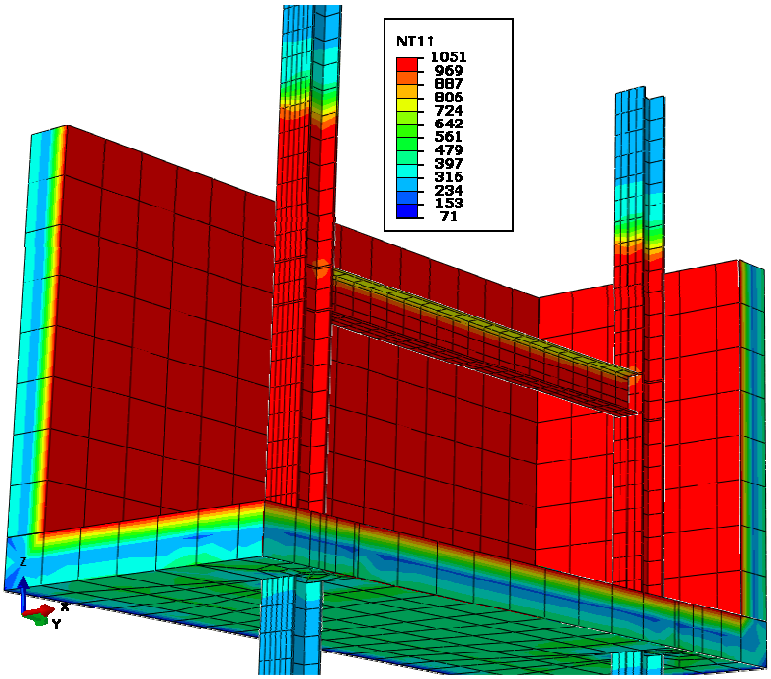

(a)

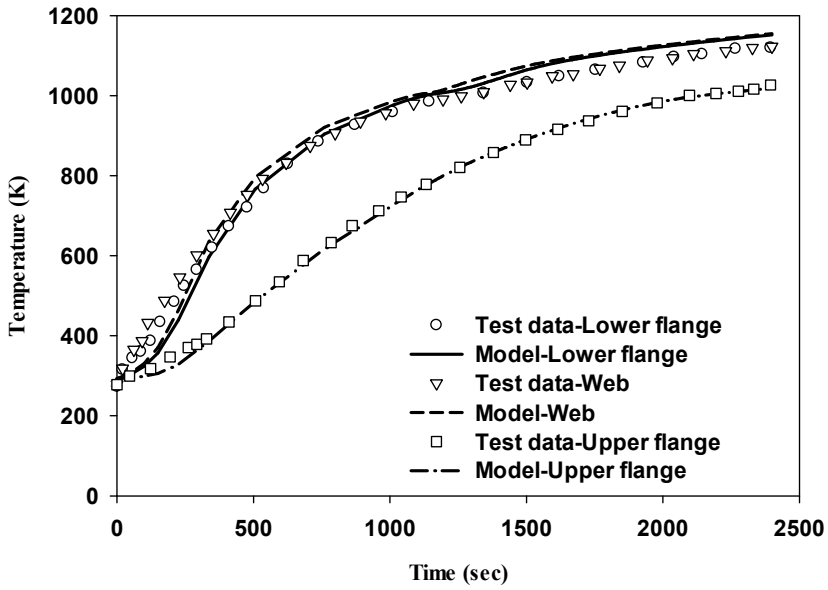

(b)

Figure 2-8: Temperature response of a 178x102x19UB steel I-beam axially restrained by two steel columns : a) spatial distribution after exposure duration of 1175s and b) as a function of time.

2.5 Sensitivity

A sensitivity analysis was performed to investigate the role of the convective heat transfer coefficient and emissivity of the interior surfaces. The sensitivity was evaluated through comparing the temperature rise of the steel I-beam from the Waimann and Kirby furnace tests due to modifying an input parameter. Table 2-4 contains the specific variables evaluated, their variation range, and the change in the temperature rise on different parts of the beam. The results indicate that the steel temperature rise results in less than 10% temperature variation due to the uncertainty of the model input parameters. The model was most sensitive to the heat transfer coefficient inside the furnace, indicating that good measurements of this parameter are desirable to ensure accurate predictions.

Table 2-4: Sensitivity of input parameters on temperature rise of structural element.

Model parameter	Variation range	Change in element temperature (K)		
		Lower flange	Web	Upper flange
Steel emissivity	0.7-0.9	10	10	10
Concrete emissivity	0.7-0.9	10	10	10
Furnace wall material emissivity	0.6-0.9	30	30	30
Convective heat transfer co-efficient ($Wm^{-2}K^{-1}$)	15-35	50	50	50

After doing the sensitivity study on the role of convective heat transfer co-efficient and emissivity of the interior surfaces, the role of furnace lining materials on the heat exposure onto specimen was performed. At first the time temperature response of a rectangular slab (3.6m x 4.9m x 0.15m) made of firebrick and ceramic fibre was predicted through 1D heat transfer analysis. The thermal properties of firebrick and ceramic fibre was given in Table 2-5 [8]. After that the predicted temperature was assigned as the surface temperature of the furnace wall

material and gauge heat flux onto specimen was computed. It was observed that the firebrick temperature rise lags the ceramic fibre temperature rise by as much as 400K. The lower temperature rise of firebrick also results in lower heat flux on the specimen as shown in Figure 2-11b. The analysis indicates that the model was sensitive to the properties of furnace lining materials. Care should be taken in using the model to predict the element time temperature response in furnace geometries made from high conductivity materials.

Table 2-5: Thermal and physical properties of furnace lining materials.

Furnace lining material	**Firebrick**	**Ceramic fibre**
Thermal conductivity ($Wm^{-1}K^{-1}$)	1.15	0.04
Specific heat ($Jkg^{-1}K^{-1}$)	900	1150
Density (kgm^{-3})	2600	160

Care should be taken in using the model to predict the element time temperature response in furnace geometries made from high conductivity materials.

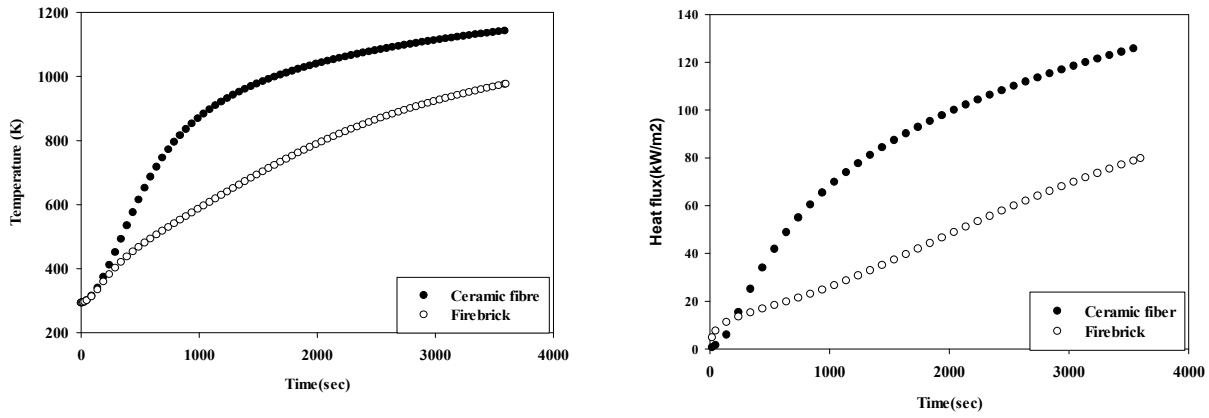

(a) Temperature response (b) Heat flux prediction

Figure 2-9: Furnace wall lining material response from an ASTM E119 exposure as a function of time

2.6 Discussion

The importance of including the radiation exchange in the modeling was further evaluated by comparing the current modeling with other models reported in the literature as well as providing additional results on the heat fluxes to the structural elements during the exposure.

Figure 2-12 provides a comparison of results from the Abaqus model reported in this study including radiation exchange along with other proposed furnace exposure models in the literature [1, 12, 16, 29] Results in Figure 2-12 are for the lower flange on the 254 x 146 steel I-beam. From the results in Figure 2-12, the current model predicts the temperature response of the unprotected structural steel member better than the other models. The models proposed [1, 12] are easier to implement; however, they are less accurate since they only provide a single temperature for the entire beam cross-section. From Figures 2-8 to 2-10, this may result in more significant error at other locations in the beam (e.g. the web) than shown in Figure 2-12. In addition, the use of a uniform temperature over the height of the beam may result in nonrealistic structural response. These non-uniform temperature profiles will induce bending and additional stresses in the structural element, which will not be observed if uniform temperatures are present.

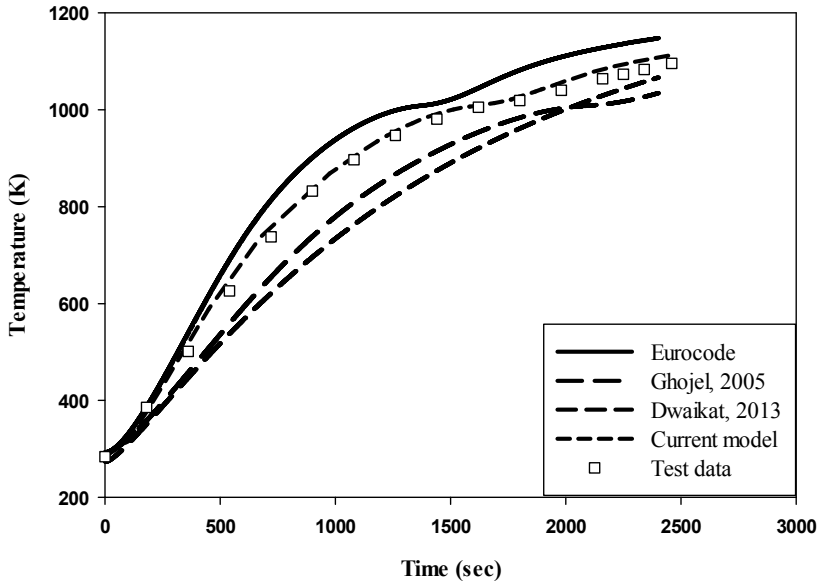

Figure 2-10: Prediction of the lower flange temperature response on a 254 x 146 beam using different models.

The model used in this study includes both the convection from the furnace environment as well as the radiation exchange between surfaces. As a result, the magnitude of the net convection and radiation heat flux in the temperature rise of a steel I-beam was predicted. A comparison of net convective and radiative heat flux to the lower flange of the 254x146 steel I-beam is shown in Figure 2-13. It is seen that both net radiative and net convective heat flux increase for the initial 200s reaching 25 kW/m^2 and 10 kW/m^2, respectively. These are the maximum net heat fluxes during the exposure due to the thermal lag between the furnace environment and steel. Following this, the net radiation and net convection heat fluxes to the steel decrease by approximately 5-8 kW/m^2 over the remainder of the simulation. During the exposure, the radiation represented 70-80% of the net heat flux to the surface. These findings clearly demonstrate that the radiative heat transfer is the dominant mode of heat transfer in the standardized furnace fire environment.

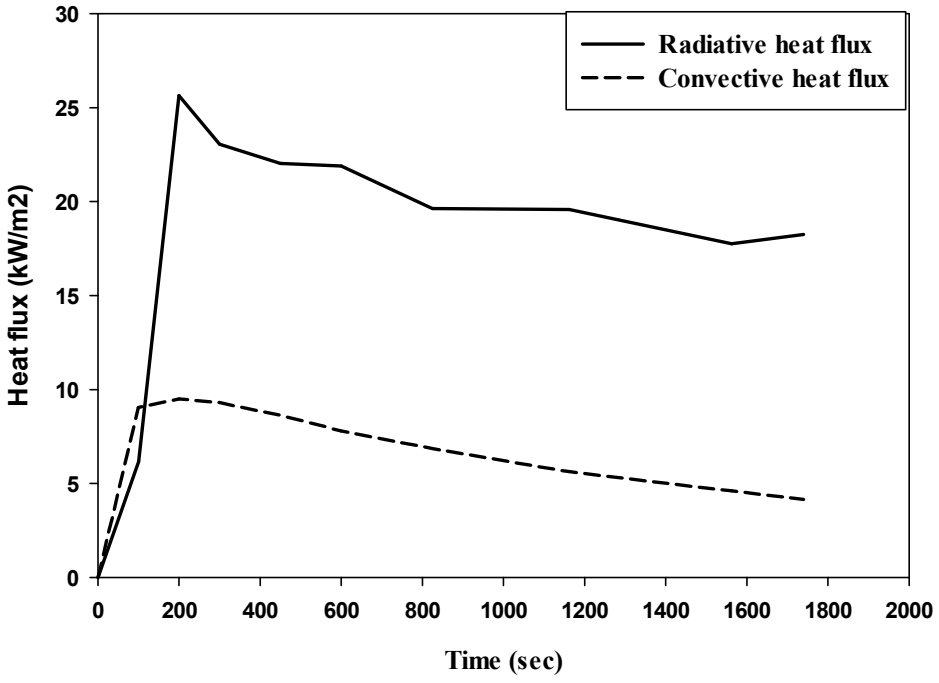

Figure 2-11: Comparison between convective and radiative heat flux to the lower flange of the 254 x 146 beam

2.7 Conclusions

A methodology was developed to predict the thermal exposure from a furnace environment. In furnaces with low conductivity wall linings and containing burners with complete combustion, gas attenuation effects were small making the radiation exchange between surfaces and convection the dominant modes of heat transfer to the specimen. This was modeled by assigning the internal furnace wall temperature to the furnace time-temperature exposure and performing a three-dimensional heat transfer analysis on the specimen.

The heat transfer to the specimen predicted by the model was compared with heat fluxes measured in furnaces of different sizes and with different wall linings. The furnace exposure model predicted heat transfer to the specimen surface that was within 10% of measured heat fluxes.

The proposed furnace exposure methodology was used to predict the temperature rise of steel in a floor assembly. Predictions were within 10% of the measured values, which was within the experimental uncertainty. The proposed method produced better predictions compared with other furnace exposure models given in the literature. The most significant difference of this model was the inclusion of radiation exchange between surfaces while neglecting gas radiation attenuation.

2.8 References

1. CEN, Eurocode 1, Actions on Structures: General actions; actions on structures exposed to fire2002, Brussels, Belgium: European Committee for Standardization.
2. Laboratories, U., UL1709-Rapid rise Fire Tests of Protection Materials for Structural Steel, 1990: Northbrook, IL.
3. ISO-834, Fire resistance tests-elements of building construction - Part 1.1: General Requirements for Fire Resistance Testing, 1975, International Standard Organization: Geneva, Switzerland.
4. ASTM E119: Standard Test Methods for Fire Tests of Building Construction and Materials, 1995, American Society for Testing and Materials: Philadelphia, PA.
5. Institution, B.S., Eurocode 3: Design of Steel Structures: Part 1.2 General Rules - Structural Fire Design (together with United Kingdom National Application Document)2001: BSI.
6. Sultan, M., T. Harmathy, and J.R. Mehaffey, Heat transmission in fire test furnaces. Fire and materials, 1986. **10**(2): p. 47-55.

7. Sultan, M.A., The effect of furnace parameters on fire severity in standard fire resistance tests. Fire and materials, 1996. **20**(5): p. 245-252.
8. Sultan, M.A., Fire resistance furnace temperature measurements: Plate thermometers vs shielded thermocouples. Fire technology, 2006. **42**(3): p. 253-267.
9. Sultan, M.A., Performance of Different Temperature Sensors in Standard Fire Resistance Test Furnaces. Fire technology, 2010. **46**(4): p. 853-881.
10. Cooke, G. Can Harmonization of Fire Resistance Furnaces be Achieved by Plate Thermometer Control? in Fire Safety Science—Proceedings of the Fourth International Symposium. 1994.
11. Wickstrom, U. Calculation of heat transfer to structures exposed to fire- shadow effects. in InterFlam 2001: 9 th International Fire Science & Engineering Conference. 2001.
12. Ghojel, J.I. and M.B. Wong, Heat transfer model for unprotected steel members in a standard compartment fire with participating medium. Journal of Constructional Steel Research, 2005. **61**(6): p. 825-833.
13. Ghojel, J.I., A new approach to modeling heat transfer in compartment fires. Fire Safety Journal, 1998. **31**(3): p. 227-237.
14. Cedeno, G.A., A.H. Varma, and J. Gore. Predicting the Standard Fire Behavior of Composite Steel Beams. 2008. Tabernash, Colorado: ASCE.
15. Nahid, M.N. and B.Y. Lattimer. Modeling Heat Transfer During Furnace Fire Exposures. in ASME 2012 International Mechanical Engineering Congress and Exposition. 2012. American Society of Mechanical Engineers.
16. Wainman, D.E., B.R. Kirby, and L. British Steel Technical. Swinden, Compendium of U.K. standard fire test data : unprotected structural steel, 11987, Rotheram [England]: British Steel Technical, Swinden Laboratories.
17. Gardner, L. and K. Ng, Temperature development in structural stainless steel sections exposed to fire. Fire Safety Journal, 2006. **41**(3): p. 185-203.
18. Kay, T.R., B.R. Kirby, and R.R. Preston, Calculation of the heating rate of an unprotected steel member in a standard fire resistance test. Fire Safety Journal, 1996. **26**(4): p. 327-350.
19. Wong, M.B., Size effect on temperatures of structural steel in fire. Journal of Structural Engineering-Asce, 2005. **131**(1): p. 16-20.
20. Wong, M.B. and J.I. Ghojel, Spreadsheet method for temperature calculation of unprotected steelwork subject to fire. The Structural Design of Tall and Special Buildings, 2003. **12**(2): p. 83-92.
21. Lattimer, B.Y., et al., Structural Response of fiber Reinforced Plastic Composites During Fires, in The 11th Interflam Conference2007: London, UK. p. 653-664.
22. Hibbitt, Karlsson, and Sorensen, Abaqus/Standard Version 6.10 EF-1, Hibbitt, Karlsson and Sorensen Inc.: Pawtucket, RI.
23. Asaro, R.J., B. Lattimer, and W. Ramroth, Structural response of FRP composites during fire. Composite Structures, 2009. **87**(4): p. 382-393.

24. A.754(18), I.R., Recommendation on Fire Resistance Tests for “A”, “B” and “F” Class Division, in FTP Code – International Code for Application of Fire Test Procedures1998, International Maritime Organization: London.
25. Liu, T., M. Fahad, and J. Davies, Experimental investigation of behaviour of axially restrained steel beams in fire. Journal of Constructional Steel Research, 2002. **58**(9): p. 1211-1230.
26. Siegel, R. and J.R. Howell, Thermal Radiation Heat Transfer2002: Taylor & Francis.
27. Diller, T., Advances in heat flux measurements. Advances in heat transfer, 1993. **23**: p. 279-368.
28. Kuo, C. and A. Kulkarni, Analysis of heat flux measurement by circular foil gages in a mixed convection/radiation environment. Journal of heat transfer, 1991. **113**(4): p. 1037-1040.
29. Dwaikat, M. and V. Kodur, A simplified approach for predicting temperatures in fire exposed steel members. Fire Safety Journal, 2013. **55**: p. 87-96.

3 A Radiative Fraction Approach for Predicting Conditions from Small and Large Scale Fires

3.1 Introduction

The prediction of heat exposure from a fire is important in a number of applications such as the durability of offshore and onshore terminals, possibility of ignition of materials, fire spread, and heating of structural members. Predicting the heat exposure onto an object from a fire depends on the burning rate of the fuel, thermal radiation from the fire, gas temperature, and velocity. The cost and lack of facilities required to conduct real scale experiments, especially large fires, highlights the need for validated numerical models to predict fire conditions and heat exposures onto adjacent objects. The model needs to provide accurate prediction of the fire environment at a range of scales (fire diameters of 0.1 – 10 m) to support simulating fires in a range of applications.

Previous studies on predicting fire conditions (e.g., gas temperature, velocity) and heat exposure onto objects were limited to the validation of a specific fire scenario [1-3]. Xin et al. [2] conducted a validation study on a large scale methane pool fire using a fixed radiative heat loss method in Fire Dynamic Simulator (FDS) for a fire size up to 2.5 MW fire with a diameter up to 1.0 m. It was found that the way radiation is treated affected the maximum gas temperature calculated, but no guidance was provided on selecting the appropriate value for radiative fraction particularly for larger fires.

Several research studies have been conducted to quantify the fire conditions for various types of fuels, diameters, and fire heat release rates [4-9]. Through this work, the maximum gas temperature for a fire was measured to increase with fire diameter. Fires up to 2.0 m were measured to have maximum gas temperatures of 800 - 900°C while increasing the diameter to 6.0 m and 15.0 m caused gas temperatures to increase to 1000°C and 1100°C, respectively [10]. In larger diameter fires with $D > 1.0$ m, the maximum flame temperature is governed by the radiative heat loss to the surroundings [11]. The radiative heat loss is directly related to the levels of major combustion products (CO_2 and H_2O) and soot particles. For large diameter fires, the amount of entrained air is not sufficient for complete combustion to occur resulting in a large amount of soot production particularly around the outer perimeter of the fire. However, experimental data for large diameter fires indicates that the emissive power of fires reduces with

an increase in diameter [10, 12]. The presence of thick black smoke on the outer periphery of the fire blocks the radiation emitted onto the surroundings. Figure 3-1 contains pictures of the flame dynamics for a small scale propane fire (D=0.34 m) and a large scale JP-8 aviation fuel (D=7.92 m) fire. Note that the fire diameter of 0.34 m resulted in a luminous flame whereas a fire diameter of 7.92 m resulted in a sooty fire. In addition, the soot particles accumulate on the outer periphery of the fire and formed a thick layer of black smoke. These results signify the need for a computationally efficient method to account for the increase in soot production due to the scale of the fire in order to accurately predict gas temperature and heat transfer to surfaces.

(a) (b)

Figure 3-1: Fully developed fire plume of a) a small scale propane fire and b) a large scale JP-8 aviation fuel fire [13].

Several models have been proposed to predict soot formation and oxidation in flames and fires [14-20]; however, the predictive abilities of the models are limited to laminar and smaller scale turbulent fires. Joulain and Most [21] developed a model to predict soot formation and oxidation using a two-equation model. The radiative heat transfer was predicted using the model developed by Modak [19], which is only applicable for an isothermal and homogeneous gas mixture. Markstein and de Ris [22] established that soot formation, oxidation and radiation correlates with laminar smoke point height of the fuel. Using the laminar smoke point concept, Lautenberger [16] developed a soot model suitable for fire applications and validated it with laminar diffusion flame test results. Beji and Delichatsios [17] developed a soot model based on gaseous phase combustion and species concentrations for a laminar diffusion flame. Chatterjee et

al. [18, 23] developed a sub grid scale soot radiation model and linked it with large eddy simulation (LES) through a local strain rate. The assumption of an optical thin medium in the energy equation limits its validity for large diameter fires. Yao et al. [24, 25] developed a global soot model based on conditional moment closure to calculate the soot volume fraction, but the method is computationally expensive. Chen et al. [20] extended the eddy dissipation concept in the LES framework and coupled it with the laminar based smoke point soot model. Validation of the model by Chen et al. [20] was limited to fire sizes of 125 kW and fire diameters of 0.3 m. These models show great promise, but their use in predicting large fires (> 2.0 m in diameter) has not been demonstrated.

A method is provided in this paper for predicting the fire conditions and heat flux exposure from a fire onto an object for fire diameters ranging from 0.3 m to 15.0 m using FDS. The FDS model accounts for soot formation changes using a radiative fraction concept. The predicted gas temperature and velocity is compared with available data on unobstructed and obstructed fires to demonstrate the ability of the model to account for the change in fire diameter, fuel type, and geometry. The methodology is then used to predict the heat transfer to an object in different geometries and compared with data.

3.2 Fire Exposure Modeling

FDS, Version 6.0 [26] developed by NIST was used to predict the fire conditions as well as the heat exposure onto objects in contact with flames or plumes. An empirically based radiative fraction modeling approach was developed to allow accurate prediction of the fire conditions over a range of scales. The model does not include the formation or oxidation of soot particles and the scattering of radiation due to soot particles inside the flame directly, but instead accounts for the effects of soot production through the radiation emitted from the fire to the surroundings.

FDS is a computational fluid dynamics (CFD) model that uses Large Eddy Simulation (LES) to predict buoyancy driven flows, thermal conditions, and species concentrations that develop due to a fire. FDS predicts gas phase conditions as well as the condensed phase response such as temperature rise of solid boundaries. Radiative heat transfer is solved using the radiation transport equation for a gray gas.

Typical simulations of a fire require a grid cell size on the order of tens of centimeters whereas to fully resolve the flame sheet a grid cell size on the order of millimeters is needed. As a result, the computed temperatures are lower than the maximum temperature of a diffusion flame since they correspond to the bulk average of a grid cell. In order to account for the use of relatively large grid cell size in the radiation calculations, the emission source term within the flaming region is defined as

$$\kappa I_b = \begin{cases} \frac{\kappa\sigma T^4}{\pi} & outside\ flame\ zone, \dot{q}''' = 0 \\ \frac{C\kappa\sigma T^4}{\pi} & Inside\ flame\ zone, \dot{q}''' > 0 \end{cases} \quad (1)$$

where I_b is the radiative source term (W.sr^{-1}.m^{-1}), κ is the absorption coefficient (m^{-1}), σ is the Stefan-Boltzmann constant (5.67x10^{-8} W/m^2-K^4), T is the cell gas temperature (K). The correction factor is given by

$$C = \frac{\sum_{\dot{q}'''_{ijk}>0}\left(\chi_r \dot{q}'''_{ijk} + \kappa_{ijk} U_{ijk}\right) dV}{\sum_{\dot{q}'''_{ijk}>0}\left(4\kappa_{ijk}\sigma T^4_{ijk}\right) dV} \quad (2)$$

where $\dot{q}'''_{ijk}$ is the heat release rate per unit volume for the cell designated by *ijk* (kW/m^3), χ_r is the radiative fraction, and U is the integrated radiant intensity, and V is the cell volume (m^3). The constant C is computed at each time step so that the net radiant energy emitted by the entire flaming region will be equal to the empirically estimated fraction of energy emitted as thermal radiation over the same region.

A radiative fraction model was used to account for the effects of soot production changes on radiation loss from the fire as a function of fire diameter. Radiative fraction is the portion of the fire heat release rate that is lost to the surroundings due to radiation transport. The remaining portion of the heat release rate was convected upward into the atmosphere. The radiative fraction is the fraction of the combustion heat release rate that is emitted as thermal radiation [12] and is defined by

$$\chi_r = \frac{Q_{rad}}{Q_{tot}} \quad (3)$$

where Q_{rad} is the total radiative power output (kW) and Q_{tot} is the total heat release rate of the fire (kW) assuming complete combustion. Assuming isotropic distribution of radiation, the total radiative power can be calculated by

$$Q_{rad} = 4\,\pi\,R_0^2\,q_0 \tag{4}$$

where R_0 is the distance between center of the pool (m) and q_0 is the radiative flux measured by a radiometer (kW/m^2).

The radiative fraction model used in this work was based on the measured change in radiative fraction with fire diameter for different fuel types [12, 27]. As seen in Figure 3-2, the radiative fraction for fire diameters less than 1.0 m is constant at an average value of 0.42 ± 0.10 for hydrocarbon fuels. Data for alcohol is shown in Figure 3-2 to be 2 to 4 times lower than the radiative fraction for hydrocarbon fuels at fire diameters less than 1.0 m. For hydrocarbon fuels, the radiative fraction is shown in Figure 3-2 to decrease with an increase in fire diameter from 1.0 m to 10.0 m. For larger fire diameters (D>10.0 m), the value of radiative fraction approaches a constant average value of 0.06 ±0.2. Note that LNG fires have higher radiative fraction at large diameters, which may be expected since methane burns more completely compared with higher order hydrocarbons. A proposed relation between fire diameter and radiative fraction for hydrocarbon fuels is

$$\chi_r = 0.06 + \frac{0.42}{1 + exp^{\frac{D-3}{1.5}}} \tag{5}$$

where D is the fire diameter (m). This relation is shown plotted in Figure 3-2. The values obtained with the expressions proposed by Munoz et al. [27] and McGrattan et al. [28] are lower compared with that predicted using Eqn. (5) for lower fire diameters. Moreover, the expression proposed by McGrattan et al. [28] over predicts the radiative fraction for fire diameters of greater than 5.0 m. The radiative fraction from Figure 3-2 and Eqn. (5) was included in FDS as a user input based on the fire diameter being simulated. Since the value of radiative fraction takes into account the effect of soot production on the fire exposure, the production rate of soot and *CO* were set to 0.0 in FDS. As a result, this method is not appropriate for fire exposures where the visibility through smoke is important.

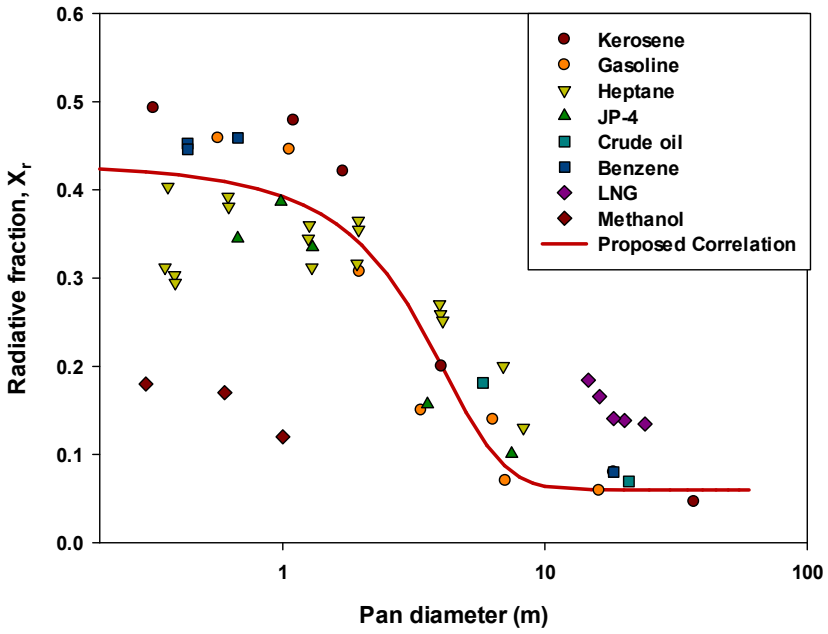

Figure 3-2: Radiative fraction, χ_r as a function of fire diameter [12, 28].

The use of FDS and the radiation fraction model to account for the changes in soot production with change in scale was evaluated in this paper through comparison of the simulation results with data from several validation test cases. These cases are described in the next section along with the simulation details. A comparison of the model results with the data is then provided.

3.3 Validation Cases

The modeling approach was validated with gas temperature and velocity measurements for unobstructed and obstructed fires as well as the heat flux measurements onto objects obstructing the fire. These validation data were taken from different experimental studies in order to demonstrate the predictive capability in a variety of scenarios.

3.3.1 Unobstructed Fire

3.3.1.1 Gas Temperature and Velocity

Gas velocities and temperatures in the fire plume (i.e., flaming region) have been measured in several studies [4, 5, 8, 29, 30] for unobstructed fires to evaluate the effects of fire

heat release rate, fire diameter, and fuel type. The model was validated with two different data sets to provide a comparison of model results over a range of fire diameters.

Koseki and Taro [31] made centerline gas temperature and velocity measurements in unobstructed pool fires using 0.32 mm diameter, Type K sheathed thermocouple and bi-directional stainless steel pressure probe, respectively, at different elevations above the fuel surface. Results were reported for a range of fire diameters and heat release rates with heptane burning on top of water in a pan. For comparison with the model, simulations were conducted on fire diameters of D = 0.6 m, 1.0 m, 2.0 m and 6.0 m. The heat release rate input for the model was determined using the measured fuel regression rate multiplied by the heat of combustion.

Raj [30] reported gas temperature and velocity measurements for a very large scale JP-4 jet fuel unobstructed pool fire with a diameter of D=15.24 m and fire heat release rate of Q=570 MW. The centerline gas temperature was measured at different elevations above the fuel surface. The gas velocity was measured at a height of 5.73 m above the pool using a high temperature anemometer with an accuracy of 13%.

3.3.1.2 Heat Fluxes

Blanchat et al. [13] performed four large scale open pool fire experiments with different wind conditions. The pool was 7.92 m diameter with JP-8 used for fuel. The heat flux to objects immersed within the flaming region was measured with two small cylindrical calorimeters placed 0.16 m above the ground plane surface. Each small calorimeter was made of stainless steel with a 0.305 m outside diameter, 0.406 m long, 3.0 mm wall thickness and 64 mm thick stainless steel end caps. The inside of the cylinder was packed with ceramic fiber insulation. The stainless steel temperatures were measured using six thermocouples attached on the inside surface: four at the half length equally distributed around the perimeter and one on each end cap. The incident heat fluxes to the heated surface were determined using the temperature histories and an inverse heat transfer model [32]. Calorimeters were located 1.52 m and 2.51 m from pool centerline.

3.3.2 Obstructed Fire

3.3.2.1 Gas Temperature, Velocity and Stagnation Point Heat Fluxes

Several studies [6, 9, 33, 34] have been conducted making measurements in the ceiling jet region of an impinging fire plume to evaluate the effects of fire heat release rate and ceiling height on thermal and flow conditions. For validation of the model, simulation results were compared with plume gas temperature, velocity, and stagnation point heat flux data taken in experiments with different ceiling heights and fire heat release rates.

Wasson [35] reported both gas temperature and velocity in the plume region beneath the ceiling as well as the stagnation point heat flux. The fire was produced from a propane fueled sand burner impinging on flat horizontal ceiling. The ceiling was constructed of 15.9 mm thick fire-resistant gypsum board supported on a steel structure. Measurements were made along the height at the centerline of the fire plume in 76 mm vertical intervals up to the ceiling. Measurements of gas temperature and gas velocity were made using an aspirated thermocouple probe and bi-directional probe, respectively. The standard heat flux (i.e., heat flux with the surface at 298 K) was measured at the impingement point of the flame on the ceiling with a hybrid heat flux gage. To evaluate the effect of fire heat release rate on the gas temperature, velocity and stagnation point heat flux, the study included the two different fire heat release rates with two different ceiling heights provided in Table 3-1.

Table 3-1: Fire diameter, heat release rate, and ceiling height for simulated experiments of Wasson [35].

Burner Dimension, (m×m)	**Fire Heat Release Rate, Q (kW)**	**Fuel Type**	**Ceiling Height, H (m)**	**Free Flame Height / Ceiling Height**
0.30 × 0.30	50	Propane	0.64	2.0
0.30 × 0.30	90	Propane	0.84	2.0

Heskestad and Hamada [33] performed a series of experiments with propane fueled fires impinging on a flat, horizontal ceiling. The ratio of free flame length to ceiling height ranged from 0.3 to 3.0. The ceiling was made with 12.7 mm thick marinate XL supported on a steel

structure. The temperatures were measured with 30-gauge, Type K thermocouples with 0.8 mm diameter bead and located beneath the ceiling at 2% of the ceiling height. To evaluate the effect of fire diameter and heat release rate on the stagnation point gas temperature, simulation results were compared with the three different fire heat release rates provided in Table 3-2.

Table 3-2: Fire diameter, heat release rate, and ceiling height of simulated experiments of Heskestad and Hamada [33].

Fire Diameter, D(m)	**Fire Heat Release Rate, Q(kW)**	**Fuel Type**	**Ceiling Height, H(m)**	**Free Flame Height / Ceiling Height**
0.30	185	Propane	0.92	1.74
0.61	382	Propane	1.51	1.27
0.61	764	Propane	1.51	1.81

3.3.3 Simulation Details

Simulations were conducted using FDS, Version 6.0 [26], which models the domain using a rectilinear grid. The dimensions of any physical obstruction in the model must conform to that of the underlying mesh. Due to this, the fuel or burner surface was modeled as a rectangular solid obstruction with the area of the top surface equal to the area of the actual fire diameter. The vents covering the top surface of the burner obstruction were prescribed a constant heat release rate per unit area (HRRPUA) to provide the desired fire heat release rate. For liquid pools, the inlet temperature was set equal to the boiling point of the fuel type simulated. All FDS simulations were performed using the default turbulence model proposed by Deardorff [36] using default parameters.

A convergence study was performed on each individual validation scenario in this work. Floyd *et al*. [37] recommended that the ratio of characteristic fire diameter and cell size, $D^*/\delta x$, should be used to determine the appropriate grid size, with δx being the computational cell size and D^* defined as

$$D^* = \left(\frac{\dot{Q}}{\rho_\infty c_p T_\infty \sqrt{g}}\right)^{2/5} \quad (6)$$

where $\dot{Q}$ is the heat release rate (kW), ρ_∞ is the ambient air density (kg/m^3), c_p is the specific heat of air (kJ/kg-K), T_∞ is the ambient air temperature (K) and g is the gravitational acceleration (m/s^2). A typical result from the convergence study is shown in Figure 3-3 for a 6.0 m diameter heptane pool fire with different cell sizes. For this case, 10 cells across the diameter (cell size = 0.6 m) provide a converged result except close to the fuel surface. The 20 cell result was used since it produced the best agreement with experimental data, particularly at the near field. In general, the benchmarking in this study indicates that more cells are required across the diameter as the fire diameter increases. For example, it was found that 10 cells across the diameter are required to accurately predict the far field gas temperature and velocity for a fire size of 1,500 kW and a fire diameter of 1.0 m. However, 30 cells across the diameter are required to predict the larger fire sizes of 570 MW and a fire diameter of 15.0 m. For larger fires, it is believed that more cells are required across the diameter to sufficiently resolve the turbulent structures that drive the mixing in the flaming region.

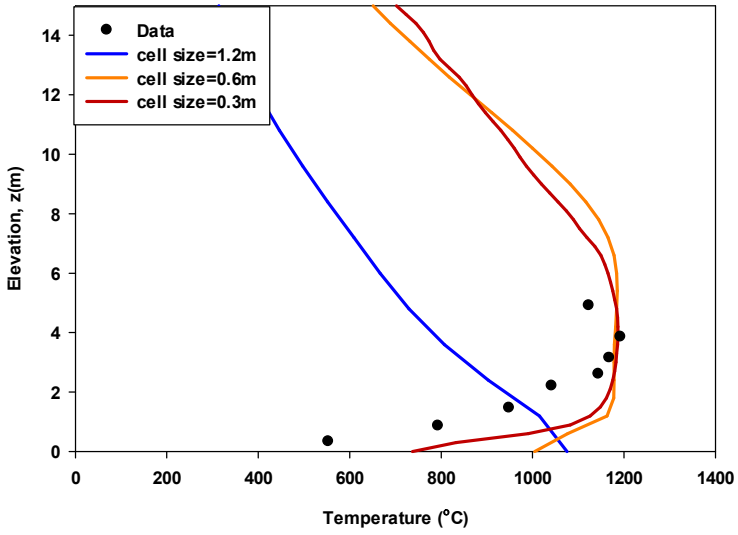

Figure 3-3: Centerline temperature rise as a function of cell size for a 6.0m diameter heptane pool fire.

The details of the computational domain and burner for all the simulations conducted are provided in Table 3-3. All domain boundaries were set to an open condition. The ceiling [33,35] and the calorimeter [13] were constructed of gypsum board and steel, respectively, using the thermo-physical properties provided in Table 3-4. All FDS simulations were performed on a

standard x86-Linux cluster with a dual-socket quad-core 2.26 GHz Intel Nehalem processor and 24GB of memory.

Gas temperature and velocity were extracted from the simulations by locating slices along the centerline of the burner. In addition, standard heat fluxes to the ceiling and heat fluxes onto the calorimeters were extracted from the simulations by locating heat flux devices at the locations where measurements were made in the tests. Gas temperature, velocity and standard heat flux reported in the results section are time averages over a 180 s period following the initial 60 s of the simulation. For the cases simulated, the fire was determined to reach a quasi-steady state following this initial 60 s period.

Table 3-3: Dimension of the computational domain, physical obstructions, heat release rate and fuel type for FDS simulations.

Validation study	**Heat release rate (kW)**	**Fuel type**	**Computational domain (m)**			**Burner (m)**			**Cell size (cm)**	$D^*/cell\ size$	$D/cell\ size$
			Height	Width	Depth	Height	Width	Depth			
Koseki[31]											
D=0.6m	420	Heptane	4.0	4.0	4.25	0.54	0.54	0.10	0.067	10	9
D=1.0m	1500	Heptane	5.5	5.5	8.25	0.88	0.88	0.11	0.11	10	9
D=2.0m	8670	Heptane	9.8	9.8	12.6	1.8	1.8	0.20	0.20	11	10
D=6.0m	97000	Heptane	15.6	15.6	24.6	5.6	5.6	0.30	0.30	20	20
Raj[30]											
D=15.0m	570000	JP-8	42	42	63	13	13	2	0.50	24	30
Blanchat[13]											
D=7.92m	124000	JP-8	16.0	16.0	27.0	7.0	7.0	0.50	0.25	26	31
Klassen[29]											
D=0.3m	126	Heptane	2.48	2.48	2.72	0.28	0.28	0.12	0.04	10	7
Wasson[35]											
D=0.34m	50	Propane	1.99	1.99	1.41	0.30	0.30	0.10	0.03	10	11
D=0.34m	90	Propane	1.96	1.96	1.41	0.30	0.30	0.10	0.035	10	9
Heskestad[33]											
D=0.30m	185	Propane	5.7	5.7	1.7	0.30	0.30	0.10	0.053	10	5
D=0.61m	382	Propane	5.16	5.16	2.22	0.54	0.54	0.12	0.06	10	10
D=0.61m	764	Propane	5.20	5.20	2.32	0.56	0.56	0.16	0.08	10	7

Table 3-4: Thermo-physical properties of ceiling and calorimeter material.

Material	Specific heat (kJ/kg-K)	Conductivity (W/m-K)	Density (kg-m3)	Emissivity
Steel	0.465	54.0	7850.0	0.9
Gypsum board	0.9	0.16	790	0.3

3.4 Results

Simulation results are provided in the following sections and compared with experimental data from the literature. This was performed to benchmark the model with available data from fire testing as well as demonstrate the modeling approach.

3.4.1 Unobstructed Fire

3.4.1.1 Gas Temperature and Velocity

Gas temperature predictions for fire diameters of D = 0.6m, 1.0m, 2.0m, 6.0m and 15.0m are provided in Figures 3-4 and 3-5. The correlation proposed by McCaffrey [4] is also shown in the figures as a reference. As seen in Figures 3-4 and 3-5, below a dimensionless height (z/D) of 0.15 the gas temperature predictions were within 25% of the data. Note the proposed modeling approach does capture the correct trend in an increasing gas temperature with an increase in fire diameter with a maximum gas temperature of 900°C for D=0.6 m, 1000°C for D=1.0 m and 1200°C for D=6.0 m. As expected, the McCaffrey correlation agrees well with the gas temperatures for the smaller fires (less than 1.0 m in diameter) while it under predicts the gas temperatures for larger fires.

Figures 3-6 and 3-7 contain the gas velocity predictions compared with data for the fire diameter of D = 0.6m, 1.0m, 2.0m, 6.0m, and 15.0m along with the correlation proposed by McCaffrey [4]. The predicted gas velocity agrees to within 25% of the data above a height of z/D = 0.35. It is also noted that gas velocity increases with an increase in fire diameter and the proposed modeling approach predicts this trend.

3.4.1.2 Heat Flux

Predicted and measured heat fluxes onto an object immersed in a 7.92 m diameter pool fire are provided in Figure 3-8. Blanchat *et al*. [13] measured heat fluxes on six locations of the calorimeter for four separate fires having different wind conditions. The simulation was

conducted with no wind; therefore, the results were compared with the data obtained from Test-1 with a wind speed of 0.85 ± 0.27 m/s. Overall, the predictions provide the correct trends and are within the range of the standard deviation in the test results. This demonstrates the ability of the proposed modeling approach to predict the variation in the fire exposure with radial distance inside the fire plume. The heat flux onto the bottom surface of the calorimeter is lower than that on the top surface. This is attributed to the bottom surface exchanging radiation with the fuel surface (at the fuel boiling point temperature), which is significantly lower temperature compared with the flame. The model is also able to predict this trend correctly.

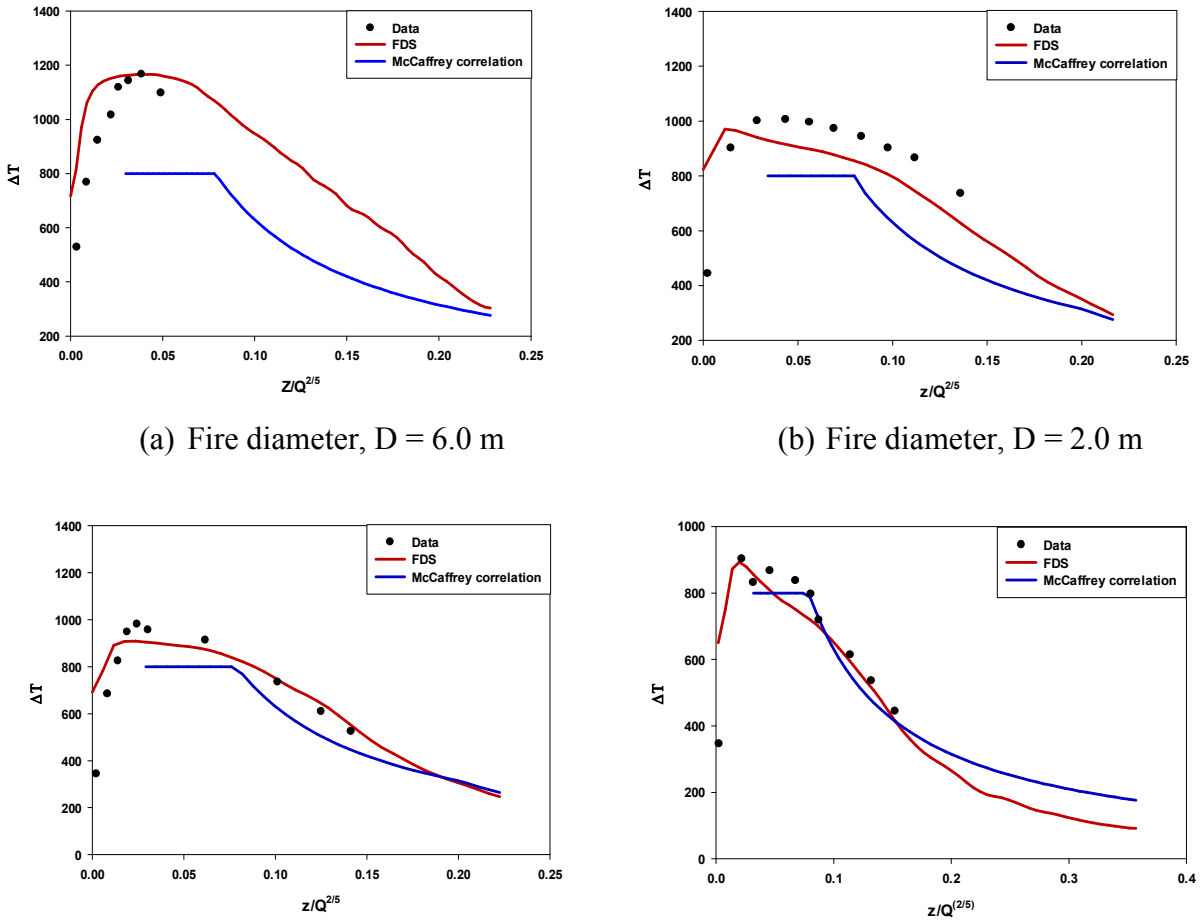

(a) Fire diameter, D = 6.0 m

(b) Fire diameter, D = 2.0 m

(c) Fire diameter, D = 1.0 m

(d) Fire diameter, D = 0.6m

Figure 3-4: Gas temperature profile in the flaming region for different unobstructed pool fire diameters.

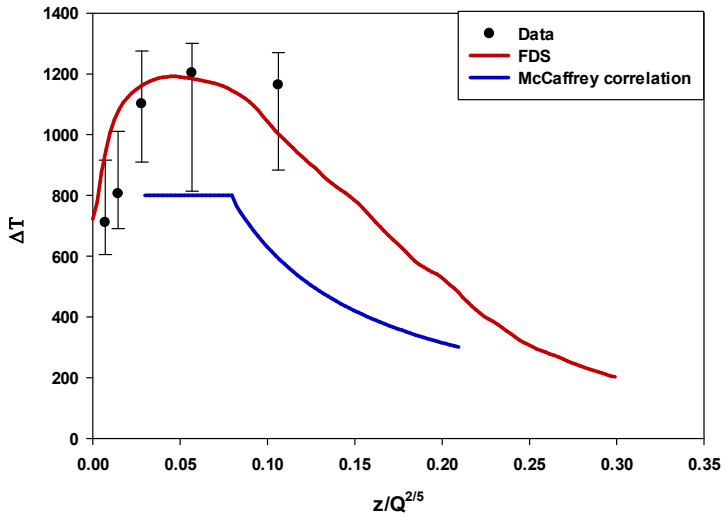

Figure 3-5: Gas temperature profile in the flaming region of an unobstructed pool fire with D=15.0 m (Raj,1980).

3.4.2 Obstructed Fire

3.4.2.1 Gas Temperature, Gas Velocity and Stagnation Point Heat Flux

Simulations were performed with a 90 kW fire located below a 0.64 m high flat ceiling that the fire impinges onto and then flows radially out along as a ceiling jet. Predicted and measured gas temperature and velocity along the height of a fire plume at the centerline prior to impinging onto the ceiling are shown in Figure 3-9 while the heat flux onto the ceiling at the impingement location is provided in Figure 3-10. The data in the figures are from experiments conducted by Wasson [35] with a propane fueled sand burner. The model agrees within 15% with gas velocity data, but the model over predicts the gas temperature data by 25% and under predicts the standard heat flux data by 18%. The deviation in the measured and predicted gas temperatures is attributed to the large scatter in radiative fraction for smaller diameter fires as seen in Figure 3-2. However, the deviation in standard heat flux prediction is attributed to using the default convective heat transfer coefficient used in FDS. The effects of this are further explained in the discussion section.

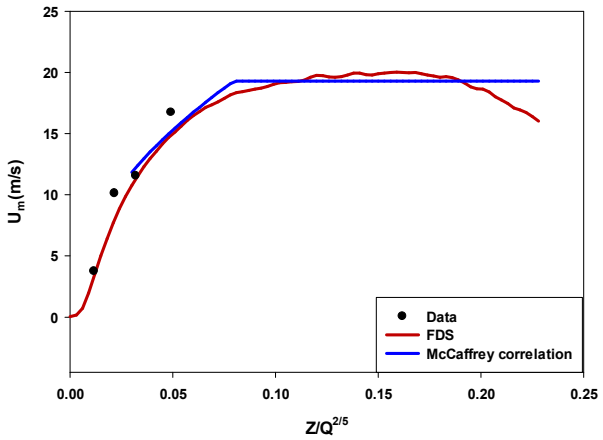

(a) Fire diameter, D = 6.0 m

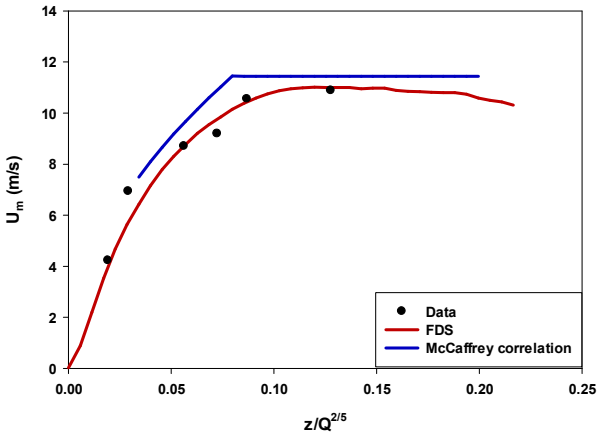

(b) Fire diameter, D = 2.0 m

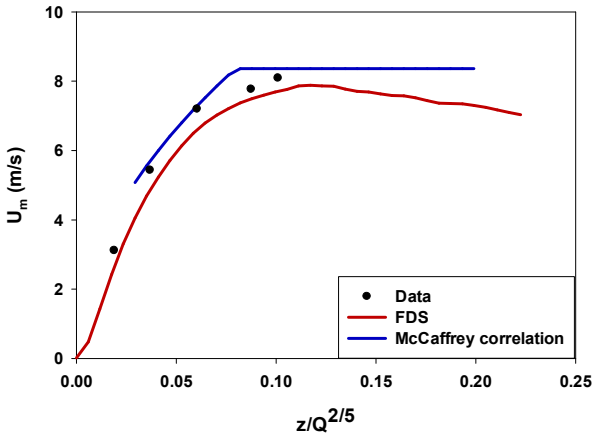

(c) Fire diameter, D = 1.0 m

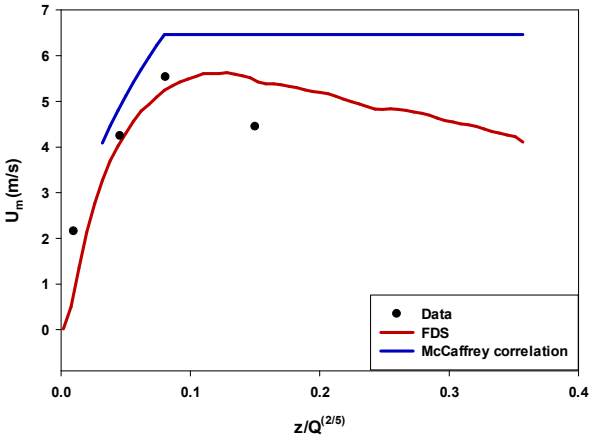

(d) Fire diameter, D = 0.6m

Figure 3-6: Centerline gas velocity profile in different flame regime for different open pool fire diameter.

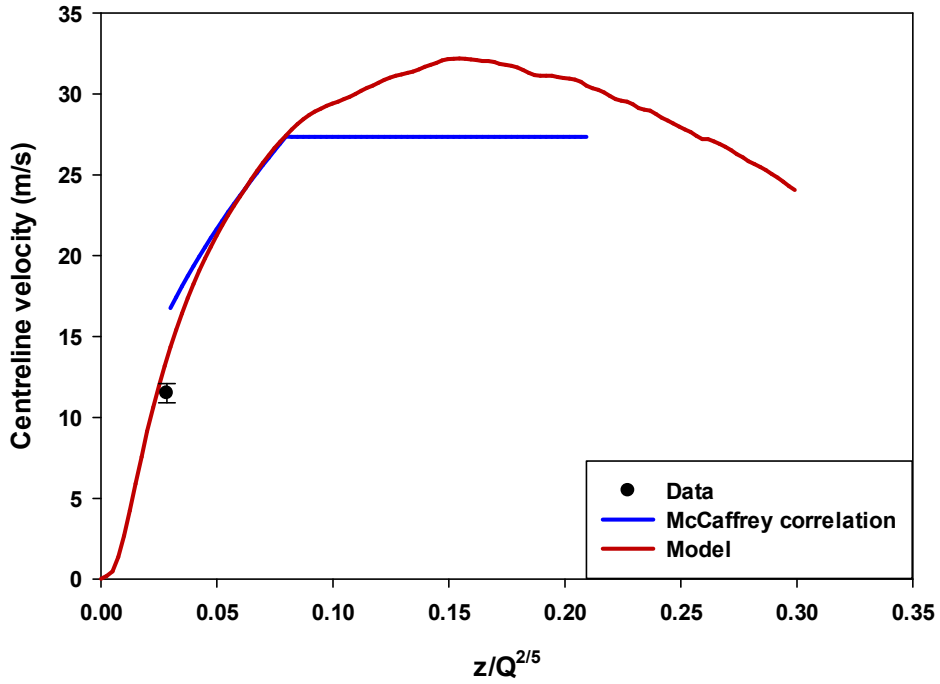

Figure 3-7: Vertical gas temperature profile of open pool fire diameter, D=15.0 m

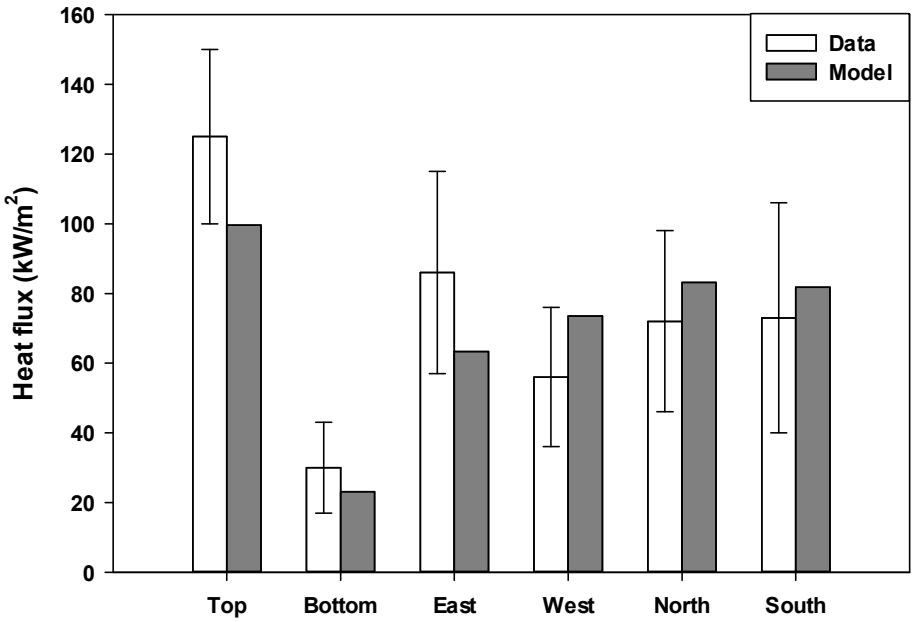

Figure 3-8: Heat flux to an object immersed in a 7.92 m diameter pool fire compared with data measured by Blanchat *et al*. [13].

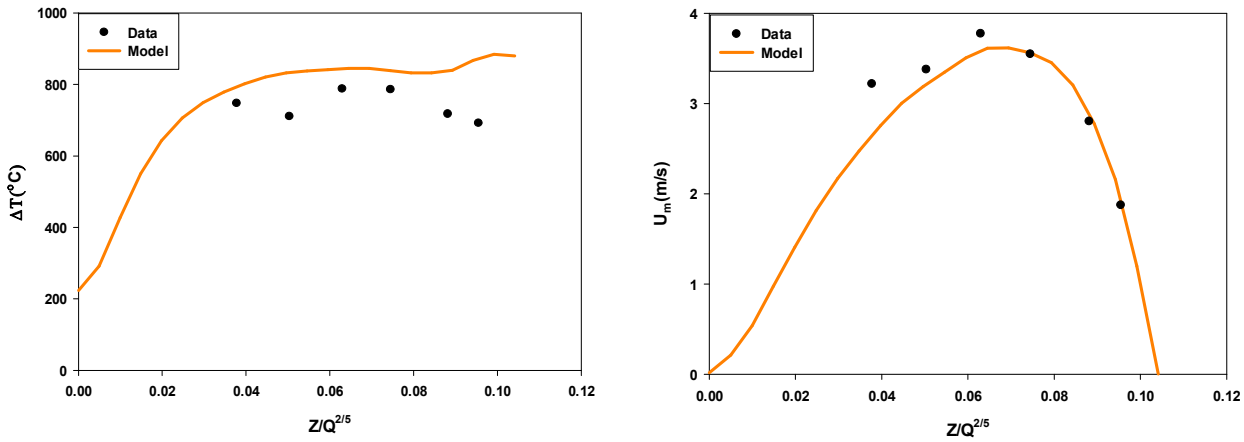

(a) (b)

Figure 3-9: Predicted (a) gas temperature and (b) velocity vertically along the centerline of a fire plume compared with data measured by Wasson [35].

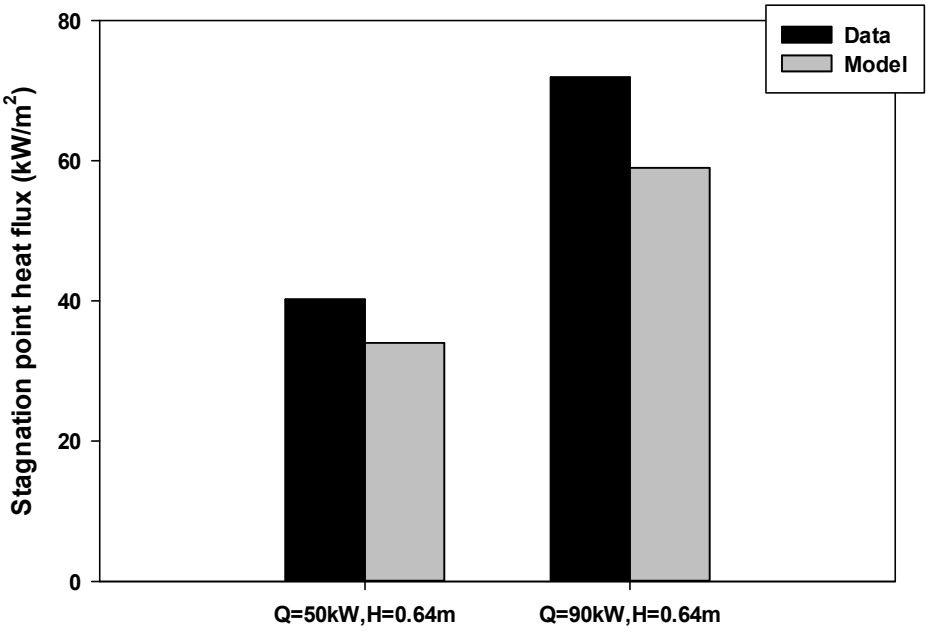

Figure 3-10: Prediction of heat flux at the impingement point compared with data measured by Wasson [35].

A series of simulations were performed to predict the gas temperature at the impingement point of a fire plume impinging on a flat ceiling made of Marinite XL. Simulations were conducted on different fire heat release rates and diameters as described in Table 3-2. A comparison of the predicted and measured [33] gas temperatures are provided in Figure 3-11. As seen in the figure, the model predicts the gas temperature within 12% of the measured data except for the case with a heat release rate of Q = 382 kW where the difference was 43%. The reason for the discrepancy is unknown; however the model predicts the correct trend.

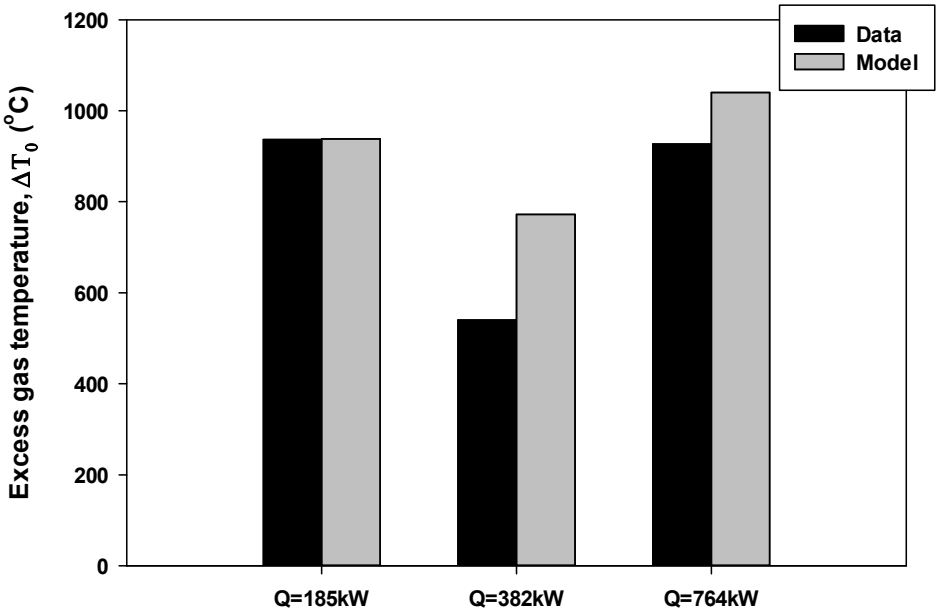

Figure 3-11: Impingement point excess gas temperature prediction of ceiling jet driven by a strong plume with data measured by Heskestad and Hamada [33].

3.5 Discussion

The predictive capability of using the radiative fraction as a function of fire diameter to account for the effects in the increase of soot for a range of fire diameters (0.3 m – 15 m) was further evaluated by comparing the current modeling with other CFD simulation results that include detailed soot formation / oxidation models reported in the literature. In addition, the

effects of heat transfer coefficient on the heat fluxes to the objects during a fire exposure are also discussed.

Figure 3-12 provides a comparison of results from the FDS model using the radiative fraction methodology proposed in this paper along with other fire models reported in the literature that include soot formation and oxidation [20, 23, 40, 41]. Results in Figure 3-12 are for the centerline gas temperature of a heptane fueled 0.3 m diameter fire conducted by Klassen and Gore [29]. Gas temperatures were measured using Type K thermocouples at five different locations along the centerline of the pool. From the results in Figure 3-12, the current model predicts the gas temperature of the heptane pool fire as well as or better than the other more sophisticated models. The other proposed models include complex mechanisms for soot formation and oxidation that require numerous input parameters and have only been validated on fire diameters up to 0.3 m. The approach proposed in this paper has been shown to be capable of predicting thermal and flow conditions for small diameter fires (<1.0 m) to larger diameter fires (up to 15.0 m) where soot formation increases resulting in higher gas temperatures.

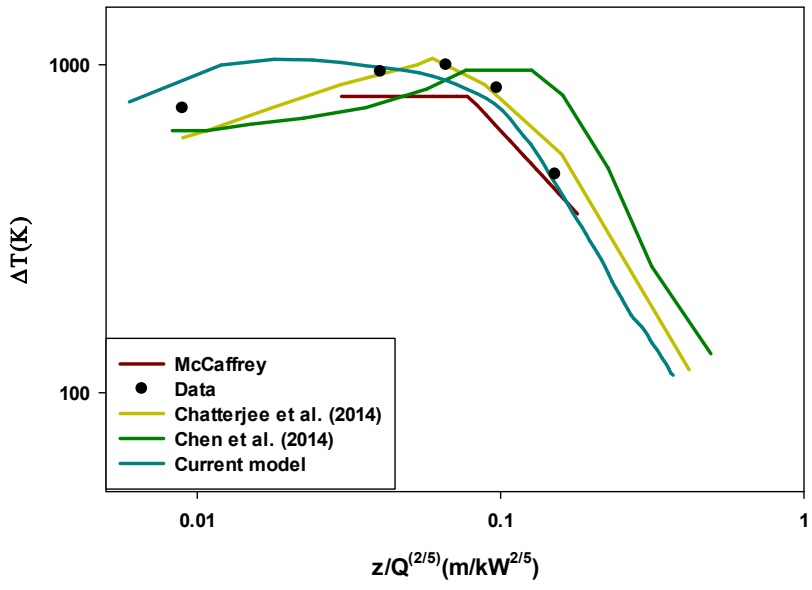

Figure 3-12: Prediction of centerline gas temperature of a heptane fueled 0.3m diameter fire using different models.

The FDS model used in this study includes the radiative fraction scaled with fire diameter. The amount of energy radiated away from the fire depends both on the fire diameter and fuel type. For a particular fire diameter, a hydrocarbon fuel such as propane will produce a small amount of soot whereas liquid fuels such as JP-8 will produce more soot. As seen in Figure 3-2, depending on the fuel type the amount of energy radiated away from the fire varies from 0.3 to 0.49 for fire diameters smaller than 1.0 m with the proposed fit providing a value of 0.42. For fire diameters of greater than 1.0 m, the fire gases become optically thick. As a result the radiative fraction becomes a function of fire diameter only. Figure 3-13 provides predicted gas temperatures using the upper and lower range of the radiative fraction as well as the proposed fit value in simulations on a 0.3 m diameter propane fuel fire from Wasson [35]. From results in Figure 3-13, the model with a radiative fraction of 0.3 which is commonly used as the default value in fire calculations (especially for clean burning gaseous fuels such as propane) over predict the data by 25%. Simulations using radiative fraction values of 0.42 and 0.49 provide results that predict the data to within 15%. This further demonstrates that the proposed curve of radiative fraction scaled with the fire diameter will accurately predict the gas temperature.

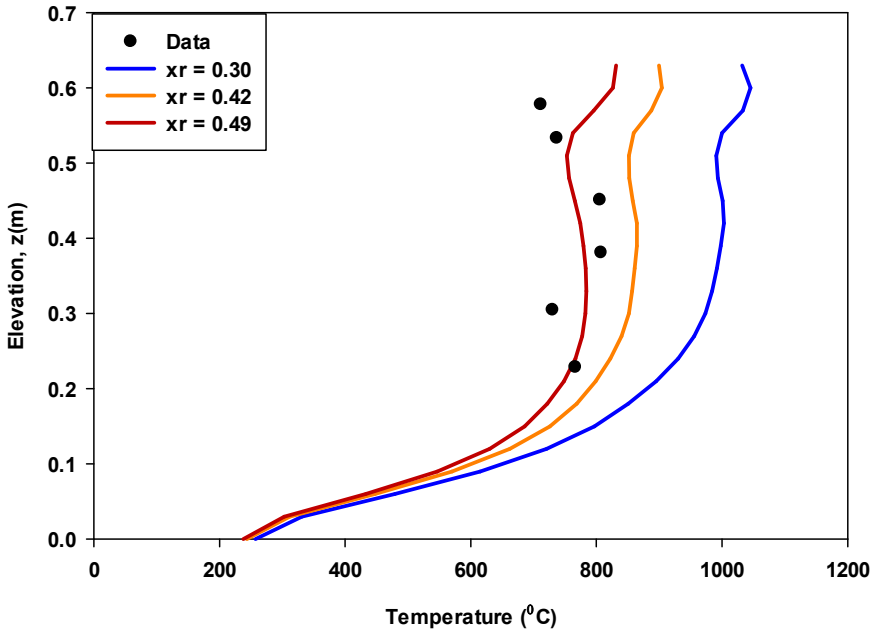

Figure 3-13: Comparison of measured [31] gas temperature with model predictions using different values of radiative fraction with propane fuel.

The standard heat fluxes onto surfaces were used to compare the experimental and simulation results. Standard heat flux can be calculated using the following relation :

$$q''_{Std} = q''_{rad} + q''_{conv} + \varepsilon_{gauge}\sigma(T_s^4 - T_\infty^4) + h_c(T_s - T_\infty) \quad (8)$$

where, q''_{Std} is the heat flux with the surface at standard temperature (kW/m^2), q''_{rad} is the radiative heat flux with the surface at elevated temperature T_s (kW/m^2), q''_{conv} is the convective heat flux with the surface at elevated temperature T_s (kW/m^2), ε_{gauge} is the gauge emissivity, T_s is the surface temperature (K), T_∞ is the reference temperature (298K), h_c is the convective heat transfer coefficient (kW/m^2-K).

Radiation is known to play a dominant role in heat transfer from fires to surfaces; however, convection can also be significant in scenarios where the flow conditions promote a high heat transfer coefficient such as the impingement region. FDS by default uses a convection heat transfer coefficient calculated based on natural and forced flow convection. Accurate prediction of the standard heat flux is sensitive to the convective heat transfer coefficient, especially in impingement regions where the convective heat transfer coefficient is larger compared with flow over a flat surface. In the case with the fire impinging onto a ceiling [35], FDS predicted the heat transfer coefficient to be h_c=9.6 W/m^2-K and 8 W/m^2-K for the fire size of 50kW and 90kW, respectively, while a value of approximately 25 W/m^2-K was needed to match the measured heat flux value as shown in Figure 3-14. For the geometry tested by Wasson [35], Wasson [35], Weng and Hasemi [42], Donaldson *et al.* [43] predict the value to range from 32-60 W/m^2-K with an average of 50 W/m^{2}K, which are higher than needed to match the predicted and measured heat fluxes. The over prediction of the results using the expected heat transfer coefficient is attributed to FDS over predicting the gas temperature in this scenario as shown in Figure 3-9. Better heat transfer coefficient correlations are needed to improve the accuracy of the heat flux predictions, especially for impinging flames.

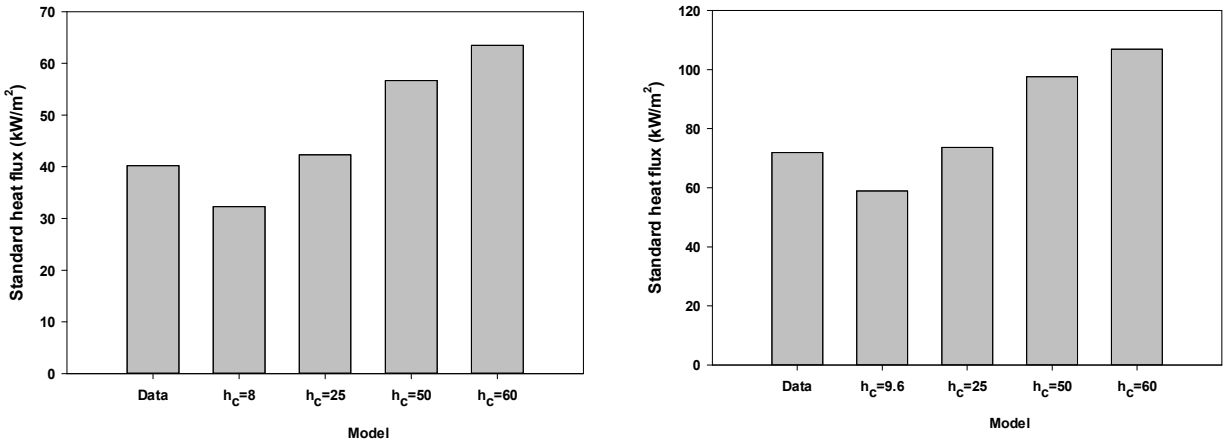

(a) (b)

Figure 3-14: Comparison of measured [35] standard heat flux with predicted heat flux using different values of convective heat transfer coefficient for a) 50 kW and b) 90kW fires.

3.6 Conclusion

A methodology was developed to predict the fire conditions and exposure heat flux onto adjacent surfaces using FDS for fires having diameters ranging from 0.3 – 15.0 m. With an increase in fire diameter, the soot production from the fire increases forming a soot mantle that blocks more radiation from leaving the fire and increasing the gas temperature. The effect was accounted for in the modeling by assigning the radiative fraction of the fire based on the fire diameter.

The fire conditions predicted using FDS including the appropriate radiative fraction was compared with gas temperature and velocity measured for a range of fire diameters with and without obstructions. When including this, FDS predicted gas temperature and velocity to within 22% of measured data. The proposed modeling methodology was also used to predict the heat transfer to objects immersed in flames and to a ceiling directly above the fire. Heat flux predictions were within 18% of the measured values, which was within the experimental uncertainty.

The proposed method produced similar predictions of gas temperature and velocity compared with other fire models containing detailed soot formation and oxidation models given in the literature for fires having a diameter of 0.3 m. Compared with these other methods, the

radiative fraction approach allows for a simple method to account for the effect of changes in soot production with the scale of fire which is not computationally expensive. More accurate heat transfer coefficients in FDS can improve predicted heat fluxes, especially for cases where the fire is impinging onto the surface.

3.7 References

[1] J. X. Wen, K. Kang, T. Donchev, and J. Karwatzki, "Validation of FDS for the prediction of medium-scale pool fires," *Fire Safety Journal,* vol. 42, pp. 127-138, 2007.

[2] Y. Xin, S. Filatyev, K. Biswas, J. Gore, R. Rehm, and H. Baum, "Fire dynamics simulations of a one-meter diameter methane fire," *Combustion and Flame,* vol. 153, pp. 499-509, 2008.

[3] J. Floyd, G. Forney, S. Hostikka, T. Korhonen, R. McDermott, and K. McGrattan, "Fire Dynamics Simulator Technical Reference Guide-Volume 3: Validation," *National Institute of Standards and Technology: Gaithersburg, Maryland, USA,* 2013.

[4] B. J. McCaffrey, *Purely buoyant diffusion flames: some experimental results*, 1979.

[5] G. Cox and R. Chitty, "Some source-dependent effects of unbounded fires," *Combustion and Flame,* vol. 60, pp. 219-232, 1985.

[6] H.-C. Kung and P. Stavrianidis, "Buoyant plumes of large-scale pool fires," in *Symposium (International) on Combustion*, 1982, pp. 905-912.

[7] Y. Hasemi and T. Tokunaga, "Flame geometry effects on the buoyant plumes from turbulent diffusion flames," *Fire Science and Technology,* vol. 4, pp. 15-26, 1984.

[8] C. Beyler, "Fire plumes and ceiling jets," *Fire Safety Journal,* vol. 11, pp. 53-75, 1986.

[9] R. L. Alpert, "Turbulent ceiling-jet induced by large-scale fires," *Combustion Science and Technology,* vol. 11, pp. 197-213, 1975.

[10] H. Baum and B. McCaffrey, "Fire induced flow field–theory and experiment," in *Fire Safety Science–Proceedings of the Second International Symposium*, 1989, pp. 129-148.

[11] M. Schneider and L. A. Kent, "Measurements of gas velocities and temperatures in a large open pool fire," *Fire Technology,* vol. 25, pp. 51-80, 1989.

[12] H. Koseki, "Large scale pool fires: Results of recent experiments," in *Proceedings of the 6th International Symposium of Fire Safety Science*, 1999, pp. 5-9.

[13] T. Blanchat, V. Nicolette, W. Sundberg, and V. Figueroa, "Well-characterized open pool experiment data and analysis for model validation and development," *SAND2006-7508,* 2006.

[14] G. Markstein, "Relationship between smoke point and radiant emission from buoyant turbulent and laminar diffusion flames," in *Symposium (International) on Combustion*, 1985, pp. 1055-1061.

[15] M. Delichatsios, "A phenomenological model for smoke-point and soot formation in laminar flames," *Combustion Science and Technology,* vol. 100, pp. 283-298, 1994.

[16] C. W. Lautenberger, "CFD simulation of soot formation and flame radiation," WORCESTER POLYTECHNIC INSTITUTE, 2002.

[17] T. Beji, J. Zhang, W. Yao, and M. Delichatsios, "A novel soot model for fires: validation in a laminar non-premixed flame," *Combustion and Flame,* vol. 158, pp. 281-290, 2011.

[18] P. Chatterjee, J. L. de Ris, Y. Wang, and S. B. Dorofeev, "A model for soot radiation in buoyant diffusion flames," *Proceedings of the Combustion Institute,* vol. 33, pp. 2665-2671, 2011.

[19] A. T. Modak, "Radiation from products of combustion," *Fire Safety Journal,* vol. 1, pp. 339-361, 1979.

[20] Z. Chen, J. Wen, B. Xu, and S. Dembele, "Large eddy simulation of a medium-scale methanol pool fire using the extended eddy dissipation concept," *International Journal of Heat and Mass Transfer,* vol. 70, pp. 389-408, 2014.

[21] P. Joulain, "The behavior of pool fires: state of the art and new insights," in *Symposium (International) on Combustion*, 1998, pp. 2691-2706.

[22] G. Markstein and J. De Ris, "Radiant emission and absorption by laminar ethylene and propylene diffusion flames," in *Symposium (International) on Combustion*, 1985, pp. 1637-1646.

[23] P. Chatterjee, Y. Wang, K. V. Meredith, and S. B. Dorofeev, "Application of a subgrid soot-radiation model in the numerical simulation of a heptane pool fire," *Proceedings of the Combustion Institute,* 2014.

[24] W. Yao, J. Zhang, A. Nadjai, T. Beji, and M. Delichatsios, "Development and validation of a global soot model in turbulent jet flames," *Combustion Science and Technology,* vol. 184, pp. 717-733, 2012.

[25] W. Yao, J. Zhang, A. Nadjai, T. Beji, and M. A. Delichatsios, "A global soot model developed for fires: Validation in laminar flames and application in turbulent pool fires," *Fire Safety Journal,* vol. 46, pp. 371-387, 2011.

[26] J. Floyd, G. Forney, S. Hostikka, T. Korhonen, R. McDermott, and K. McGrattan, "Fire Dynamics Simulator User's Guide," *Gaithersburg, Maryland, USA,* 2013.

[27] M. Munoz, E. Planas, F. Ferrero, and J. Casal, "Predicting the emissive power of hydrocarbon pool fires," *Journal of hazardous materials,* vol. 144, pp. 725-729, 2007.

[28] K. B. McGrattan, H. R. Baum, and A. Hamins, "Thermal radiation from large pool fires," *NISTIR-6546, NIST, Gaithersburg, Md., USA,* 2000.

[29] M. Klassen and J. Gore, *Structure and radiation properties of pool fires*: US Department of Commerce, National Institute of Standards and Technology, 1994.

[30] P. Raj, "Analysis of NASA JP-4 fire tests data and development of a simple fire model," 1980.

[31] H. Koseki, Y. Iwata, Y. Natsume, T. Takahashi, and T. Hirano, "Tomakomai large scale crude oil fire experiments," *Fire Technology,* vol. 36, pp. 24-38, 2000.

[32] T. K. BLANCHAT, L. L. HUMPHRIES, and W. GILL, "Sandia heat flux gauge thermal response and uncertainty models," Sandia National Labs., Albuquerque, NM, and Livermore, CA (US)2000.

[33] G. Heskestad and T. Hamada, "Ceiling jets of strong fire plumes," *Fire Safety Journal,* vol. 21, pp. 69-82, 1993.

[34] Y. Hasemi, S. Yokobayashi, T. Wakamatsu, and A. Ptchelintsev, "Firesafety of building components exposed to a localized fire: scope and experiments on ceiling/beam system exposed to a localized fire," *Proceedings of ASIAFLAM,* pp. 351-361, 1995.

[35] R. A. Wasson, "Separation of the Heat Transfer Components for Diffusion Flames Impinging onto Ceilings," Virginia Tech, 2014.

[36] J. W. Deardorff, "Stratocumulus-capped mixed layers derived from a three-dimensional model," *Boundary-Layer Meteorology,* vol. 18, pp. 495-527, 1980.

[37] K. McGrattan, S. Hostikka, J. Floyd, W. Mell, and R. McDermott, "Fire dynamics simulator, technical reference guide, volume 1: mathematical model," *NIST Special Publication,* vol. 1018, 2013.

[38] L. G. Blevins and W. M. Pitts, "Modeling of bare and aspirated thermocouples in compartment fires," *Fire Safety Journal,* vol. 33, pp. 239-259, 1999.

[39] W. M. Pitts, E. Braun, R. D. Peacock, H. E. Mitler, E. Johnson, P. A. Reneke, and L. G. Blevins, "Temperature uncertainties for bare-bead and aspirated thermocouple measurements in fire environments," *ASTM Special Technical Publication,* vol. 1427, pp. 3-15, 2003.

[40] P. Chatterjee, J. L. De Ris, Y. Wang, N. Krishnamoorthy, and S. B. Dorofeev, "Laminar Smoke Point Based Subgrid Soot Radiation Modeling Applied to LES of Buoyant Turbulent Diffusion Flames," in *Journal of Physics: Conference Series*, 2012, p. 012009.

[41] Z. Chen, "Extension of the eddy dissipation concept and laminar smoke point soot model to the large eddy simulation of fire dynamics," Kingston University, 2012.

[42] W. G. Weng, Y. Hasemi, “Heat transfer to an unconfined ceiling from an impinging buoyant diffusion flame,” Heat and Mass Transfer, vol. 42, pp. 652-659, 2006

[43] C. D. Donaldson, R. S. Snedeker, D. P. Martgolis, “A study of free jet impingement. Part 2. Free jet turbulent structure and impingement heat transfer,” Journal of Fluid Mechanics, vol. 45, pp. 477-512, 1971.

4 Thermo-structural Response of Steel Bridge Elements Exposed to Large Localized Vehicle Fire

4.1 Introduction

In recent years, a number of highway bridge fires have occurred throughout the USA and the rest of the world with sometimes catastrophic outcomes including those in Birmingham, Alabama with one death [1, 2] and the complete collapse of the bridges located in Oakland, CA and Hazel Park, MI [2]. The main reasons for the catastrophic outcome are that some vehicles contain a very fuel load such as seats made of polyurethane foam and hydrocarbon fuel contained in the fuel tank. Despite the frequency of occurrences and the severity of highway bridge fire incidents [3], fire has been neglected as one of the primary extreme event limit states in the highway bridge design codes [4]. This is in part due to the difficulty in simulating these large fires as well as the thermo-structural response. As a result, there is still little understanding of the thermo-structural response of highway bridge structural elements exposed to vehicle fires.

Predicting the behavior of highway bridge structural elements during a fire exposure is a multi-physics problem that involves the vehicle fire exposure as well as the thermal and structural response of both the steel girders and concrete deck. Similar fire exposures are possible in other transportation related infrastructure such as tunnels and parking garages, which have previously received more attention. A large focus has been on the hazards associated with vehicle fires in tunnels due to the life safety issues and potential severity of fires [5-8]. The characteristics of tunnel fires have been documented including vehicle heat release rate, flame extension along the tunnel from the burning vehicle, gas temperatures along the tunnel, and ceiling lining material temperature rise with time [8, 9]. However, the findings from tunnel fire studies cannot be applied to highway bridge scenarios due to tunnel boundaries partially confining the fires as well as a restriction in ventilation to the fire resulting in long flame extensions along the tunnel. In addition, tunnel interior surfaces become heated causing an increase in heat transfer back to the vehicle enhancing burning, higher gas temperatures, and higher heat fluxes to tunnel surfaces. In contrast, fire exposures onto highway bridges are large scale fires that are only partially obstructed. As a result, there is typically more air available for burning, the surfaces of the bridge have less impact on the burning of the vehicle compared with tunnel fires, and the exposure heat fluxes may not be as extreme as those in tunnel fires. In

addition, the main structural components of highway bridges (e.g., the steel girders) commonly do not have fire protection. Some tests were conducted on parking garage fires, which are somewhat similar to the highway bridge scenario [9]. Parking garage fires are obstructed fires but have access to large amounts of air. The fire exposures in these studies were limited to car fires, which has a heat release rate of less than 10 MW [10]. For bridge scenarios, larger trucks present the most significant hazards such as a fuel tanker that can a heat release rate of 300MW [11]. Also, the analyses of parking garage fires has been limited to the determination of fire conditions, such as gas temperature and velocity, and not the heat transfer to the structural surfaces [9].

The thermo-structural response of shallow steel I-beams used in buildings have been tested in accordance with a standard, uniform fire exposure such as ISO 834 [12] and ASTM E119 [13] [14, 15]. The findings cannot be directly applied to assess the highway bridge fire hazard as the steel beams used in bridges are different than those used in buildings. Bridge girders are much deeper with thicker flanges and slender webs. Recently, Kodur [16] and Paya-Zaforteza [17] predicted the thermo-structural response of a short span steel girder with a standardized furnace exposure such as ISO 834 and UL 1709. Standardized furnace exposures are uniform exposures where the whole length of the beam is exposed to similar thermal conditions. Conversely, vehicle fire exposures produce a nonuniform thermal exposure on the structure. The flames and hot gases from vehicle fires will impinge on the lower flange of the girder and concrete deck between steel girders. After the impingement, flames will flow radially outward between the girders. The extension of the flame front will depend on the size of the fire and the relative position between the bridge and the fire source. This will create a temperature gradient along the length of the girder leading to a variation in the thermal and structural behavior. Thus the structural response of bridges under fire depends on the size of the fire, duration of the fire, and fire location relative to the bridge. The fire scenario to which bridges may be exposed ranges from a small car fire (2–9 MW)[18] to a large oil tanker fire (300MW). Some of the fires may not be threatening while the others may result in complete collapse of the bridge depending on the heat exposure from the vehicle fire onto the bridge structural elements. The majority of research on bridge element thermo-structural response during fires have used uniform standard fire exposures, while limited work has been performed to evaluate the effects of local fire exposures on bridge collapse [19-22]. A detailed study of the thermo-structural

response of bridges to different local fires with and without structural load has not been performed.

The large fire sizes associated with vehicle fires and the large dimensions of the bridge elements renders it difficult for experimental studies to be performed on highway bridge fire behavior. Therefore, it is of major importance to develop a modeling methodology to predict the thermo-structural response of highway bridge structural elements during large vehicle fire scenarios. Garlock et al. [2] and Kodur et al. [23] reviewed the literature on highway bridge fire hazards. In their study, they stated there is a lack of appropriate modeling methodology to simulate a bridge fire scenario and little understanding of the thermo-structural response of bridge structural member under realistic fire scenarios. Recently, some studies were conducted to predict the behavior of highway bridges under fire [21, 24-26, 47, 48]. Eisel et al [26] conducted a tanker fire simulation using the computational fluid dynamics code Fire Dynamics simulator (FDS) on Wiehltalbridge in Germany and found that flame temperature could reach as high as 1200°C [26]. Choi [21] conducted a simulation of a fuel tanker fire using the FDS to predict the temperature rise of a bridge exposed to a fuel tanker fire in an attempt to predict the events of the McCarthur Maze steel bridge over I-880, CA (April 29, 2007) exposed to fire. Fitted surface temperatures from FDS were imported into Abaqus, which was used to predict the structural response. Wright et al. [48] conducted a validation study of the fire behavior of I-65 overpass in Birmingham, AL. The effects of vehicle type and size, fire location and height of the bridge above the fire on the fire response of a typical highway bridge were also investigated. Alos-moya et al. [20] continued the study and conducted a numerical study of the fire response of I-65 overpass in Birmingham, AL, USA. The study also included an evaluation of the influence of three different fire exposures: i) CFD modeled tanker fire exposure, ii)the standard curve proposed by EC1 [28] and iii) the hydrocarbon fire curve proposed by EC1 [28] and live load on the fire response of a single steel girder with the fire source located at one end. The study highlights the need for an accurate fire model that accounts for the vehicle fire physics and non-uniform thermal exposures.

FDS is currently the most well validated computational fluid dynamics model [20] capable of predicting conditions during a bridge-vehicle fire scenario. Vehicle fires typically have an effective diameter of several meters, especially when a fuel spill is involved. It is well known that larger fires produce significant amounts of soot, especially around the periphery,

which blocks radiation loss to the surroundings causing higher gas temperatures for larger fires (D > 2 m) [46]. In order to use FDS to predict vehicle fires, the effects of soot production increase with fire diameter need to be included to predict gas temperatures and heat fluxes from the fire to the bridge structural elements. In addition, the heat fluxes predicted using FDS need to be mapped to the thermal and structural model to predict the bridge response.

A modeling approach is presented where FDS is used to predict large scale fire behavior and is coupled with Abaqus to predict the thermal and structural response of the bridge. FDS is sequentially coupled to Abaqus through a user subroutine that allows the heat fluxes from FDS to be mapped onto the elements of bridge surfaces in Abaqus for thermal prediction. These thermal model results in Abaqus are then sequentially coupled to a structural analysis within Abaqus for predicting structural behavior of the bridge during fire. The predicted heat exposure and temperature rise of elements due to a localized fire exposure as well as the deflection response of steel-concrete floor assembly is compared with available test data to demonstrate the ability of the methodology to account for localized fire and structural behavior of steel I beam-concrete assembly. The methodology is then used to predict the thermo-structural response of unprotected steel girder-concrete deck composite assembly exposed to a range of different size vehicle fires. Simulation results with a localized fire are compared with thermo-structural behavior predicted due to a standard furnace exposure.

4.2 Bridge Geometry and Fire Scenarios

The thermo-structural response of highway bridge structural elements during a fire exposure were studied on a real scale steel girder composite bridge deck exposed to different types of vehicle fires as well as a standard fire exposure. The evaluation with both vehicle and standardized furnace exposures will demonstrate the effect of temperature variation along the length of the long span girder on the bridge response during a fire.

4.2.1 Bridge Geometry

Analysis was performed on a multi-lane highway bridge with steel plate girders as shown in Figure 4-1. The bridge in Figure 4-1 is a typical multi-lane highway overpass bridge containing steel plate girders beneath a concrete deck, designed in accordance with the specifications of the Federal Highway Administration (FHWA). The multi-lane highway bridge consists of seven built in plate girders supporting a reinforced concrete slab 14.0 m wide, 37.0 m

long and 200 mm thick. The girders are assumed to be in full composite action with the slab and have an expansion joint at each end with a width of 72 mm. Each plate girder has a total of 34 stiffeners with a thickness of 25.4mm. The span length of the bridge is 37.0 m and the geometric definitions of the plate girder bridge are provided in Figure 4-1.

4.2.2 Fire Exposure

Fire scenarios for highway bridges include different types of burning vehicles which result in different fire heat release rates, duration, and diameters. As a result, four different types of vehicle fire scenarios were selected to evaluate the behavior of bridge structural elements during a fire. Including different types of vehicle fires allow for a comparison of the performance of the bridge structural elements for a range of fire severity. The types of vehicle fires considered in this study are provided in Table 4-1 along with the dimension of the vehicles and the peak heat release rate of the fire. Note that fires were oriented so that their length was perpendicular to the bridge span.

The analysis was performed using the time varying heat release rate curves for each vehicle fire shown in Figure 4-2. The heat release rate produced from a bus, heavy goods vehicle, box truck, and heavy goods vehicle (18 wheeler with a flatbed of stacked combustibles) fires with time were reported by Ingasson [5] and Babraskaus [10]. For the tanker fire scenario, no test data on the heat release rate with time was available in the literature. Due to this, the burning duration for the tanker fire scenario was calculated from the time required to burn all of the gasoline contained in a tanker. The tanker was assumed to carry 9,900 gallons of gasoline, which is the typical maximum volume. The heat release rate profile with time was then assumed to have an initial growth rate period of 3 minutes followed by a fully developed, constant heat release rate phase that persisted until all of the fuel was consumed. The steady state heat release rate for the gasoline burning was obtained from the pool fire burning rate relation, the fuel heat of combustion and fuel dimensions [18],

$$\dot{m}'' = \dot{m}''_{\infty} (1 - e^{-k\beta D}) \quad (1)$$

$$\dot{q} = \Delta h_c \, \dot{m}'' A \quad (2)$$

where $\dot{m}''$ is the pool mass loss rate (kg/m^2-s), $\dot{m}''_{\infty}$ is the infinite diameter pool mass loss rate (0.055 kg/m^2-s), k is the extinction coefficient (2.0 m^{-1}), D is the fuel diameter (m), β is the beam

length correction (1.05), Δh_c is the heat of combustion (44.7 MJ/kg), and A is the fuel surface area (m^2). The values provided in parenthesis are for gasoline [29]. All the simulations were conducted with the fire located at mid-span of the highway bridge. Based on results from a study evaluating the effects of fire location, it was found that a fire located at the mid-span is one of the worst case scenarios [48].

(a)

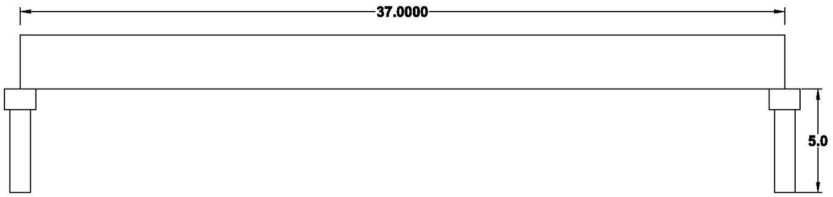

(b)

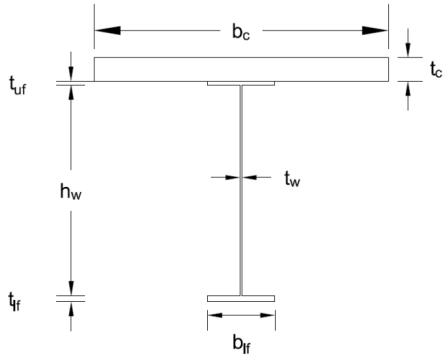

(c)

	(m)
b_c	14.0
t_c	0.2
t_{uf}	0.0254
b_{uf}	0.46
t_w	0.01
h_w	1.4365
t_{lf}	0.0381
b_{lf}	0.46

(d)

Figure 4-1: A typical multi-lane highway overpass bridge according to FHWA : a) top view, (b)elevation view, (c)cross-sectional view, (d) geometric definition of a typical girder. All dimensions in (m).

Standard time-temperature exposures inside furnaces are commonly used to assess the fire resistance of structural elements. The fire resistance of structural elements is defined as the ability of the element to maintain structural integrity and prevent heat transmission through the assembly. For the unprotected bridge application, the focus is on maintaining structural integrity only. The two different standardized furnace exposures used in this study included the cellulosic fire curve (ISO-834) [12] and the more severe hydrocarbon pool fire exposure (UL 1709) [28]. A plot of these time temperature curves is provided in Figure 4-3.

Table 4-1: Dimensions and peak heat release rates produced from different vehicle fires.

Vehicle Type	**Dimension**			**Peak Heat Release Rate (MW)**
	Length(m)	**Width(m)**	**Fire Elevation(m)**	
Bus	3.0	12.0	1.5	40
Box truck	3.0	10.5	1.0	100
Heavy goods vehicle	3.0	10.5	1.0	200
Tanker	6.5	14.0	0.5	294

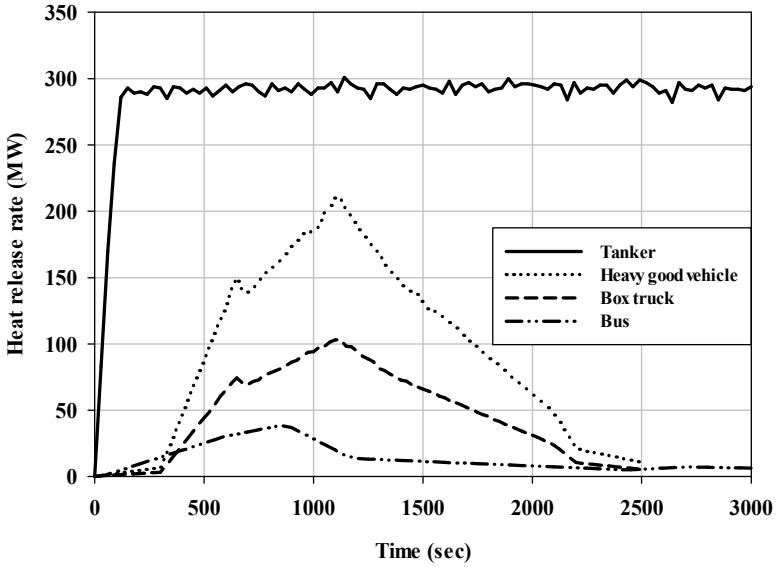

Figure 4-2: Profile of heat release rate for various types of vehicle fires.

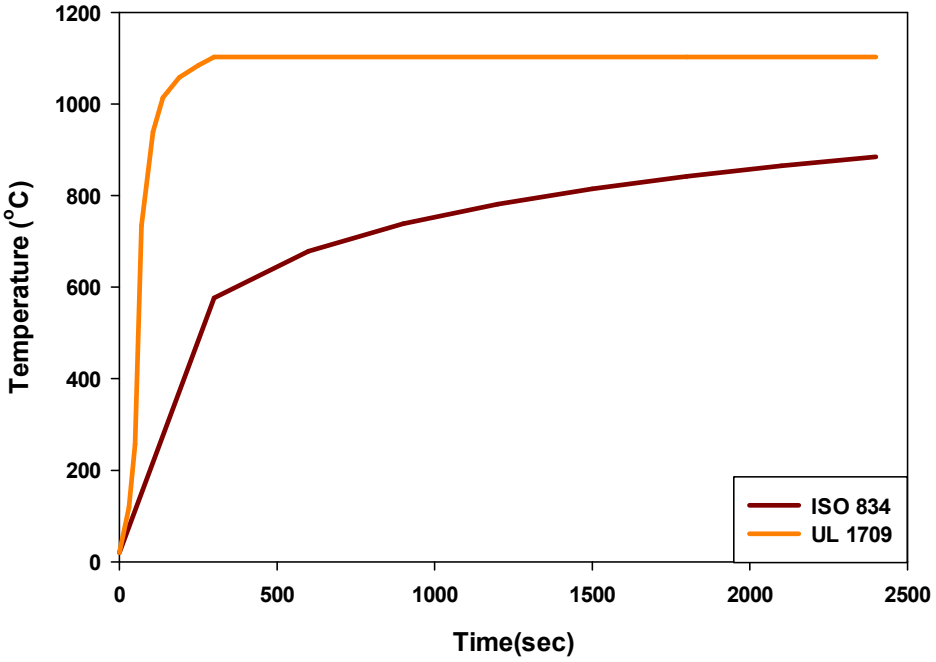

Figure 4-3: Time-temperature curve for standard fire exposures.

4.3 Modeling Approach

Modeling was performed by sequentially coupling models to predict the thermal and structural behavior of the bridge. Two different types of modeling methodologies were used to evaluate the exposure onto the bridge structural elements: one to model the non-uniform exposure due to a vehicle fire and another to evaluate the response due to a standard furnace exposure. The vehicle fire scenarios required coupling FDS with Abaqus while the furnace exposure scenarios were all done within Abaqus.

4.3.1 Vehicle Fire Exposure

4.3.1.1 Coupled Fire-Thermal-Structural Model

The bridge response prediction in this work was conducted through a series of three sequentially coupled analyses: fire analysis, thermal analysis, and structural analysis. A sequentially coupled fire-thermal-structural model was used in part to accommodate the use of different mesh sizes required for each model. Figure 4-4 shows the flowchart of the sequentially

coupled vehicle fire modeling methodology. Predictions of the fire environment was performed using FDS, Version 6 [30] developed by NIST. The heat transfer from the fire environment onto the bridge structural members determined using FDS was imported into Abaqus through a custom developed user-subroutine within DSFLUX. The three-dimensional heat transfer analysis was then performed using the commercial finite element code Abaqus 6.12 [31]. The predicted temperature rise was then imported into an Abaqus structural model to determine the response of the bridge at high temperatures. The structural model used non-linear, high temperature mechanical properties of the bridge materials, including creep. External loads (gravity and dead load) were held constant during the analysis.

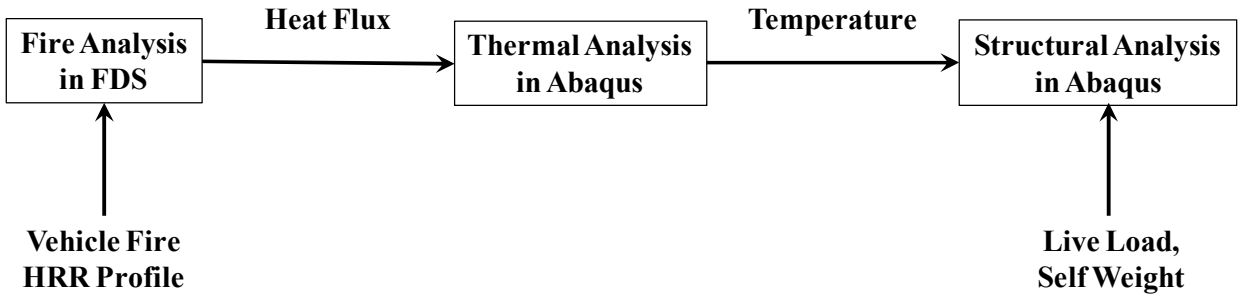

Figure 4-4: A flow chart for modeling the bridge response due to a vehicle fire.

4.3.1.2 Fire Model

Fire simulations were conducted using FDS, Version 6.0 [30]. FDS is a computational fluid dynamics (CFD) model that uses large-eddy simulation to predict the buoyancy driven flows, thermal conditions and species concentrations that develop due to fire. FDS includes predictions of conditions in the gas phase as well as the condensed phase (i.e., solid boundaries). In the gas phase, FDS predicts the fire plume location, heat release rate of the fire, gas species concentrations, soot and visibility through smoke. Radiative heat transfer problems have been solved using the radiation transport equation for a gray gas. A technique similar to Finite Volume Method (FVM) has been used to solve this equation, while the absorption coefficients have been calculated using RADCAL narrow band model. FDS uses the fire conditions to predict heat fluxes to the boundaries. The mesh is rectilinear in shape, and obstructions in the flow field must conform to that of the rectilinear grid to accurately predict heat transfer to these surfaces. In this

study, FDS simulations were performed on a standard x86-Linux cluster with a dual-socket quad-core 2.26 GHz Intel Nehalem processor and 24GB of memory.

The FDS model of the bridge is shown in Figure 4-5. The model included the sloped ground under the bridge approach and departure lane, the road underneath the bridge, and the bridge to ensure proper flow within and around the bridge. In the FDS model of the bridge, the girders were modeled as the web only (excluding the lower flanges, upper flanges and girder stiffeners). Simulations were performed to demonstrate that the exclusion of the flanges does not significantly affect the flow field as well as the heat flux exposure onto the web and concrete deck for the fires considered. Heat fluxes to the solid obstruction (steel web and concrete deck) were extracted from the simulations using a boundary file for export to Abaqus. The domain was extended by 26.0 m, 9.0 m and 13.0 m along width, depth and height respectively to allow the free flow of gases into and out of the domain as well as ensuring that the entire flame was included in the domain. Computational domain sizes for the different fires are provided in Table 4-3.

The time varying heat release rate of the fire was modeled as the ejection of gaseous fuel from the top surface of the vehicle by prescribing the heat release rate per unit area with time. The profiles of heat release rate from different burning vehicles are shown in Figure 4-2. The fire footprint, provided in Table 4-1, was based on the size of the vehicle in the fire test [5, 7, 10]. The fuel inlet temperature was set equal to the fuel boiling point. All FDS simulations were performed using the default turbulence model proposed by Deardorff. Large scale fires result in a significant amount of soot production in the flaming region that blocks radiation from escaping from the fire [18]. Soot blockage increases with fire diameter and results in higher gas temperatures as the fire diameter increases [32]. The level of soot blockage on fire exposure is modeled in FDS using a radiative fraction model approach. Due to using the radiative fraction modeling approach, the soot and CO yield was set to 0.0 kg/kg. The elevated temperature thermo-physical properties for concrete and steel from the Eurocode [33, 34] were used in the FDS modeling. Though the temperature rise of the elements in FDS was not used as the thermal analysis, predicting the temperature rise of these surfaces was used to predict reradiation between surfaces, which is necessary to obtain accurate heat fluxes.

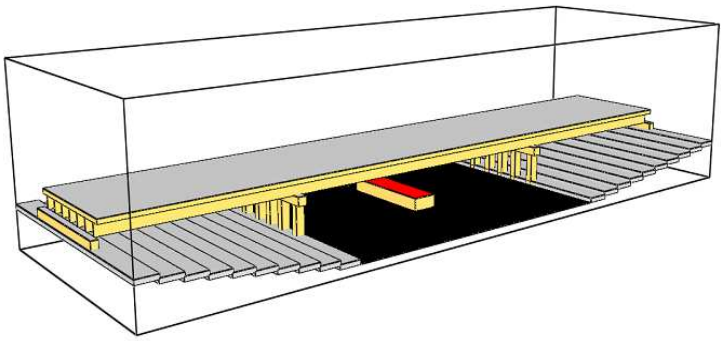

(a) View from fire side

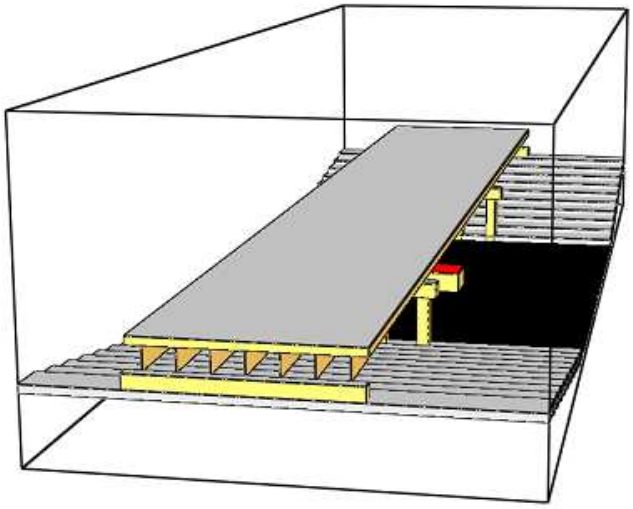

(b) View from approach side

4-5: The FDS fire model of the bridge with a vehicle fire beneath.

FDS simulations results depend on the cell size chosen for the simulation, similar to other CFD models. Floyd *et al*. [27] recommended that the ratio of characteristic fire diameter and cell size, $D^*/\delta x$, should be used for the prediction of the optimal grid size, where δx is the computational cell size and D^* is defined as

$$D^* = \left(\frac{\dot{Q}}{\rho_\infty c_p T_\infty \sqrt{g}}\right)^{2/5} \tag{3}$$

In this study, it was found that there should be 7 to 10 cells across the fire diameter to get the converged results. The dimensions of the computational domain and fire exposure for all the simulations conducted are provided in Table 4-3.

Table 4-2: Thermo-physical properties of the steel girder, concrete deck and furnace wall materials.

Temperature (K)	Concrete			Steel		Ceramic Fiber	
	k (W/m-K)	c_p (J/kg-K)	ρ (kg/m^3)	k (W/m-K)	c_p (J/kg-K)	k (W/m-K)	c_p (J/kg-K)
293	1.95	900	2400	53.34	441.15	3.7e-2	
373	1.76	900	2400	50.67	521.42	3.83e-2	819.18
453	1.59	980	2363	48.0	631.84	5.23e-2	850.93
533	1.43	930	2330	45.34	779.24	6.88e-2	881.40
613	1.29	970	2301	42.68	970.44	8.80e-2	910.59
693	1.16	1100	2276	40.01	1212.25	1.09e-1	938.51
773	1.04	1100	2259	37.35	1511.5	1.34e-1	965.14
853	0.94	1100	2242	34.69	1875.0	1.61e-1	990.49
933	0.85	1100	2225	32.02	832.69	1.90e-1	1014.60
1013	0.77	1100	2209	29.36	2525	2.22e-1	1037.4
1093	0.71	1100	2192	27.3	745.22	2.57e-1	1058.9
1173	0.66	1100	2175	27.3	435	2.94e-1	1079.1
1253	0.63	1100	2158	27.3	650	3.33e-1	1098.1
1333	0.61	1100	2141	27.3	650	3.75e-1	1115.7
1413	0.60	1100	2125	27.3	650	4.20e-1	1132.1
1493	0.60	1100	2108	27.3	650	4.67e-1	1147.2

Table 4-3: Fire description and mesh details for the FDS simulations.

Vehicle Type	Fuel Type	Computational Domain (m)			Fire Dimension (m)			Cell size (m)	Number of cells
		Width	Depth	Height	Width	Depth	Height		
Bus	Gasoline	86.0	30.0	21.0	3.0	12.0	1.5	0.25	433,440
Box truck	Gasoline	88.0	30.0	26.0	3.0	10.5	1.0	0.50	549,120
Heavy goods vehicle	Gasoline	88.0	30.0	26.0	3.0	10.5	1.0	0.50	549,120
Tanker	Gasoline	86.0	30.0	21.0	6.5	14.0	0.5	0.50	549,120

4.3.1.3 Thermal Model

The three dimensional heat transfer analysis simulations were conducted on a single girder using Abaqus 6.12 [31]. In this study, the middle steel girder (Girder-4) and the corresponding concrete slab as seen in Figure 4-6 were selected to evaluate the fire response of the steel bridge elements as it was exposed to the highest heat fluxes in comparison to the other girders. The thermal analysis accounts for the radiation and convection from the fire onto the bridge; radiation from the ground and road onto the bridge; re-radiation from the bridge back onto itself and re-radiation from the bridge to the surroundings. In order to include this, a user-subroutine was used to import the heat fluxes predicted using FDS into Abaqus. The appropriate interactions for convection and radiation were included in Abaqus to implement this heat flux boundary condition. For this, a heat transfer coefficient of 25 W/m^2-K [28] was used along with steel and concrete emissivity of 0.95 and 0.9, respectively [35]. The user-subroutine uses linear interpolation to account for the different meshing between the FDS and Abaqus models as well as structural details not included in the fire analysis. Specifically, the routine assigns heat fluxes to the flanges and web stiffeners based on interpolation from the predicted heat fluxes to the web.

The thermal analysis of the steel and concrete was carried out using Abaqus element DC3D20. This is a three dimensional 20-noded quadratic heat transfer brick element. The thermal model has 7751 nodes and 2096 solid elements. Figure 4-7 contains the finite element mesh adapted for the thermal analysis. A convergence study was performed to choose the appropriate size mesh. In the model, thermal resistance between contact surfaces was not considered and the surfaces in thermal contact were forced to have the same temperature using TIE constraints. The thermal analysis on the steel-concrete composite girder was conducted using temperature dependent thermal properties for steel and concrete. The properties used in the analysis are given in Table 4-2 and were taken from Eurocode 3 [34] for steel and Eurocode 2 [33] for concrete.

4.3.1.4 Structural Model

The structural analysis simulations of the steel girder-concrete deck were conducted using Abaqus 6.12. In the simulation, three dimensional solid continuum 20-noded quadratic elements (C3D20R) were used for the steel girder while 8-noded linear elements C3D8R were

used for the concrete deck. Both C3D20R and C3D8R have three degrees of freedom per node namely three translations in the x-, y- and z- directions. These elements were used to model three dimensional solids and are able to capture deformation of the flange, cracking of concrete in tension. As a result, the elements are well suited for large deformation, large strain and non-linear problems. Woodworth [47] found that solid elements performed well at very coarse mesh densities reducing the computation time against more common shell elements. The single steel girder-concrete deck composite assembly structural model has 97,659 nodes and 15,837 solid elements. Figure 4-8 contains the finite element mesh used in the structural analysis. A convergence study was performed to choose the appropriate mesh size. The total numbers of elements used in the structural analysis are higher than the total number of elements used in the thermal analysis as the convergence study revealed that more elements are required to accurately predict the stress and deformation of the structure. The simulation was performed using the non-linear setting with a time step not exceeding 10 seconds. In the model, the shear studs were not included and the surfaces in composite action were forced to have the same degree of freedom using the TIE constraint.

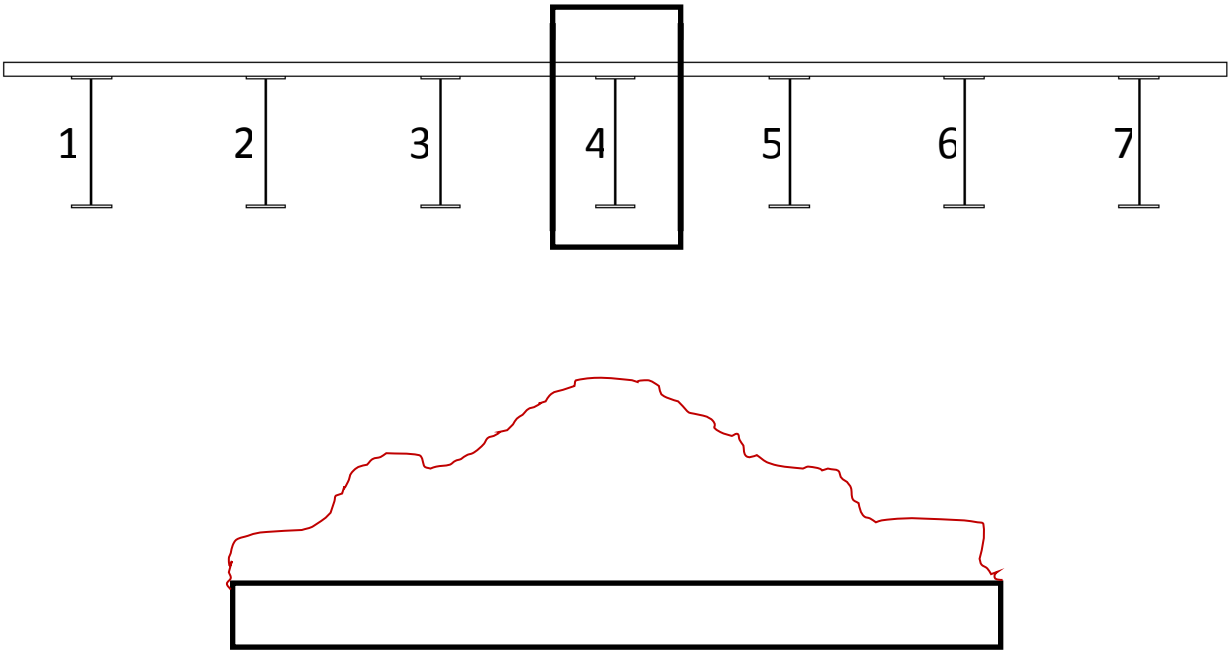

Figure 4-6: Cross section of the simulated highway bridge showing the layout of steel girder 4.

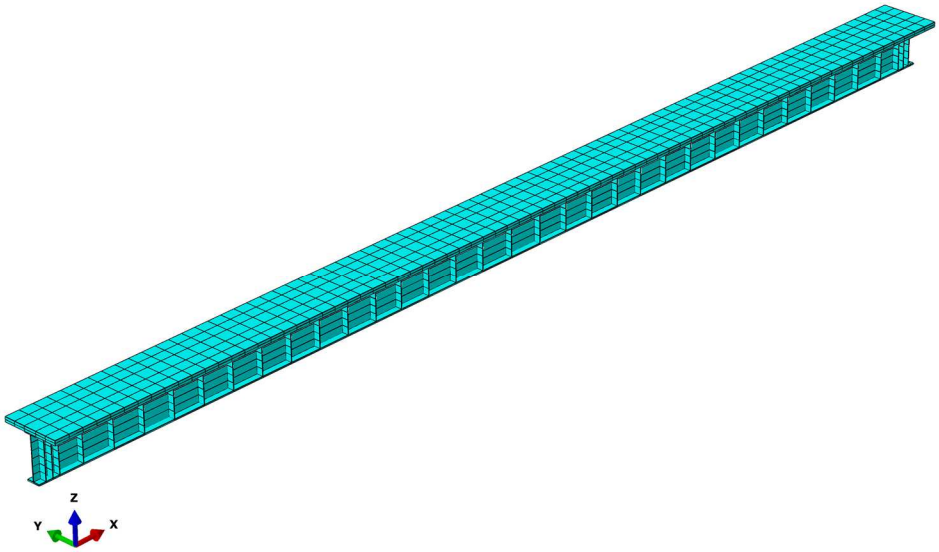

Figure 4-7: Three dimensional finite element mesh of the center steel girder-concrete deck composite assembly for thermal analysis.

The mechanical properties (stress-strain relationships, modulus of elasticity and thermal expansion) were taken from Eurocode 3 [34] for steel and Eurocode 2 [33] for concrete. Figure 4-9 contains the stress-strain behavior with elevated temperature for steel. For input into Abaqus, true stresses (σ_n) and strains (ε_n) were computed from the engineering values of stresses (σ) and strains (ε) using

$$\sigma_n = \sigma(1+\varepsilon) \tag{4}$$

$$\varepsilon_n = ln(1+\varepsilon) \tag{5}$$

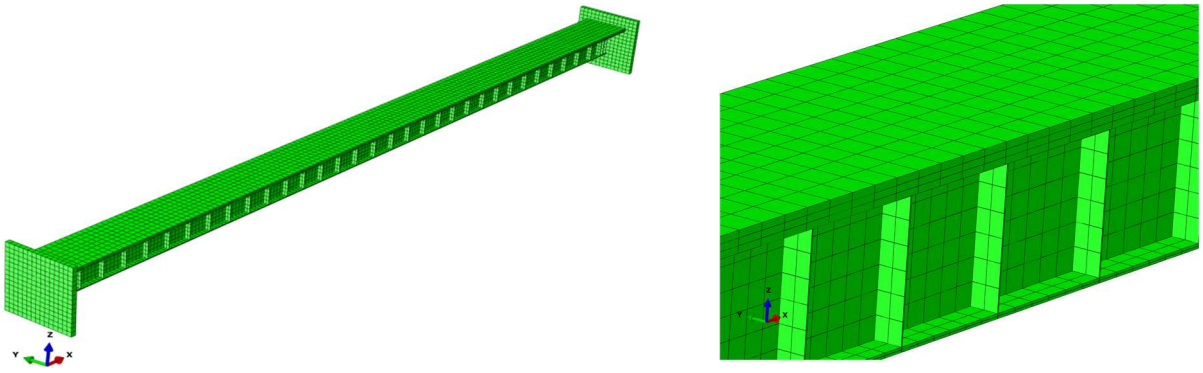

(a) (b)

Figure 4-8: Three dimensional finite element model of the center steel girder-concrete deck composite assembly for structural analysis showing an a) isometric view and b) close-up view.

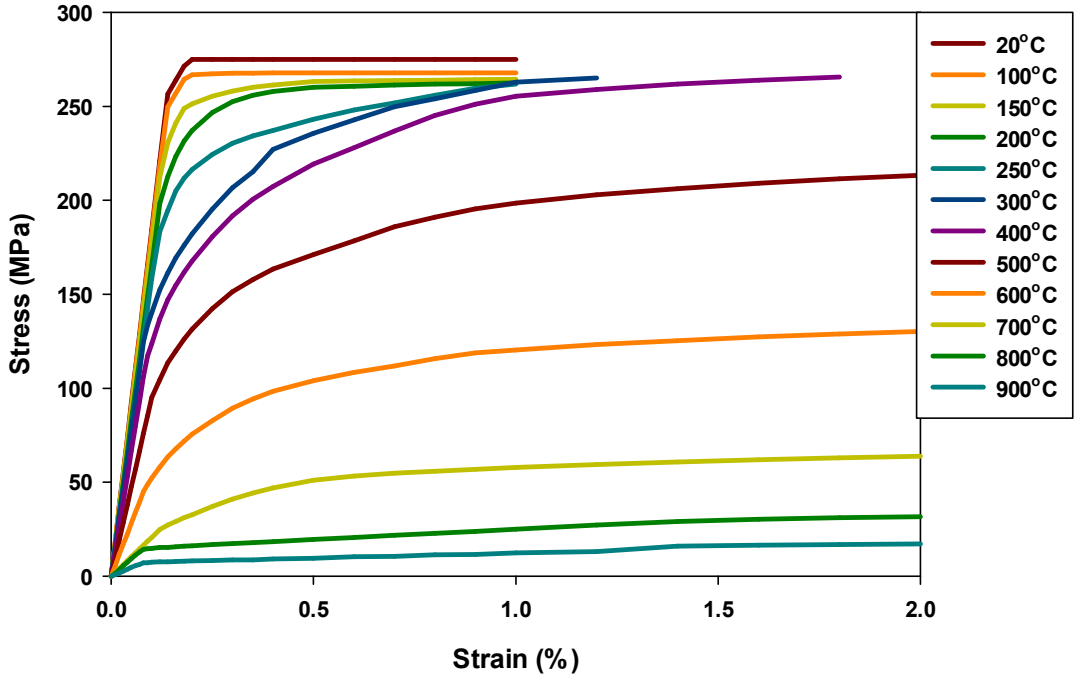

Figure 4-9: Stress-strain relationship for Grade 43A steel as a function of temperature.

To investigate the effect of creep on structural response, the modified version of the Fields and Fields [44] power law creep model was implemented into Abaqus. The power law creep model proposed by Fields and Fields is valid up to a temperature of 650°C. Due to this, it was modified to obtain realistic results both at high and low temperatures [45].

The vertical loads on the structure during the fire included the steel girder and concrete deck self-weight as well as the dead load which consisted of the weight of the curbing and rail assemblies according to AASHTO [36]. The self-weight was applied as a gravitational body force. The dead load consisted of the weight of the wearing surface and concrete parapets were estimated to be 11.25 kN/m. The majority of the simulations were conducted with no live load as found from the literature survey [20, 37]; however , the effects of live loading was assessed for specific cases. For the live load, 4.65 kN/m representing 30% of the live loading according to AASHTO [36] provisions was applied.

The cross bracings were not explicitly modeled, but the effect of cross bracing members was accounted for in the model by restraining the movement of web plate in the transverse

direction. In a similar way, the transverse movement of the concrete slab was restrained to model the effect of restraint due to adjacent spans. To reduce the size of the structural model, the approach and departure span was not included in the structural model. Their effect was accounted for by creating two rigid blocks offset from the bridge at a distance equal to the expansion joint gap (0.072m) from the outer edge of the girder and deck assembly. The interaction between the steel girder-concrete deck assembly and the rigid blocks were modeled using the Abaqus mechanical contact property option with the normal surface to surface interaction. Due to this, the support ends of the girder were considered as a roller to allow free axial movement until the girder contacted the rigid blocks. The support end boundary conditions were applied on multiline nodes to reduce the stress concentration.

The structural analysis was completed in two steps. The self-weight and dead loads were applied to the model initially and then the nodal temperature histories generated from the heat transfer analysis were imported. The solution method utilized adaptive damping to aid convergence. Adaptive damping adds a small mass proportional force to aid in numerical convergence when local instabilities are present [38]. The magnitude of the mass was adjusted and tested to ensure that the damping does not affect the global behavior. In this study, a value of 0.0001 was used as the dissipated energy fraction in Abaqus.

4.3.2 Standard Fire Exposure

A sequentially coupled, three dimensional thermal and structural analysis was also conducted to predict the thermo-structural response of a steel girder-concrete deck composite assembly subjected to a standardized furnace exposure. The thermal analysis simulates the radiation exchange inside the furnace, convection between the furnaces gases and assembly, and the heat conduction to predict the element temperature rises. The temperature results were imported into a structural response model that was used to predict the response of the composite assembly at high temperatures.

4.3.2.1 Thermal Model

Three-dimensional thermal analysis simulations were conducted with Abaqus 6.12 using the furnace exposure methodology proposed by Nahid *et al.* [39]. For this, a rectangular furnace enclosure was constructed around the bridge assembly test specimen as shown in Figure 4-10.

The five furnace walls were insulated surfaces with an assigned interior surface temperature that followed the desired time-temperature fire exposure curve. A three-dimensional thermal analysis was performed on the test specimen located on top of the furnace enclosure to predict the temperature rise. The temperature rise of the test specimen was conducted using quadratic solid elements (DC3D20). In the model, thermal resistance between contact surfaces was not considered and the surfaces in thermal contact were forced to have the same temperature using TIE constraints. Analysis was performed using the nonlinear setting with a time step not exceeding 10 s.

The test specimen boundary conditions on the exposed side included convection with furnace gases, radiation exchange between surfaces on the inside of the furnace including itself, and reradiation. The convection with the furnace gases was implemented using a convection heat transfer coefficient of 25 W/m^2-K and 50 W/m^2-K for the ISO-834 and UL-1709 fire exposure, respectively, as recommended in Eurocode 1 [28]. The gas temperature was equal to the time-temperature fire exposure curve. Radiation exchange between surfaces inside the furnace was performed using the Abaqus built-in radiation exchange model. For this, the furnace walls were divided into 150 mm size square elements while the test specimen was divided into element sizes appropriate to capture the temperature variation of the specimen and converged results. A furnace wall element size sensitivity study confirmed the selected wall element size produced converged results. The view factor between an element inside the furnace and all other elements was calculated at the beginning of the simulation. Using these view factors and the instantaneous surface temperatures of elements inside the furnace, the radiation exchange inside the furnace was calculated at each time step. This approach assumes that the attenuation through the furnace gases is negligible, which was previously discussed to be appropriate for furnaces with clean burning furnace burners.

The unexposed side of the test specimen included boundary conditions for convection and radiation exchange with the laboratory surroundings. The convection boundary condition used a laboratory gas temperature of 298K and a convective heat transfer coefficient of 10 W/m^2-K [28]. The radiation exchange was determined using the element surface temperature on the unexposed side and a laboratory gas temperature of 298K.

The thermal analysis on the test specimen was conducted using temperature dependent thermal properties for steel, concrete, and ceramic fiber insulation. The properties used in the

analysis given in Table 4-2 were taken from Eurocode 3 [34] for steel, Eurocode 2 [33] for concrete, and from the manufacturer for the ceramic fiber insulation [25]. The value of emissivity for concrete, steel, ceramic fiber, and furnace walls were 0.94, 0.9, 0.9 and 0.75; respectively [35].

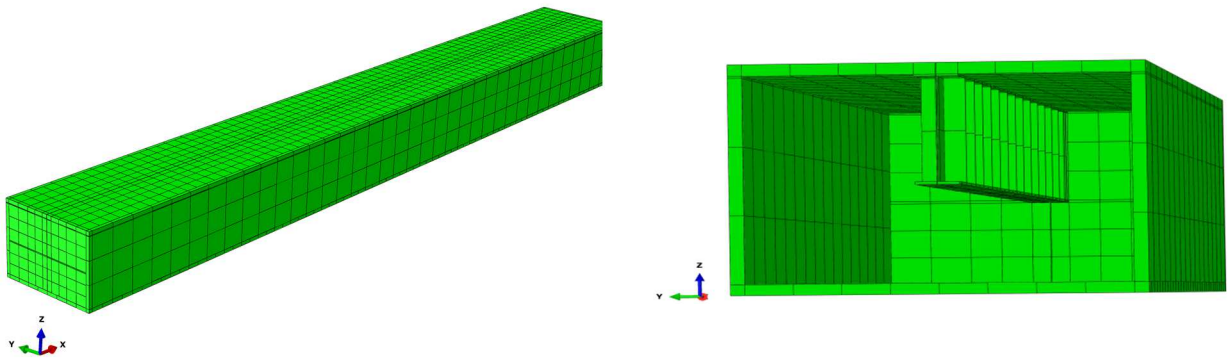

(a) Exterior view (b) Interior view

Figure 4-10: Three dimensional finite element thermal model of the steel girder-concrete deck composite assembly for the standard fire exposure analysis.

4.3.2.2 Structural Model

Three dimensional non-linear structural analyses were conducted using Abaqus 6.12 on the same structural model described in Section 3.2.1. The loading and boundary conditions were also the same as that described in Section 3.2.1.

4.3.3 Simulations

Table 4-4 presents the series of simulations performed in this study to investigate the structural integrity of a steel girder-concrete deck composite assembly during a fire exposure. Initial simulations were performed to evaluate the behavior of a steel girder-concrete deck composite assembly under different vehicle fire scenarios to determine what size fire is required to cause the assembly to fail and how this compares with behavior during a standard furnace exposure. The effects of structural boundary conditions and loading were considered to determine the impact of these parameters on the structural integrity. The effect of creep on the thermo-structural response was also investigated.

4.3.4 Failure criteria

The steel girder concrete deck composite assembly was considered to fail when one of the following criteria were met:

i. The vertical mid-span deflection exceeded $L/20$, where L is the span length.
ii. The rate of vertical deflection exceeded $L^2/9000d$.
where, d is the distance from the top of the structural section to the bottom of the design tension surface.
iii. The ultimate strain (ε_{ut} = 20.0% for steel)[34] of the material was exceeded. It was determined by comparing the maximum principal strain of the structure with the ultimate strain of the material.
iv. The von Mises stresses of the element exceeded the material ultimate strength.

Table 4-4: Details for the simulations to evaluate the behavior of the steel girder-concrete deck composite assembly during fires.

Parameter studied	**Case**	**Fire Scenario**	**Exposure Duration (sec)**	**Creep Model**	**Boundary Condition**	**Loads**
Fire Scenario	1	Bus	2400	No creep	PR, δ=0.072m	G
	2	Box truck	2400	No creep	PR, δ=0.072m	G
	3	Heavy goods vehicle	2400	No creep	PR, δ=0.072m	G
	4	Tanker	2400	No creep	PR, δ=0.072m	G
	5	ISO-834	2400	No creep	PR, δ=0.072m	G
	6	UL-1709	2400	No creep	PR, δ=0.072m	G
Boundary Condition	7	Heavy goods vehicle	2400	No creep	Simply Supported	G
	8	Heavy goods vehicle	2400	No creep	PR, δ=0.036m	G
	9	Heavy goods vehicle	2400	No creep	PR, δ=0.072m	G
	10	Heavy goods vehicle	2400	No creep	Fixed	G
Loading Condition	11	Heavy goods vehicle	2400	No creep	PR, δ=0.072m	G
	12	Heavy goods vehicle	2400	No creep	PR, δ=0.072m	G+0.3Q
Effect of Creep	13	Tanker	2400	No creep	PR, δ=0.072m	G
	14	Tanker	2400	creep	PR, δ=0.072m	G

PR: Partially restrained, δ: Expansion gap, G: Gravity and dead weight, Q: Live load

4.4 Model Validation

There is a lack of fire test data on the response of steel bridge girders as well as thermo-structural response of beams exposed to a localized fire. As a result, the model was benchmarked against two data sets. The fire prediction and thermal analysis parts of the model were validated with heat flux and temperature rise measurements of a steel I-beam mounted to a ceiling directly above a heptane pool fire. To validate the thermal and structural analyses as well as the furnace modeling, model results were compared with data on the response of a steel beam-concrete slab assembly in a furnace environment.

4.4.1 Pool Fire Exposure onto Steel I-Beam

Experiments were conducted on an unprotected steel I-beam mounted to a ceiling directly above a heptane pool fire to measure the effects of fire heat release rate on the thermal exposure and temperature rise of the steel beam [39, 40]. For validation of the fire and thermal model, simulation results were compared with measured the heat fluxes and temperature rise of the steel beam for one experiment.

Myllymaki and Kokkala [39] measured the total heat flux onto the steel beam surfaces as well as the temperature rise of the steel I-beam mounted below a lightweight concrete Siporex slab directly above a heptane pool fire with fire heat release rates sizes ranging from 0.56-3.6 MW. For comparison with the model, simulations were conducted on the 3.6 MW fire with a distance of 1.77 m between the lower flange and pool surface. The steel I-beam was 0.57 m high and 4.5 m long with web, lower and upper flange thicknesses of 6 mm, 8 mm and 18 mm; respectively. In the fire simulation to be consistent with the bridge fire study, the lower and upper flanges of the steel I-beam were not included. From the fire simulation in FDS, it was observed (not shown here) that the width of the flame was much larger compared to the width of the lower flange and the movement of the flame and heat transferred to the surfaces were not affected due to the presence of the lower flange. The fire was produced by placing commercial liquid heptane LIAV 110 in a pool contained in a 1.77 m diameter pan.

The predicted and measured [39] heat fluxes to the web surfaces of the steel I-beam due to the pool fire directly beneath the beam are provided in Figure 4-11. The predicted heat flux to the web agrees within 10% of the data. The deviation is attributed to calculating the heat flux

with a plate thermometer. As the fire behavior is transient, the measurement of heat flux based on a relatively large area for the case of plate thermometer is expected to be low.

Predicted heat flux from the fire analysis was imported into Abaqus through a user subroutine, DSFLUX and the thermal analysis was conducted to predict the temperature rise of steel I-beam elements. Predicted and measured temperature rise of the web of steel I-beam are provided in Figure 4-12. Overall, predictions from the sequentially coupled FDS and Abaqus model match within 25% with the reported test data. The slight variation in the temperature response at a distance far from the centerline was attributed to the variations in the properties of steel and the transient behavior of the burning of fuel.

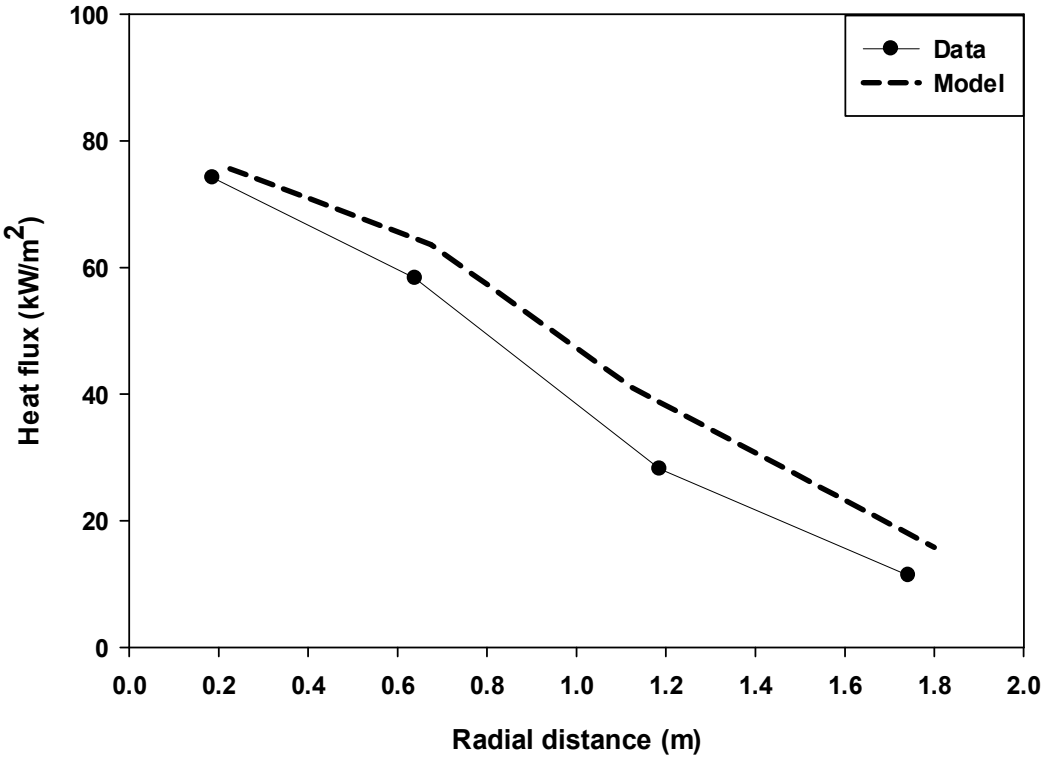

Figure 4-11: Comparison of heat flux between experimental result [39] and FDS prediction.

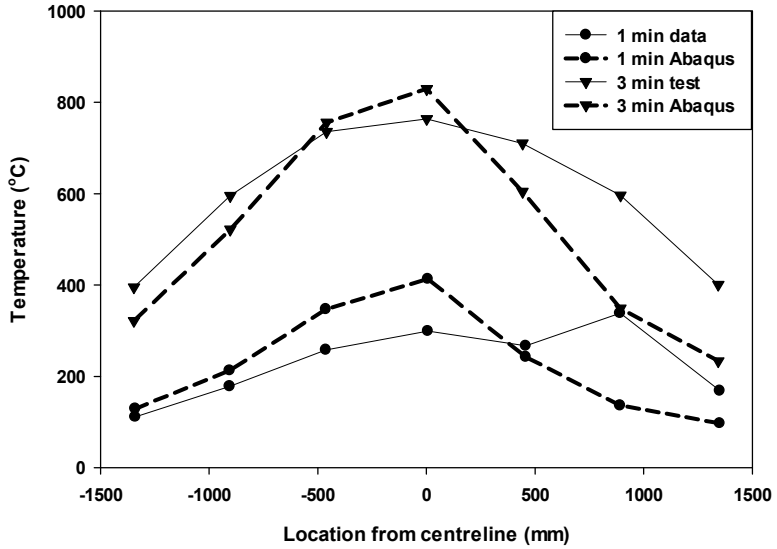

Figure 4-12: Prediction of web temperature rise of steel I-beam in comparison with the test data [39].

4.4.2 Furnace Exposure on a Concrete-Steel I-beam Floor Assembly

Wainmann and Kirby [14] conducted a series of experiments on an unprotected concrete slab floor with a single steel I-beam support on the fire exposure side of the concrete. Simulations were conducted on a composite concrete-steel I-beam floor assembly with simply supported end conditions. The steel I-beam was a 254x146 section with flange and web thicknesses of 12.7 mm and 7.3 mm; respectively. The concrete slab was 125 mm thick and covered the top of the furnace. The furnace exposure was performed in accordance with the ISO 834 time-temperature history with furnace control conducted using standard furnace thermocouples. Elevated temperature material properties were used in the modeling, but creep was not included in the structural response predictions.

A simulation was performed to predict the temperature rise and mid-span vertical deflection history of concrete-steel I-beam assembly exposed to a furnace environment. Figure 4-13 contains the thermal response predictions for the steel I-beam mounted below the concrete slab. As seen in Figure 4-13, the temperature response was within 10% of the data for all parts of the beam for the exposure duration. Mid-span vertical deflection of the concrete-steel I beam

assembly are provided in Figure 4-14. As seen in Figure 4-14, the mid-span deflection response was within 10% for the duration of the exposure.

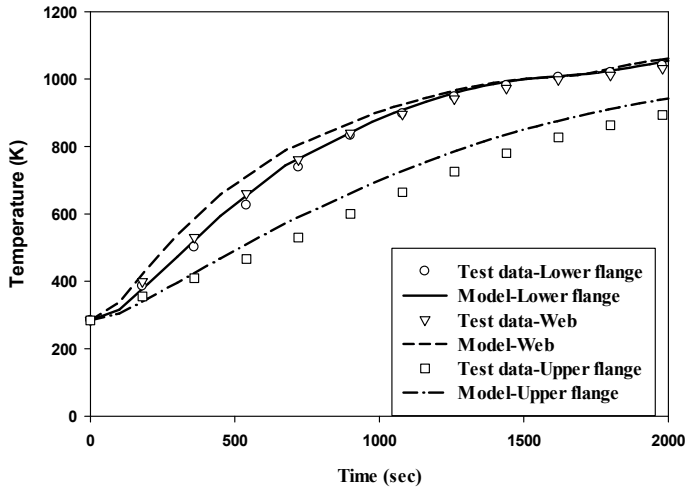

Figure 4-13: Prediction of thermal response of 254x146 steel I-beam mounted below the concrete slab subjected to an ISO 834 furnace exposure in comparison with test data [14].

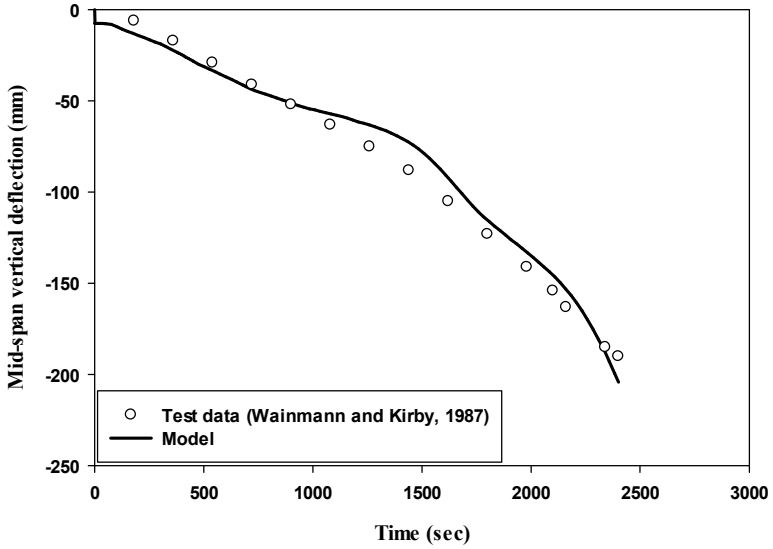

Figure 4-14: Prediction of mid-span vertical deflection of steel I-beam concrete floor assembly subjected to an ISO 834 furnace exposure compared with the test data [14].

4.5 Results

Simulation results on bridge structural elements are provided in the following sections and the fire response of bridge structural elements are compared between different fire scenarios. This was performed to identify the fire scenarios that could result in a collapse of a bridge structure and require further study. Vehicle fires will typically result in a thermal gradient both along the length and depth of the bridge structural elements. Due to this, the behavior of bridge structural elements are also compared between vehicle and standard fire exposure to evaluate the effect of longitudinal temperature variation. Details of the simulations are provided in Table 4-4. In these simulations, the fire exposure was performed on the entire bridge. Due to the computational expense of these simulations, the effect of the fire exposure on the thermo-structural response was performed by evaluating the response of only the center girder of the bridge with a portion of the concrete deck.

4.5.1 Influence of Fire Exposure

4.5.1.1 Fire Dynamics

The influence of different vehicle fire scenarios on the flame dynamics occurring beneath the bridge are provided in Figure 4-15. These are plots of the heat release rate per unit volume (HRRPUV) at a threshold where the flame will be supported (set to 46 kW/m^3 in this study). As a result, the HRRPUV plot shows the outside envelope of where the fuel burning is occurring and provides a means for visualizing of the flame. Through validation studies on free burning plumes and ceiling jets, it was found that the sum of the cell volumes with a HRRPUV value of greater than 46 kW/m^3 represents the total volume where 95% of prescribed heat release rate was produced.

As seen in Figure 4-15, the bus fire exposure resulted in a fire scenario where the flame impinges on the concrete deck but there is no axial extension of the flame along the length of the bridge. In contrast, the box truck, heavy goods vehicle and tanker fire exposures resulted in fire scenarios where the flames extend toward the ends of the bridge along the space between the girders. The extension of flame along the length of the bridge depends on the heat release rate of the burning vehicle. The difference in flame dynamics will cause the steel girder elements to be exposed to different heat flux levels along their length.

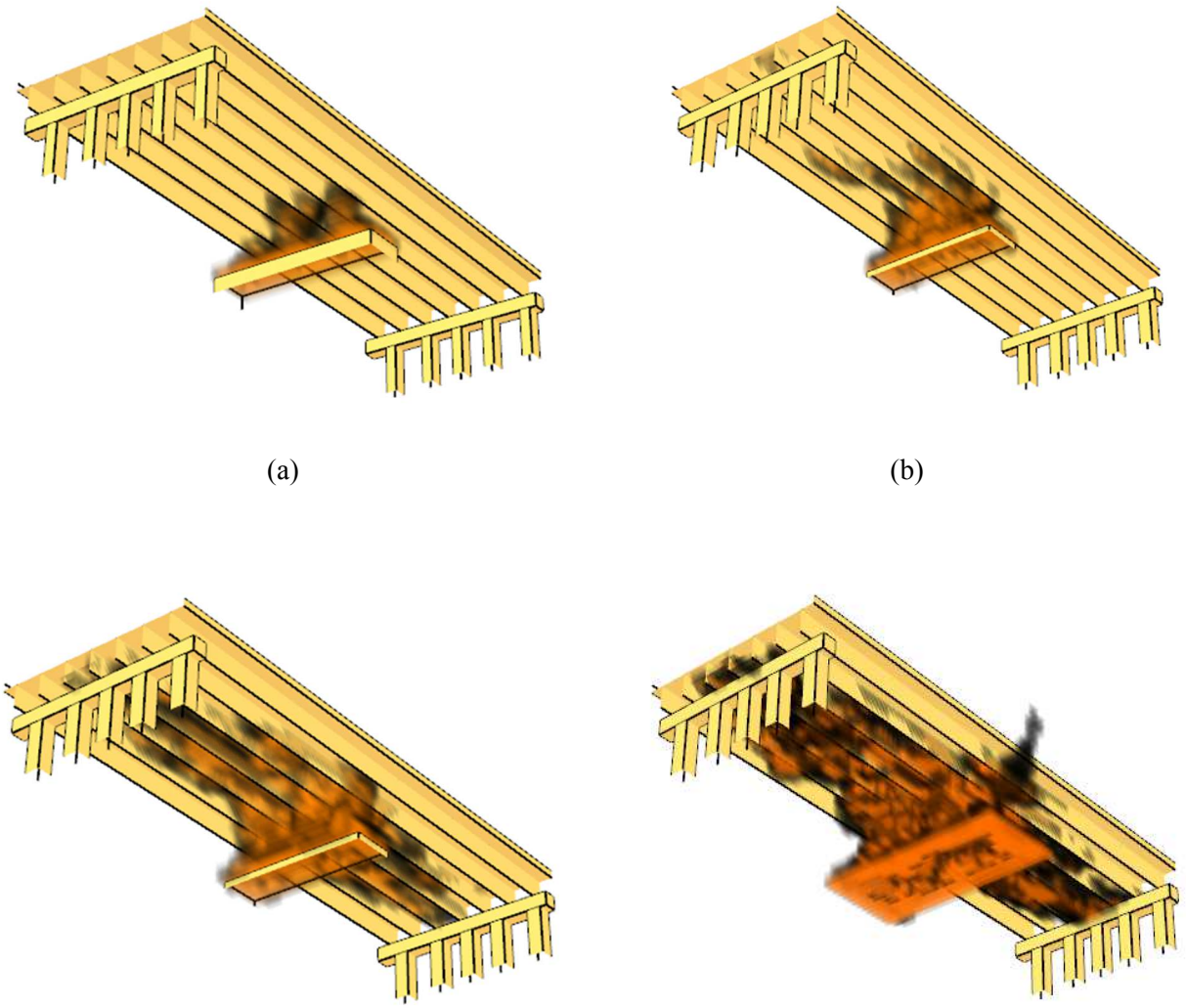

(a) (b)

(c) (d)

Figure 4-15: Flame dynamics of a a) bus, b) box truck, c) heavy goods vehicle and d) tanker fire exposure beneath a highway bridge.

Figure 4-16 contains predicted maximum heat fluxes on the web surfaces at mid-span from different vehicle fire scenarios as well as the heat flux from standard fire exposures. For the standard furnace fire exposure, the standard heat flux calculated from the gas temperature was reported in Figure 4-16. As seen in Figure 4-16, the UL 1709 fire exposure resulted in the highest heat flux among the six different fire exposures considered in this study. In contrary, the

heavy goods vehicle and tanker fire exposure resulted in higher heat fluxes than ISO 834 fire exposure whereas the box truck and bus fire resulted in lower heat fluxes than ISO 834.

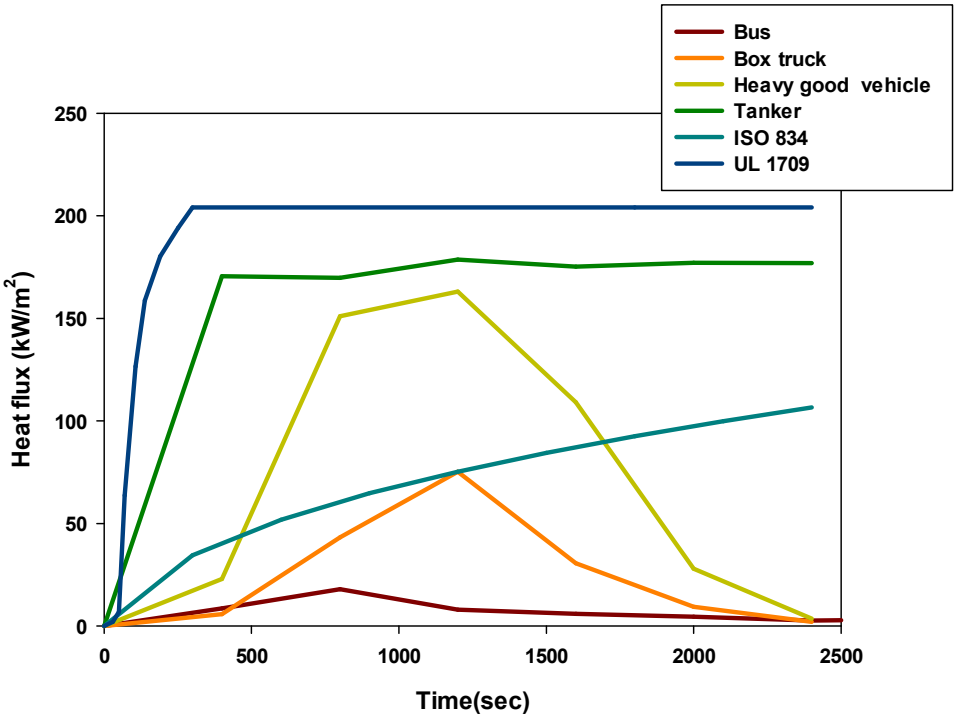

Figure 4-16: Prediction of maximum heat flux on the web surfaces of steel girder for vehicle and standard furnace exposure.

4.5.1.2 Bridge Structural Element Response during Fire

Table 4-5 contains the failure time, failure mode and maximum mid-span vertical deflection at the time of failure for the different fire exposures simulated in this study, Cases 1-6 in Table 4-4. Note that only gravity loads due to self-weight and dead loads are included in these analyses. The results indicate that all of the fire exposures except the bus and box truck fire resulted in failure of the single steel girder-concrete deck assembly. The bus and box truck fire exposures do not result in failure of the single steel girder-concrete deck assembly according to the criterion described in Section 3.4 with no live loading and an expansion gap width of 0.072 m. The mid-span vertical deflection only reaches a value of 0.28 and 0.40 m for the bus and box truck fire respectively compared to *L/20* = 1.85 m. In addition, the deflection starts to recover starting at 1350s as the fire starts to diminish.

For all the cases that failed, the instability of the steel girder assembly was initiated with the occurrence of local buckling of the bottom flange. The time, temperature and location of the local buckling of the bottom flange are different for different fire exposures. For the standard ISO 834 and UL 1709 fire exposure, the bottom flange near the boundary undergoes local buckling whereas for the heavy goods vehicle and tanker fire exposure the bottom flange at the impingement location experiences local buckling. The temperature at which the local buckling occurs with the uniform furnace exposures was lower compared with the non-uniform heavy goods vehicle and tanker fire exposures. After the bottom flange undergoes local buckling, the steel girder-concrete deck does not fail immediately and continues to carry the load. The additional thermal expansion due to the continuous element temperature rise was accompanied by the continuous increase of downward deflection. The steel girder assembly finally collapses with the formation of plastic hinge at the mid-span for the heavy goods vehicle and tanker fires. Note the tanker and heavy goods vehicle fire causes the girder assembly to fail at shorter times in comparison to the ISO 834 exposure. This is attributed to the higher local heat fluxes and the attainment of higher temperatures within a relatively short period of time. For the tanker fire exposure, the steel bridge girder assembly fails at approximately 1012 s whereas it is 1157 s and 1180 s for the heavy goods vehicle and ISO-834 uniform furnace fire exposure. The UL 1709 fire exposure causes the single steel girder assembly to fail within a relatively short period of time (350 s).

Table 4-5: Results on the influence of fire exposure study.

Fire Exposure	Failure Initiation		Ultimate Failure		Mid-span Deflection (m)	Thermal Gradient at Ultimate Failure
	Time (sec)	Mode	Time (sec)	Mode		Along length
Bus	N/A	N/A	N/A	N/A	0.28*	
Box Truck	N/A	N/A	N/A	N/A	0.73*	
Heavy Goods Vehicle	1040	LB	1157	PH	0.71	554
Tanker	974	LB	1012	PH	0.85	365
ISO-834	550	LB	1171	U	1.82	N/A
UL-1709	100	LB	350	PH	1.25	N/A

LB: local buckling of lower flange, PH: formation of plastic hinge, U: mid-span deflection exceeded L/20

* values represented the maximum during the whole simulation duration

The variation in temperature and deflection along the length of the beam at failure were also examined to further evaluate the behavior near failure. Figure 4-17 contains a comparison of the steel girder and exposed concrete deck element temperature for the five different fire exposures at the time of failure. For the bus and box truck fire exposure, the temperatures are plotted at simulation duration of 1100s and 1200s respectively when the element reaches the highest temperature during the simulation. As expected, the ISO-834 and UL-1709 furnace fire exposures resulted in a uniform temperature along the entire length of the structural element. On the other hand, vehicle fire exposures resulted in a temperature gradient along the length of 365 - 554^{o}C. This is attributed to the localized heating of the element due to the impingement of the flame onto the steel girder. The maximum element temperature increases with the increase in fire heat release rate, but the temperature gradient remains approximately same for the three vehicle fire exposures considered. In addition, note the tanker fire exposure resulted in a temperature gradient of 60°C along the depth of the steel girder whereas standard fire exposure resulted in a temperature gradient of 130°C. This is in part due to the immersion of bridge elements into flame at the point of impingement in the case of the vehicle fire exposure.

Figure 4-18 contains the mid-span vertical deflection of the girder assembly with time up to the onset of failure or fire duration (2400 s) for the bus and box truck fires. As seen in Figure 4-18, the steel girder assembly initially deflects by 125 mm due to the self-weight and the dead load. Following this, the deflection increases due to the increase in girder assembly temperature and effects of thermal expansion. At the initial stage, the elastic response dominates the deflection behavior up to the yielding point. The elevated temperature of the girder assembly also causes the girder to extend in the axial direction due to the thermal expansion until the girder comes in contact with the rigid block representing the approach span. Depending on the fire exposure, the steel girder comes in contact with the rigid block at different times. Thereafter, the rate of deflection decreases with time. This is due to the thermal gradient along height and the presence of rigid block which restrains thermal expansion causing a local uplifting moment. The steel modulus is reduced due to the high temperature and local member distortions alleviate some of the axial forces, which increase downward deflections. Due to the localized exposure from the fuel tanker and heavy goods vehicle fires, a plastic hinge forms at the mid span resulting in girder assembly collapse. For the uniform standard fire exposures, the girder

assembly is taken to collapse after the deflection was predicted to exceed the L/20 limit but no plastic hinge was observed.

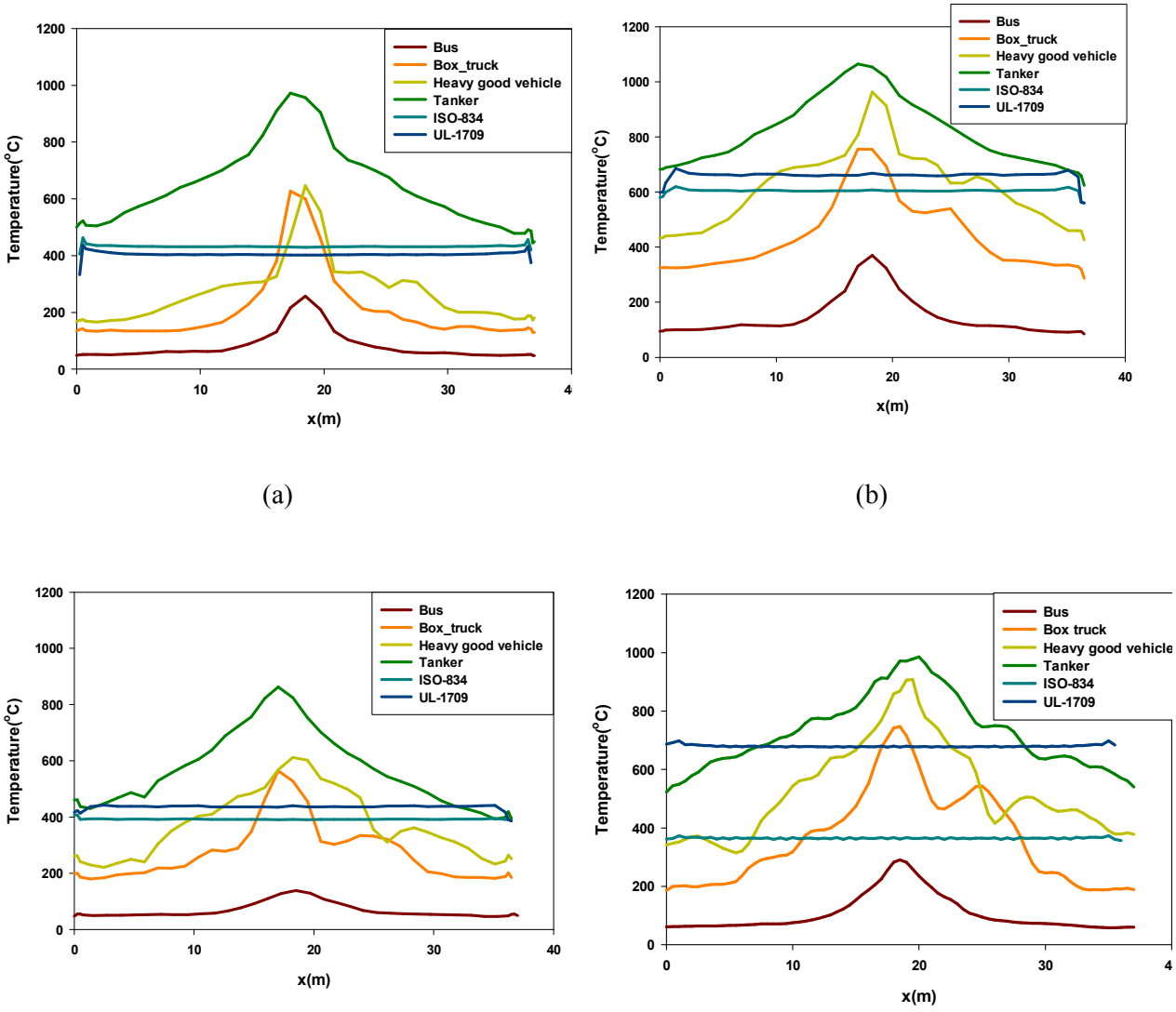

Figure 4-17: The temperature distribution along the bridge length at the a) lower flange, b) mid-height of web, c) upper flange, and d) exposed surface of concrete at the time of failure or maximum temperature reached for the bus and box truck.

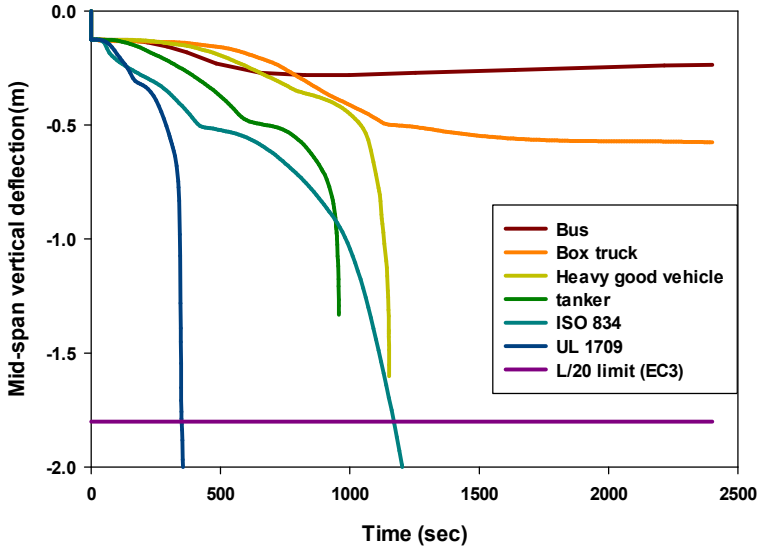

Figure 4-18: Deflection response of steel girder-concrete deck composite assembly as a function of time with different fire exposures.

4.5.2 Effect of End Structural Boundary Conditions

The effect of structural boundary conditions at the ends of the steel girder assembly were investigated by altering the size of the initial expansion gap widths at the ends of the assembly and comparing the results with a simply supported assembly and an assembly with fixed boundary conditions. The heavy goods vehicle fire exposure was selected to evaluate the effect of boundary conditions. Figure 4-19 contains plots of the mid span deflections for gap widths of 0.036 m and 0.072 m as well as simply supported and fixed boundary conditions. For the simply supported case the steel girder initially deflects by 125 m due to the self-weight and the dead load. The rate of downward deflection starts to increase at around 350s as the material temperature increases. The increase in downward deflection is due to the loss of material stiffness at higher temperature and the thermal bowing due to the temperature gradient along the depth. At approximately 1000 s, the steel girder assembly fails with the formation of plastic hinge resulting in a steep increase in the rate of downward deflection. For the fixed case, the steel girder initially deflects 31 mm due to the self-weight and the dead load of the assembly. The smaller deflection is due to the fixed end conditions. The vertical downward deflection of

the steel girder assembly starts to increase at 450s with the increase in girder assembly temperature and eventually fails at around 860s with the formation of a plastic hinge at mid-span. For the partially restrained case, the deflection history of the steel girder assembly follows that of the simply supported case up to the duration of 520s and 800s respectively for gap widths of 0.036m and 0.072m respectively. The rate of increase of vertical deflection decreased for the case with expansion gap width of 0.072m whereas the steel girder assembly experienced an upward deflection in the case with an expansion gap width of 0.036m. This upward deflection response is a balance of moments between the downward moment resulting from the self-weight, dead load and the thermal bowing with the upward moment due to the axial force exerted by the boundary restraint. In addition, note the increase in failure time from 920s to 1200s for the increase in expansion gap width from 0.036m to 0.072m for the heavy goods vehicle fire exposure.

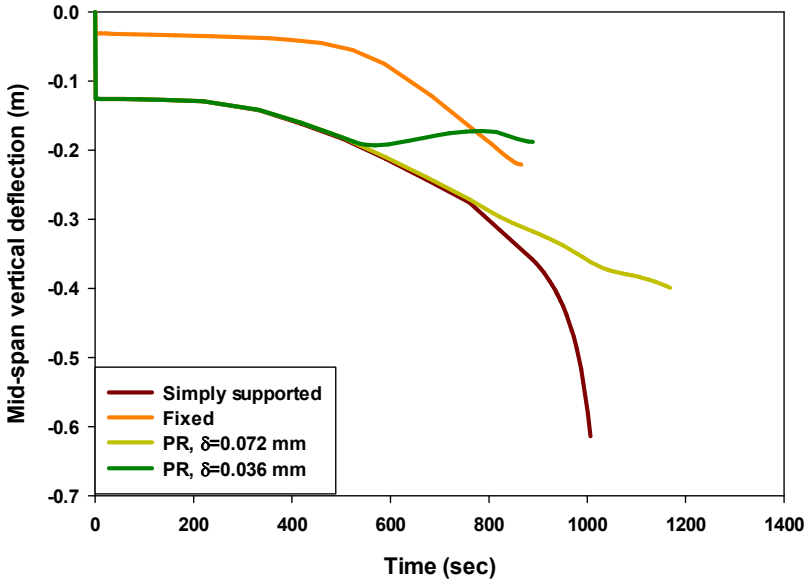

Figure 4-19: Influence of end structural boundary condition on the mid-span deflection over time for a heavy goods vehicle fire exposure.

4.5.3 Effect of Live Loading

The effect of live load on the fire response of a single steel girder-concrete deck assembly was investigated in this study for the heavy goods vehicle fire exposure. The live load was a

uniformly distributed load of 9.3kN/m, which represents 30% of the live load according to AASHTO provisions. A comparison in mid-span deflection with and without load is contained in Figure 4-20. It is seen that the addition of live loading decreases the failure time by 17% for the heavy goods vehicle fire exposure. It is a contrary to the findings from previous work [17, 28], where live load was reported to not have significant influence on the fire response of steel girder bridges. The deviation is attributed to the amount of loading and the location of the fire along the length of the bridge span. The findings from this study clearly demonstrate that in order to get the realistic fire response of steel girder it is necessary to consider the effect of live load.

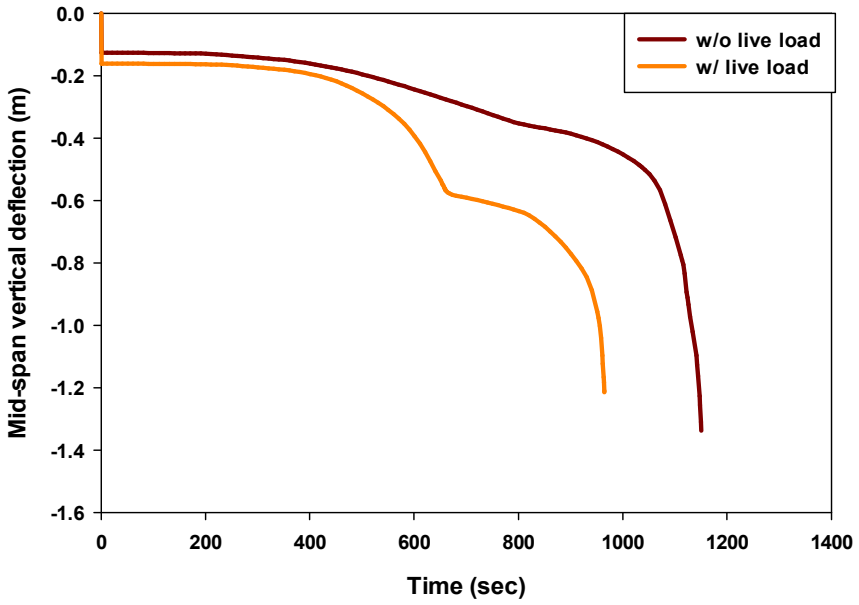

Figure 4-20: Influence of live loading on the mid-span deflection over time for heavy goods vehicle fire exposure.

4.5.4 Effect of Creep

The steel girder used in this study is partially restrained and experienced internal forces leading to internal stresses which vary as a function of fire exposure time and high temperature material properties [43]. Due to this, the effect of high temperature creep on the structural behavior of steel girder during fire was investigated. The time hardening form (creep strain rate depends only upon the time) available in Abaqus was invoked in the model. Figure 4-21 contains a comparison of the mid-span vertical deflection for the bus fire and tanker fire exposures. For

the bus fire exposure, the predictions including creep increase the deflection by 6% over the simulations without creep whereas for the tanker fire exposure the difference is as much as 42%. This deviation is attributed to the higher temperatures and stresses that are experienced in the tanker fire exposure. The findings show that creep will affect the deflection response with the significance dependent on temperature reached.

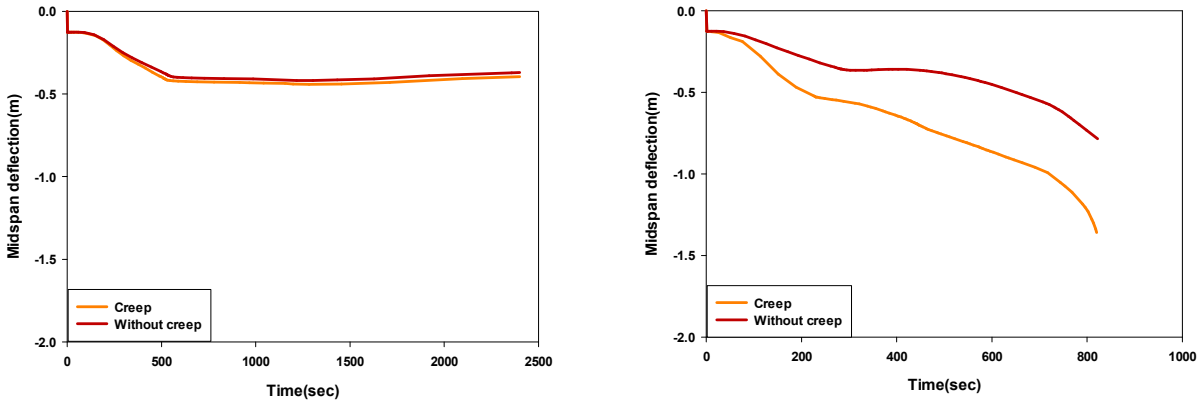

(a) (b)

Figure 4-21: Influence of high temperature creep on the global maximum deflection over time for a) bus and b) tanker fire exposure.

4.6 Discussion

4.6.1 Uniform versus Non-uniform Fire Exposure

The influence of non-uniform localized vehicle fire exposures onto the bridge structural steel girder-concrete deck assembly was further evaluated by comparing the reaction forces at the ends of the assembly, strain distribution and stress levels.

Figure 4-22 contains a comparison of the axial force exerted by the steel girder-concrete deck assembly on the rigid end supports for the i) heavy goods vehicle and ii) ISO-834 fire exposures as a function of bottom flange temperature. For the heavy goods vehicle fire exposure, the bottom flange temperature represented the average temperature over the width of the bottom flange at mid-span. It is seen that for the ISO 834 fire exposure the axial force begins to increase at a bottom flange temperature of 200°C whereas for the heavy goods vehicle exposure the axial force starts to develop at a bottom flange temperature of 400°C. The uniform heating over the

entire length of a 37m steel girder for the ISO 834 fire exposure resulted in more axial force at a lower temperature in comparison to the non-uniform heating from the heavy goods vehicle fire exposure.

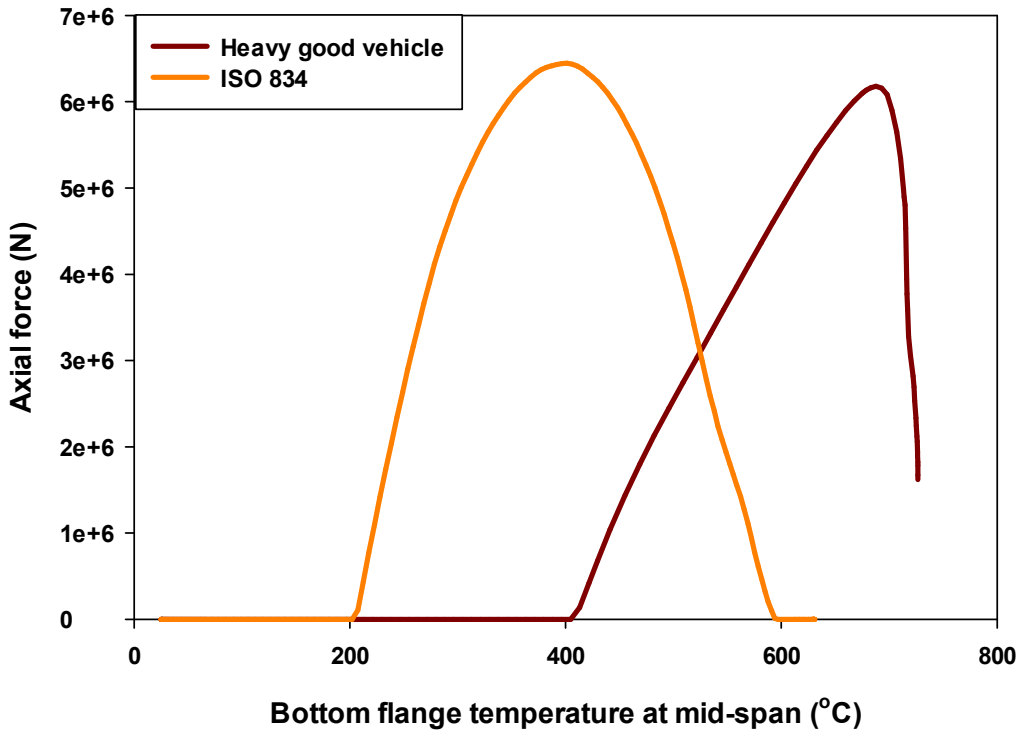

Figure 4-22: Reaction forces at steel girder ends for the heavy goods vehicle and ISO 834 fire exposures.

The maximum principal strain distribution of the steel girder near the ends and at mid-span are shown in Figure 4-23 for the heavy goods vehicle and ISO 834 fire exposure at the time of failure. All maximum principal strains were scaled to a maximum of 0.2 (strain limit), and the grey region corresponds to the region where the element maximum strain exceeded 0.2. The plot shows the difference in structural response between the heavy goods vehicle and the ISO 834 fire exposures. The uniform heating over the entire length for the ISO 834 fire exposure resulted in local flange buckling of the steel girder assembly near the ends due to the large axial compressive force from thermal expansion, see Figure 4-23. The steel girder assembly does not

fail immediately, but the load is redistributed to the regions of higher stiffness. The additional moment resulted in more downward deflection of the steel girder assembly which continues to increase with the loss of material stiffness at higher temperature. The steel girder assembly eventually fails due to excessive downward deflection. For the non-uniform heating due to the heavy goods vehicle fire exposure, local buckling occurs in the bottom flange at the mid span where the highest temperatures are located as shown in Figure 4-23. After the local buckling of the bottom flange, the steel girder assembly does not fail immediately and the load is redistributed to regions with higher stiffness. In addition, the non-uniform heating resulted in a lower mid-span deflection as the regions outside of the localized heating zone were at lower temperature. As the temperatures increased, the steel girder fails by to the formation of plastic hinge. Figure 4-24 contains a plot of the stress at the mid span as a function of temperature. At the time of failure, the stress in the bottom flange exceeds the ultimate strength of the steel at its temperature whereas for the ISO 834 fire exposure the stress in the bottom flange does not exceed the ultimate strength of steel at its temperature.

4.6.2 Response of Full Scale Highway Bridge

Previous simulation results reported herein were on the middle steel girder concrete deck assembly of a multi-lane highway bridge that consists of a seven steel girder, concrete deck composite assembly. The study accounted for the accurate fire physics from the localized vehicle fire exposure, but the effects of the adjacent six steel girders on the structural response were not included. As a result, the thermo-structural response of the entire steel girder-concrete deck composite bridge with a heavy goods vehicle fire exposure was evaluated in this study and the results were compared with the results from a single girder steel girder.

Figure 4-25 provides the thermal response predictions of the bottom flange of the seven steel girders of a typical full scale highway bridge. The temperatures presented here are averaged over the width of the bottom flange at mid-span. It is seen that the bottom flange temperatures of the outermost girders (1 and 7) reach a maximum of 244°C whereas the bottom flange temperature of the middle girders (3, 4, and 5) reach a maximum temperature of 933°C. The difference in temperature rise of girders 1 and 7 is attributed to the asymmetry of the fire location relative to the width of the highway bridge.

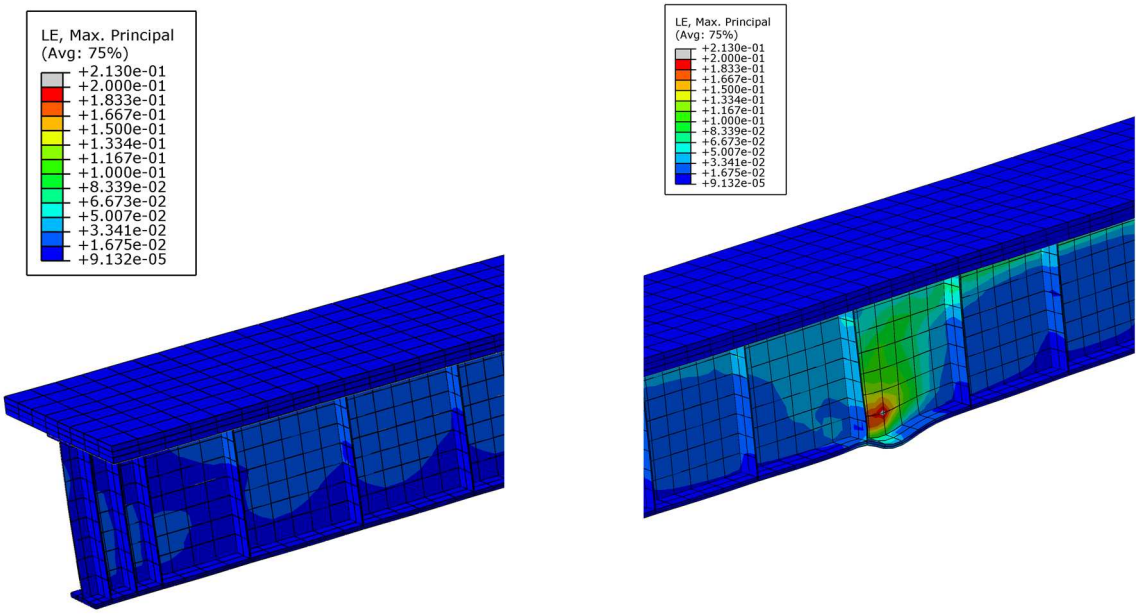

Near the end At mid-span

(a)

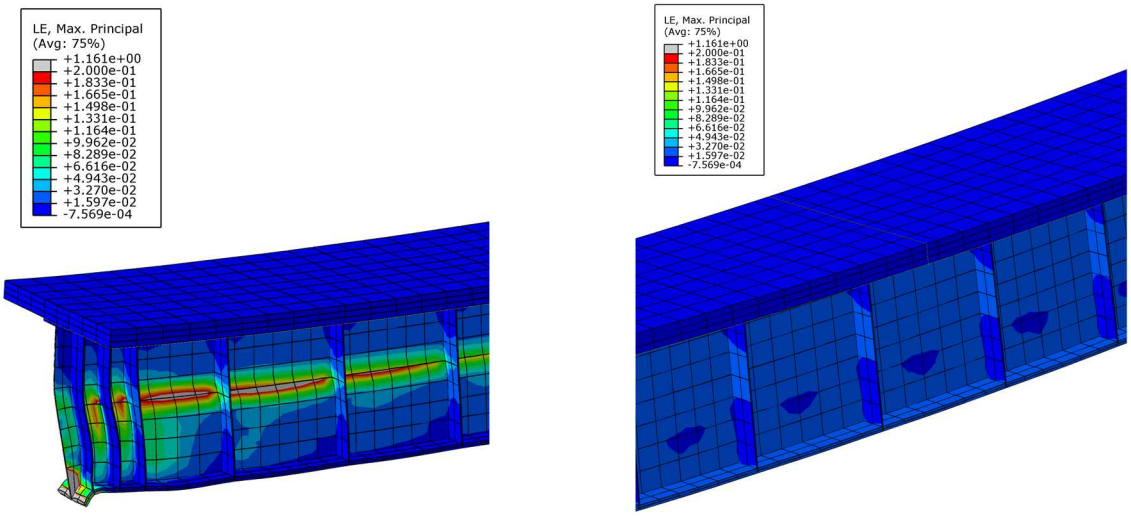

Near the end At mid-span

(b)

Figure 4-23: Strain distribution at the time of failure for a) the heavy goods vehicle and b) the ISO 834 fire exposure.

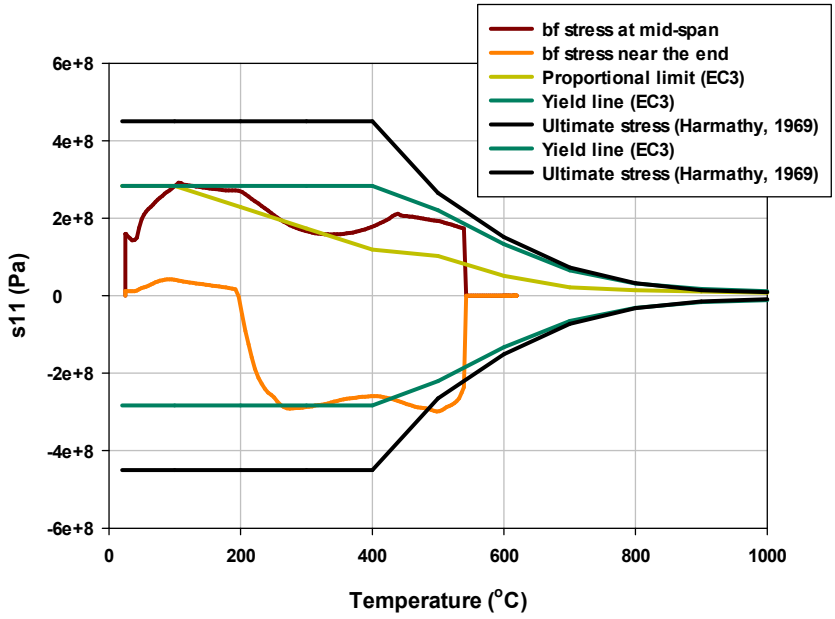

(a)

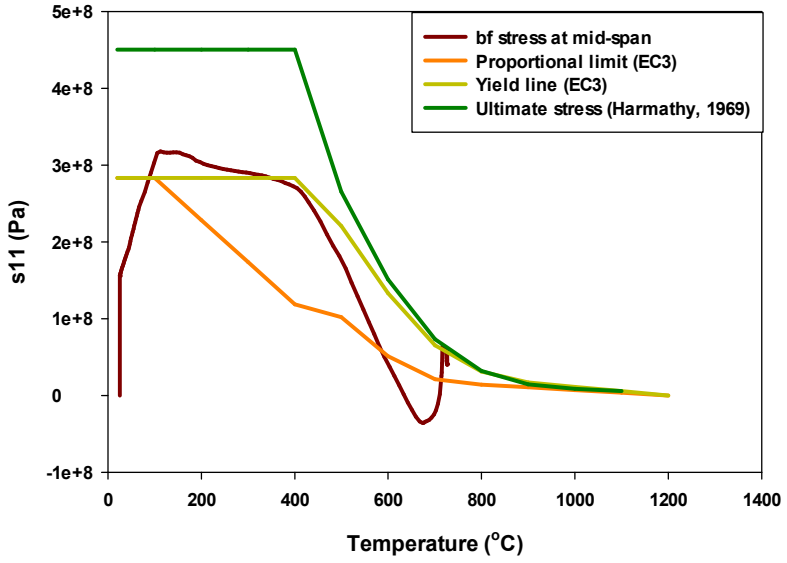

(b)

Figure 4-24: Evolution of bottom flange stress in the axial direction (s11) with time for a) the ISO 834 and b) the heavy goods vehicle fire exposure.

Figure 4-26 contains a comparison of the mid-span vertical deflection for the entire highway bridge and a single steel girder-concrete deck assembly up to the onset of failure. As seen in Figure 4-26a, at approximately 200 s the entire highway bridge starts to deflect more in comparison to the single girder assembly. This is attributed to the higher self-weight and dead load resulting from the entire bridge. At approximately 640 s, the single girder assembly starts to deflect more than the entire bridge and eventually fails at 692°C. The single girder assembly was predicted to fail sooner than the entire bridge assemble, which failed at 907 s. The spatial distribution of vertical deflection of the entire highway bridge is shown in Figure 4-26b at the time of failure (907 sec). The longer survival time for the entire bridge was attributed to the load redistribution to the outer girders which remain at lower temperature and still have sufficient load carrying capacity. The study demonstrates that the analysis with a single steel girder-concrete deck assembly will provide conservative results.

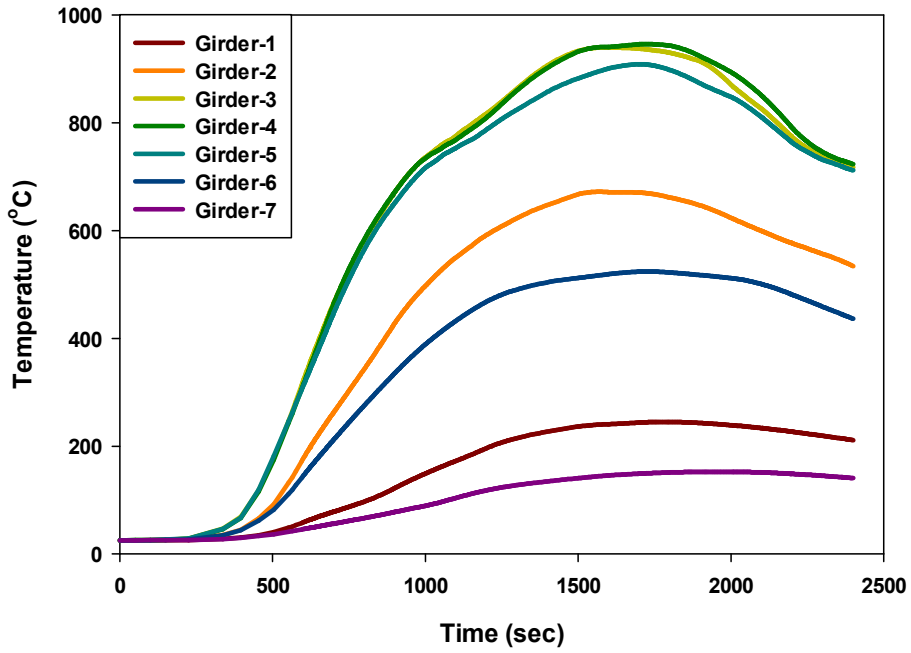

Figure 4-25: Bottom flange temperature response for different steel girders of an entire highway bridge with a heavy goods vehicle fire exposure.

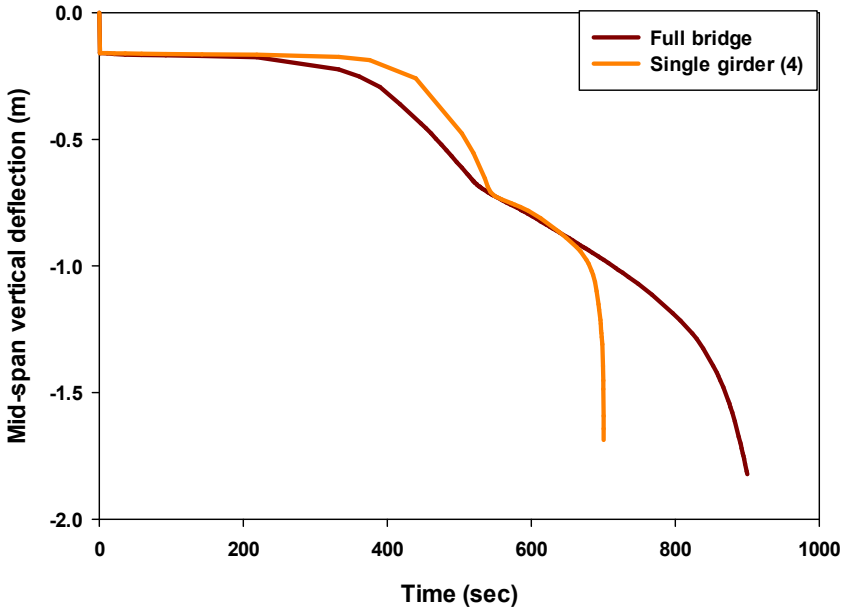

(a)

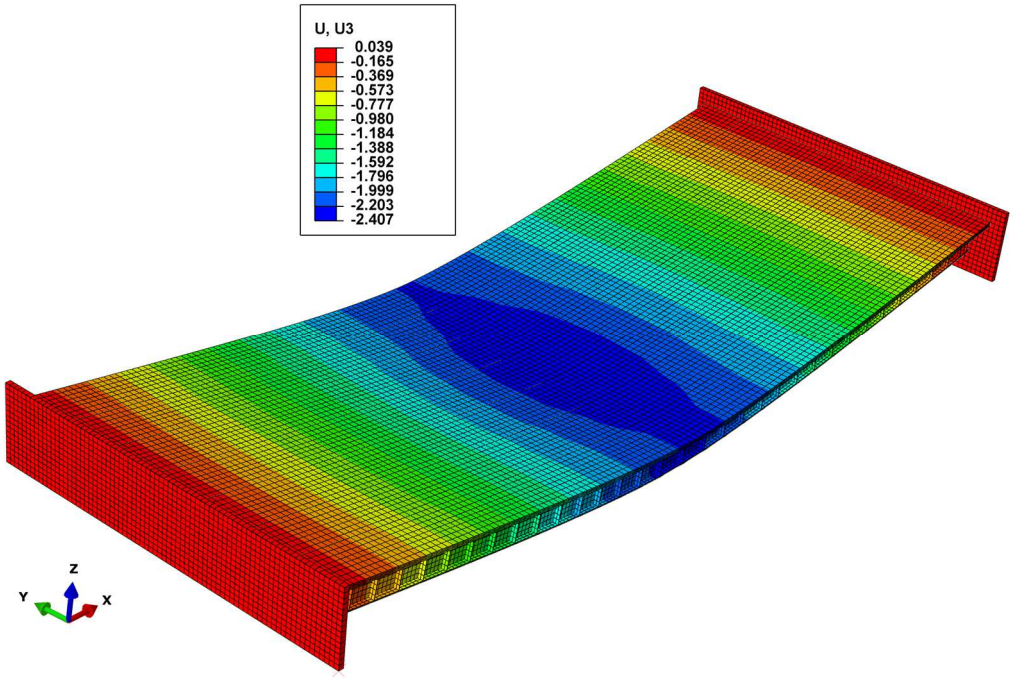

(b)

Figure 4-26: a) A comparison with mid-span deflection response of a single girder assembly with an entire bridge assembly and b) spatial distribution in deflection of the entire bridge just prior to failure at 907s.

4.7 Summary and Conclusions

A series of simulations were performed to investigate the behavior of a bridge exposed to realistic, non-uniform fire exposures as well as uniform standard fire exposures. Simulations of the response of a highway bridge during a fire exposure were performed using fire, thermal and structural models that were sequentially coupled. The CFD model FDS was coupled with Abaqus through a user-subroutine developed in this work. Through this subroutine, the temporal and spatial heat flux due to the fire exposure was imported into Abaqus. The thermal and structural analyses were then conducted within Abaqus with the material properties as a function of temperature. The modeling approach was validated with two sets of experimental data.

The modeling methodology was used to predict the temperature rise and structural integrity of a single steel girder-concrete deck assembly exposed to vehicle and standard fire exposures. The influences of creep, structural boundary conditions, and loading levels on the structural response were also investigated. Based on the results, the following conclusions were determined :

- Vehicle fire exposures produce a strong thermal gradient along the length of the bridge girders as opposed to the standard fire exposure which heats up the girder similarly along its length.
- Vehicle fire exposures resulted in the local buckling of bottom flange at a higher temperature (682°C for Heavy goods vehicle (HGV) exposure) in comparison to the standardized furnace fire exposure (258°C for ISO 834 exposure).
- Localized heating from the vehicle fire exposure resulted in smaller downward deflection and caused failure of the steel girder assembly with the formation of a plastic hinge at the midspan whereas standard furnace fire exposures resulted in excessive deflection at the midspan.
- Not all the vehicle fires impose a threat to the stability of a highway bridge. Vehicles, such as a buses or passenger cars, which produce lower heat release rates (typically less than 50 MW) were not predicted to cause any permanent damage to the steel girder-concrete deck assembly considered in this study. However, vehicles such as a box truck or fuel tanker that produce moderate to large heat release rates (100 – 300 MW) were predicted to cause bridge failure.

4.8 References

[1] F. P. Bulwa D. (2007, Tanker fire destroys part of MacArthur maze. *2007(29)*.

[2] M. Garlock, I. Paya-Zaforteza, V. Kodur, and L. Gu, "Fire hazard in bridges: Review, assessment and repair strategies," *Engineering Structures,* vol. 35, pp. 89-98, 2012.

[3] Battelle. (2004, Comparative risks of hazardous materials and non-hazardous materials truck shipment accidents/incidents. *Federal Motor Carrier Safety Adminstration*.

[4] N. F. P. A. (NFPA). (2008, NFPA 502 Standard for road tunnels, bridges and other limited access highways. *NFPA*.

[5] H. Ingason and A. Lönnermark, "Heat release rates from heavy goods vehicle trailer fires in tunnels," *Fire Safety Journal,* vol. 40, pp. 646-668, 2005.

[6] A. H. Buchanan, *Structural design for fire safety* vol. 273: Wiley New York, 2001.

[7] H. Ingason, "Model scale railcar fire tests," *Fire Safety Journal,* vol. 42, pp. 271-282, 2007.

[8] R. Carvel, A. Beard, P. Jowitt, and D. Drysdale, "The influence of tunnel geometry and ventilation on the heat release rate of a fire," *Fire Technology,* vol. 40, pp. 5-26, 2004.

[9] I. D. Bennetts, D. Proe, R. Lewins, and I. Thomas, "Open deck car park fire tests," 1985.

[10] V. Babrauskas, "Heat release rates," *SFPE handbook of fire protection engineering,* vol. 3, pp. 3-1, 2002.

[11] A. Lönnermark, "On the characteristics of fires in tunnels," Lund University, 2005.

[12] ISO-834, "Fire resistance tests-elements of building construction - Part 1.1: General Requirements for Fire Resistance Testing," ed. Geneva, Switzerland: International Standard Organization, 1975.

[13] A. E119, "Standard Test Methods for Fire Tests of Building Construction and Materials," ed. Philadelphia, PA: American Society for Testing and Materials, 1995.

[14] D. Wainman and B. Kirby, *Compendium of UK Standard Fire Test Data: Unprotected Structural Steel*: British Steel Corporation, Swinden Laboratories, 1988.

[15] T. Liu, M. Fahad, and J. Davies, "Experimental investigation of behaviour of axially restrained steel beams in fire," *Journal of Constructional Steel Research,* vol. 58, pp. 1211-1230, 2002.

[16] V. Kodur, E. Aziz, and M. Dwaikat, "Evaluating fire resistance of steel girders in bridges," *Journal of Bridge Engineering,* vol. 18, pp. 633-643, 2012.

[17] I. Payá-Zaforteza and M. Garlock, "A numerical investigation on the fire response of a steel girder bridge," *Journal of Constructional Steel Research,* vol. 75, pp. 93-103, 2012.

[18] D. Gottuk and B. Lattimer, "SFPE Handbook of Fire Protection Engineering," *National Fire Protection Association,* vol. 2, pp. 54-2, 2002.

[19] P. A. Friday and F. W. Mowrer, *Comparison of FDS model predictions with FM/SNL fire test data*: National Institute of Standards and Technology Gaithersburg, MD, 2001.

[20] J. Floyd, G. Forney, S. Hostikka, T. Korhonen, R. McDermott, and K. McGrattan, "Fire Dynamics Simulator Technical Reference Guide-Volume 3: Validation," *National Institute of Standards and Technology: Gaithersburg, Maryland, USA,* 2013.

[21] A. Pchelintsev, T. Hasemi, T. Wakamatsu, and Y. Yokobayashi, "Experimental and Numerical Study on the Behavior of a Localized Steel Beam Under Ceiling Exposed to a Localized Fire," in *Fire Safety Science--Proceedings of the Fifth International Symposium*, 1997, pp. 1153-1164.

[22] V. Kodur, L. Gu, and M. E. M. Garlock, "Review and assessment of fire hazard in bridges," *Transportation Research Record: Journal of the Transportation Research Board,* vol. 2172, pp. 23-29, 2010.

[23] W. I. Alnahhal, M. Chiewanichakorn, A. J. Aref, and S. Alampalli, "Temporal thermal behavior and damage simulations of FRP deck," *Journal of Bridge Engineering,* vol. 11, pp. 452-464, 2006.

[24] I. Bennetts and K. Moinuddin, "Evaluation of the impact of potential fire scenarios on structural elements of a cable-stayed bridge," *Journal of Fire Protection Engineering,* vol. 19, pp. 85-106, 2009.

[25] J. Choi, *Concurrent fire dynamics models and thermomechanical analysis of steel and concrete structures*: ProQuest, 2008.

[26] H. Eisel, N. Palm, W. Prehn, and G. Sedlacek, "Fire damages and repair of the Wiehltalbridge at motorway A4, Cologne-Olpe," *Stahlbau,* vol. 76, pp. 94-104, 2007.

[27] H. S. McGrattan K., Floyd J., Baum H., Rehm R., Mell W., McDermott R. (October 29, 2010, Fire Dynamics simulator (Version 5), Technical Reference Guide. *Volume 1: Mathematical model*.

[28] J. Alos-Moya, I. Paya-Zaforteza, M. Garlock, E. Loma-Ossorio, D. Schiffner, and A. Hospitaler, "Analysis of a bridge failure due to fire using computational fluid dynamics and finite element models," *Engineering Structures,* vol. 68, pp. 96-110, 2014.

[29] J. Floyd, G. Forney, S. Hostikka, T. Korhonen, R. McDermott, and K. McGrattan, "Fire Dynamics Simulator User's Guide," *Gaithersburg, Maryland, USA,* 2013.

[30] D. S. Simulia, "Abaqus 6.12 documentation," *Providence, Rhode Island, US,* 2012.

[31] K. Hiroshi and Y. Taro, "Air entrainment and thermal radiation from heptane pool fires," *Fire Technology,* vol. 24, pp. 33-47, 1988/02/01 1988.

[32] E. C. f. S. (CEN). (2004, Eurocode 2: Design of concrete structures - part 1-2: general rules - structural fire design. *CEN*.

[33] E. C. f. S. (CEN). (2005, Eurocode 3: Design of steel strucutres - part 1-2: general rules - structural fire design. *CEN*.

[34] E. C. f. S. (CEN). (2002, Eurocode 1 Actions on structures, part 1-2: general actions - actions on structures exposed to fire. *CEN*.

[35] R. Siegel and J. Howell, "Thermal radiation heat transfer. 2002," ed: Taylor and Francis, New York.

[36] X. Dai, Y. Wang, and C. Bailey, "Numerical modelling of structural fire behaviour of restrained steel beam–column assemblies using typical joint types," *Engineering Structures,* vol. 32, pp. 2337-2351, 2010.

[37] G. Heskestad, "SFPE Handbook of Fire Protection Engineering, chapter Fire Plumes, Flame Height and Air Entrainment," *National Fire Protection Association, Quincy, Massachusetts,* vol. 6, p. 86, 2002.

[38] CEN, *Eurocode 1, Actions on Structures: General actions; actions on structures exposed to fire*. Brussels, Belgium: European Committee for Standardization, 2002.

[39] R. Siegel and J. R. Howell, *Thermal Radiation Heat Transfer*: Taylor & Francis, 2002.

[40] J. Myllymaki and M. Kokkala, "Thermal exposure to a high welded I-beam above a pool fire," in *First international workshop on structures in fires, Copenhagen*, 2000, pp. 211-226.

[41] Y. Hasemi, S. Yokobayashi, T. Wakamatsu, and A. Ptchelintsev, "Firesafety of building components exposed to a localized fire: scope and experiments on ceiling/beam system exposed to a localized fire," *Proceedings of ASIAFLAM,* pp. 351-361, 1995.

[42] M. Nahid and B. Y. Lattimer, "Modeling thermal response of steel–concrete floor systems in a furnace," *Fire Safety Journal,* 2014.

[43] V. Kodur and M. Dwaikat, "Effect of high temperature creep on the fire response of restrained steel beams," *Materials and structures,* vol. 43, pp. 1327-1341, 2010.

[44] B. Fields and R. Fields, "Elevated temperature deformation of structural steel," 1988.

[45] H. M. Ali, P. E. Senseny, and R. L. Alpert, "Lateral displacement and collapse of single-story steel frames in uncontrolled fires," *Engineering Structures,* vol. 26, pp. 593-607, 2004.

[46] H. Koseki, "Large scale pool fires: Results of recent experiments," in *Proceedings of the 6th International Symposium of Fire Safety Science*, 1999, pp. 5-9.

[47] Woodworth M.A. (2013). Fire Hazard Assessment for Highway Bridges with Thermal Mechanical Modeling (Doctoral dissertation, Virginia Polytechnic institute and state university).

[48] Wright W., Lattimer B., Woodworth M., Nahid M., Sotelino E., (2013), NCHRP Project No. 12-85: Highway Bridge Fire Hazard Assessment, Transportation Research Board of the National Academies, Washington, DC (2013)

5 Thermo-Structural Response of Highway Bridge Structures with Tub Girder and Plate Girder

5.1 Introduction

In recent years, a number of highway bridge fires occurred throughout the U.S. and the rest of the world with catastrophic outcomes including those in Birmingham, Alabama with one death [1, 2] and the complete collapse of the bridges located in Oakland, CA and Hazel Park, MI [2]. A voluntary bridge failure survey conducted by the New York Department of Transportation in 2008 [3], found that 52 bridges collapsed due to fire out of 1,746 bridge failures. According to the survey, nearly three times more bridges collapsed due to fires compared to earthquakes [4]. The main reasons for the catastrophic outcome are that some vehicles contain large combustible loads such as the cargo, seats made of polyurethane foam, and petroleum products. Also, the unlimited access of ventilation allows the fires to grow large. Despite the frequency of occurrences and the severity of highway bridge fire incidents, fire has been neglected as one of the primary extreme event design considerations in highway bridge design codes [5, 6]. Passive fire protection is commonly attached or applied to steel surfaces to achieve desired structural integrity performance [7]. In bridges, this is less desirable due to cost, maintenance, and limiting surface inspection. Therefore, can the steel girders be designed in a way to improve the structural integrity of the bridge without the need for passive fire protection applied onto the steel surface?

Few studies have been performed to identify the factors that influence the structural integrity of bridges during a localized vehicle fire. The influence of live load, material properties and the effect of boundary conditions on the fire response of steel girder bridges were studied by Paya-zaforteza *et al.* [8] and Alos Moya *et al.* [9]. Glassman *et al.* [10] studied incorporating diagonal stiffeners as well as protecting the stiffener alone on improving the girder structural integrity. The previous studies concluded that the investigated parameters had little influence on the thermo-structural response of steel girder bridges during fire. Previous work has not focused on modifying the girder designs to limit the flame exposure on the steel through changing the fire dynamics.

Simulating the thermo-structural response of highway bridge structural elements during a fire exposure is a multi-physics problem that involves predicting the vehicle fire exposure as well

as the thermal and structural response of both the steel girders and concrete deck. Fire exposures onto highway bridges are non-uniform, local type fire exposures which are characterized by high heating rates and can reach very high temperatures within the first few minutes of the fire exposure. A local fire exposes a portion of the bridge structural elements to flames. The open nature of the fire allows the flames flow along the length of the bridge as well as wrap around the bridge. Many bridges have a series of girders that run along the length of the bridge. If a fire occurs directly below the bridge, flames and hot gases may impinge upon the bottom of the concrete deck between two girders. In this scenario, the fire will flow beneath the bottom of the bridge exposing the deck and supports of the bridge to high heat flux levels. Restricting the flow of the fire in this manner has been determined to increase heat fluxes, which would result in higher heat fluxes to the bridge deck and structural supports compared with the fire impinging on an unobstructed ceiling [11].

The fire dynamics observed in simulations on bridges with multiple plate girders is similar to a fire impinging onto the ceiling of a narrow corridor, which has been previously tested. Based on data in [11], it was found that the fire impinging on a ceiling and flowing along a corridor produces higher heat fluxes (160 kW/m^2 for a fire size of 400 kW [12]) and longer flame extensions compared with the same size fire impinging on an unconfined ceiling (90 kW/m^2 for a fire size of 400 kW [13]). These results indicate that girder designs without gaps between them or preventing the flames from flowing between the plate girders through a flame deflector may reduce the thermal exposure by changing the flame dynamics and thermal exposure. Recently, tub girders, shown in Figure 5-1, are being considered as an alternative bridge girder design due to their higher bending resistance and torsional stiffness. A single tub girder would replace multiple plate girders, thus removing the bays between the plate girders and possibly reducing the thermal exposure during a fire.

Figure 5-1: Highway bridge structure with tub girder (photograph from Leonard G.)

A computational study is presented in this chapter to investigate the effect of modifying the steel girder design to remove the closely spaced bays to reduce the fire exposure and increase the structural integrity during a fire. This was done by predicting and comparing the fire response of a standard single lane steel girder-concrete deck composite assembly made of three plate girders with bays between girders, a single tub girder, three plate girders with a flame shield, and two tub girders. All simulations were performed with a heavy goods vehicle fire scenario, which causes the standard plate girder design to fail.

5.2 Bridge Geometry and Fire Scenario

The effect of a localized fire exposure on the behavior of highway bridge structure was studied on single and multi-lane concrete deck-steel girder composite assembly with a heavy goods vehicle fire exposure. Steel girders will be of different shape and arrangement that effects the movement of flame of the vehicle fire exposure and the heat flux to the specimen. As a result, two different types of steel girder (i.e., plate, tub) were selected to evaluate the fire performance of the highway bridge structure.

5.2.1 Highway Bridge Geometry

To predict the heating mechanism of highway bridge structural elements under localized fire conditions, two different single lane highway overpass bridges made of plate and tub girder according to the specifications of the Federal Highway Administration (FHWA) were selected for analysis. The plate girder bridge consists of three built in plate girders supporting a reinforced concrete slab 6.0 m wide and 160 mm thick. The girders are assumed to be in full composite action with the slab and have two expansion joints at its ends with a width of 72mm. Each plate girder has a total of 34 stiffeners with a thickness of 25.4mm. The span length of the bridge is 37.0 m and the geometric definitions of the plate girder bridge are provided in Figure 5-2. In contrast, tub girder bridge consists of a single tub girder supporting a reinforced concrete slab 6.0 m wide and 160 mm thick. Similar to the plate girder bridge, the tub girder is assumed to be in full composite action with the slab and have two expansion joints at its ends with a width of 72mm. The geometric definitions of the tub girder bridge are provided in Figure 5-2.

Most of the highway bridges in the US and the rest of the world consist of multiple lanes, which would require with two and more tub girders. As a result, a multi-lane bridge with two tub girders was selected to evaluate the effect of spacing between adjacent tub girders on the fire response of the bridge assembly. The study also evaluated the influence of utilizing a flame shield made of steel between the adjacent lower flanges of the girders in reducing the fire exposure. The cross section views of the bridge geometry studied are provided in Figure 5-3.

5.2.2 Fire Exposure

Fire scenarios for highway bridges may include different types of burning vehicles which result in different fire heat release rates, duration, and diameters. In the previous chapter it was found that not all the vehicle fires impose a threat to the stability of a bridge. Vehicles, such as a buses or passenger cars, with that produce lower heat release rates (typically less than 60 MW) were not predicted to cause any permanent damage to the steel bridge girder elements. However, vehicles such as a heavy goods vehicle or fuel tanker that produce moderate to large heat release rates (150 – 300 MW) will cause localized failure of steel girder elements. A heavy goods vehicle fire scenario was selected to evaluate the heating of bridge structural elements during a fire to determine if failure could be prevented through a modified girder design. The heat release rate produced from heavy goods vehicle fire with time was reported by Ingasson [14] and is

provided in Figure 5-4. The dimensions of the heavy goods vehicle were 3.0 m wide, 10.5 m long with elevation of the base of the fire being 1.0 m. The simulations were conducted with the fire located at mid-span of the highway bridge. Based on the results on the effect of fire location, it was found that fire located at mid-span is one of the worst case scenarios [28].

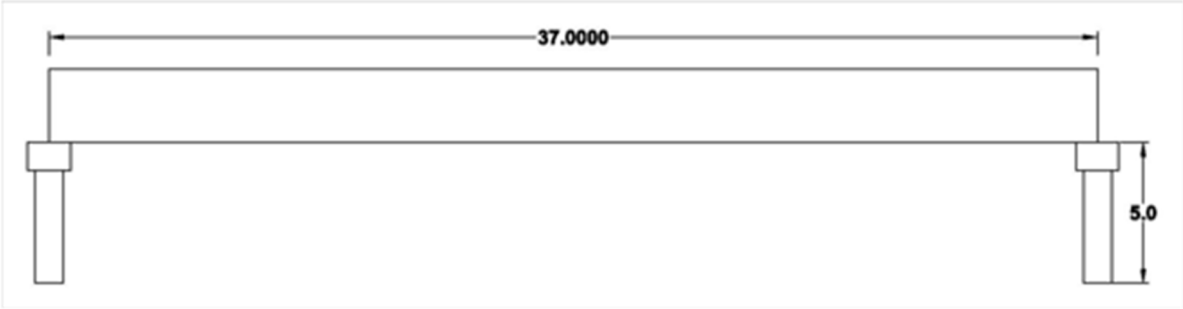

(a)

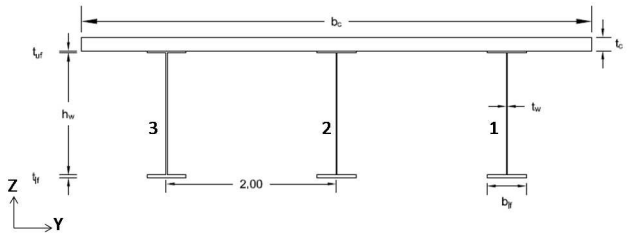

(b)

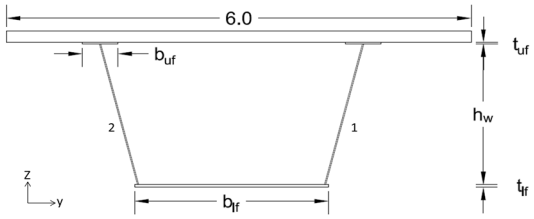

(c)

	Plate Girder(m)	Tub Girder(m)
b_c	6.0	6.0
t_c	0.16	0.16
t_{uf}	0.0254	0.02
b_{uf}	0.46	0.46
t_w	0.01	0.016
h_w	1.4365	2.03
t_{lf}	0.0381	0.03
b_{lf}	0.46	2.5

(d)

Figure 5-2: The model geometry of single lane highway bridge structure: a) elevation view, cross section view of b) plate girder, c) tub girder, and d) geometric definition.

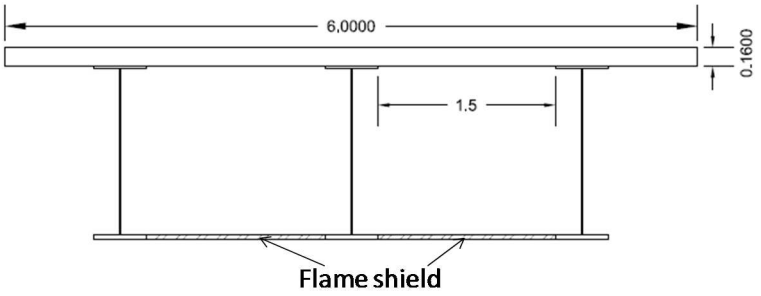

(a) Single lane plate girder highway bridge with flame shield

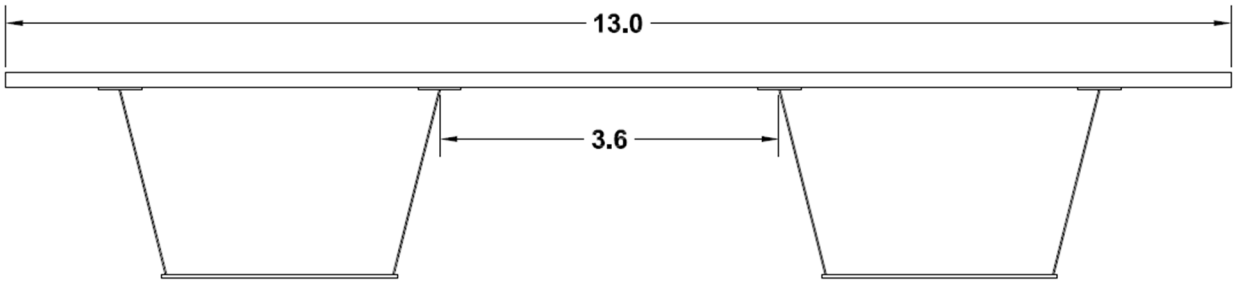

(b) Multi-lane tub girder highway bridge

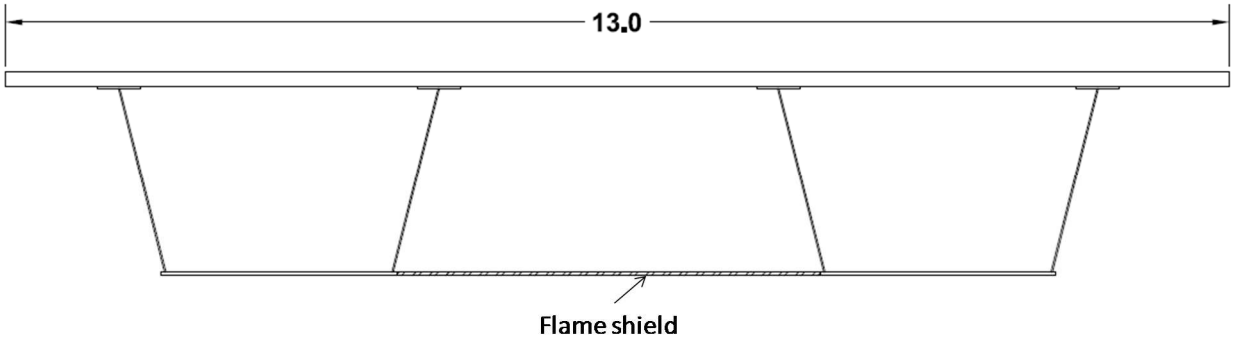

(c) Multi-lane tub girder highway bridge with flame shield

Figure 5-3: Cross-section view of different highway bridge geometry studied.

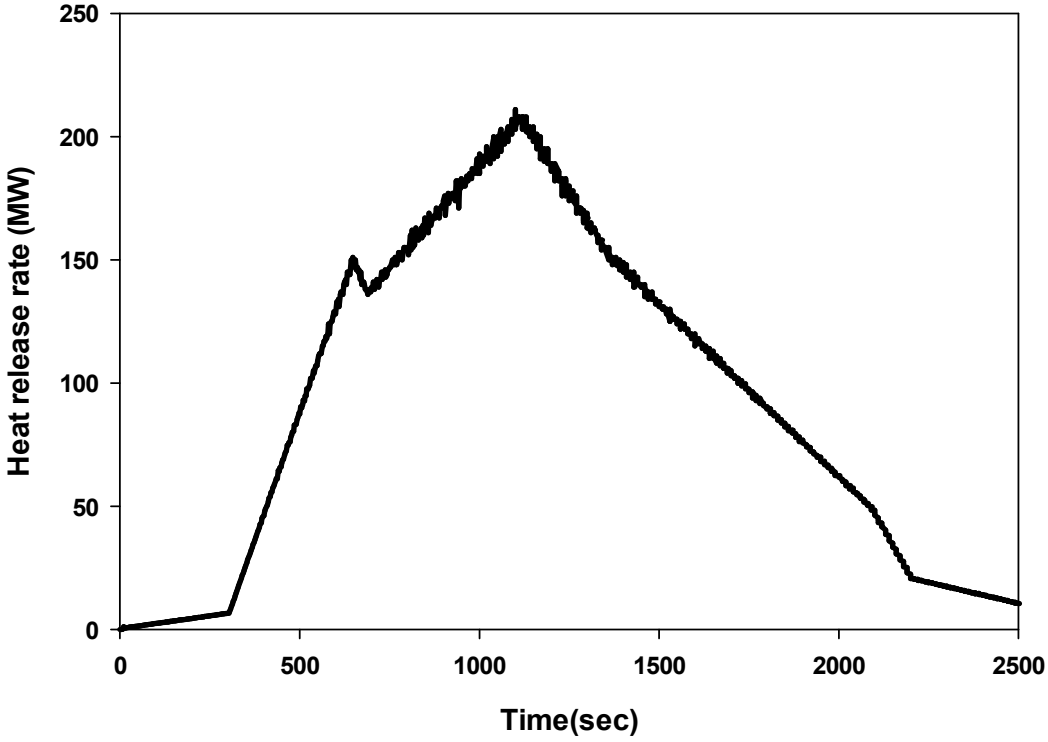

Figure 5-4: Profile of heat release rate for the heavy goods vehicle fire.

5.3 Modeling Methodology

A multi-physics based modeling approach developed and verified in Chapter 4 was used to predict the fire behavior of steel girder, concrete deck composite bridges with a vehicle fire exposure. This model involves the loosely coupled modeling of vehicle fire physics, 3D transient heat transfer and non-linear structural response. The motivation for using the loosely coupled fire-thermal-structural model is based on the use of different scales of mesh appropriate for each type of model.

5.3.1 Coupled Fire-Thermal-Structural Model

Fire, thermal, and structural models must be coupled to predict bridge response due to a local vehicle fire to adequately capture the physics controlling the structural response. Vehicle fires occurring underneath the highway bridges will not heat the whole bridge uniformly; it will create localized regions of higher temperature. This will induce temperature gradients both along

the length and height of the bridge structural components. These temperature gradients will induce differential thermal expansion of the components that can result in very high internal stresses and distortion of individual elements. Boundary conditions of the bridge (determined by the presence of expansion joints, bearings, substructure elements, and adjacent spans) also have a large influence on the development of internal forces. Therefore, the modeling methodology must provide a reasonably accurate simulation of nonuniform heating conditions. This includes both the spatial and temporal heat flux distribution onto the different structural elements. Assuming the thermal boundary conditions are accurately predicted, there remains considerable complexity in predicting the thermal and structural response. As a result, a three-dimensional finite element model is required to understand the bridge element response. The mechanical properties of materials change as a function of temperature, requiring a non-linear material formulation. The thermal properties as a function of temperature for the components must also be input to accurately predict the temperature rise of structural components. Non-linear effects such as creep and local buckling are also expected and need to be included in the model.

In this work, the bridge response was predicted through a series of three sequentially coupled analyses: fire analysis, thermal analysis, and structural analysis. Figure 5-5 shows the flowchart of the sequentially coupled vehicle fire modeling methodology. The fire simulations were performed using the computational fluid dynamics code Fire Dynamic Simulator (FDS) [15] developed by NIST. FDS was used to predict the transfer of heat from the fire environment onto the bridge structural members. The three-dimensional heat transfer analysis was then performed using the commercial finite element code Abaqus 6.12 [16]. The heat flux boundary condition generated in FDS that represents the heat transfer to the bridge structural elements during a fire exposure was imported into Abaqus through a custom-developed user subroutine DSFLUX. The Abaqus thermal model was used to simulate the temperature rise of the bridge components. The predicted temperature rise was then imported into an Abaqus structural response model to determine the response of the structure at high temperatures. The structural model used non-linear, high temperature mechanical properties of the bridge materials. External loads (gravity and dead load) were held constant during the analysis. In this study, all simulations were performed on a standard x86-Linux cluster with a dual-socket quad-core 2.26 GHz Intel Nehalem processor and 24GB of memory.

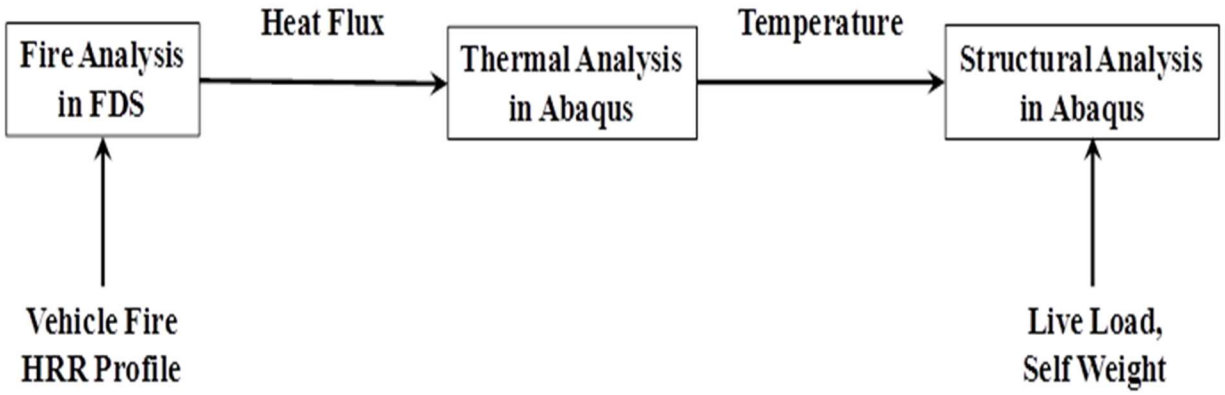

Figure 5-5: A flow chart for modeling the bridge response due to a vehicle fire.

5.3.2 Fire Model in FDS

Fire simulations were conducted using Fire Dynamics Simulator (FDS), Version 6.0 [15]. FDS is a computational fluid dynamics (CFD) model that uses large-eddy simulation to predict the buoyancy driven flows, thermal conditions and species concentrations that develop due to fire. FDS includes predictions of conditions in the gas phase as well as the condensed phase (i.e., solid boundaries). In the gas phase, FDS predicts the fire plume location, heat release rate of the fire, gas species concentrations, soot and visibility through smoke. Radiative heat transfer problems have been solved using the radiation transport equation for a gray gas. A technique similar to Finite Volume Method (FVM) has been used to solve this equation, while the absorption coefficients have been calculated using RADCAL narrow band model. FDS uses the fire conditions to predict heat fluxes to the boundaries. Boundaries can consist of multiple layers of materials but must be of rectilinear in shape to conform to that of the rectilinear grid.

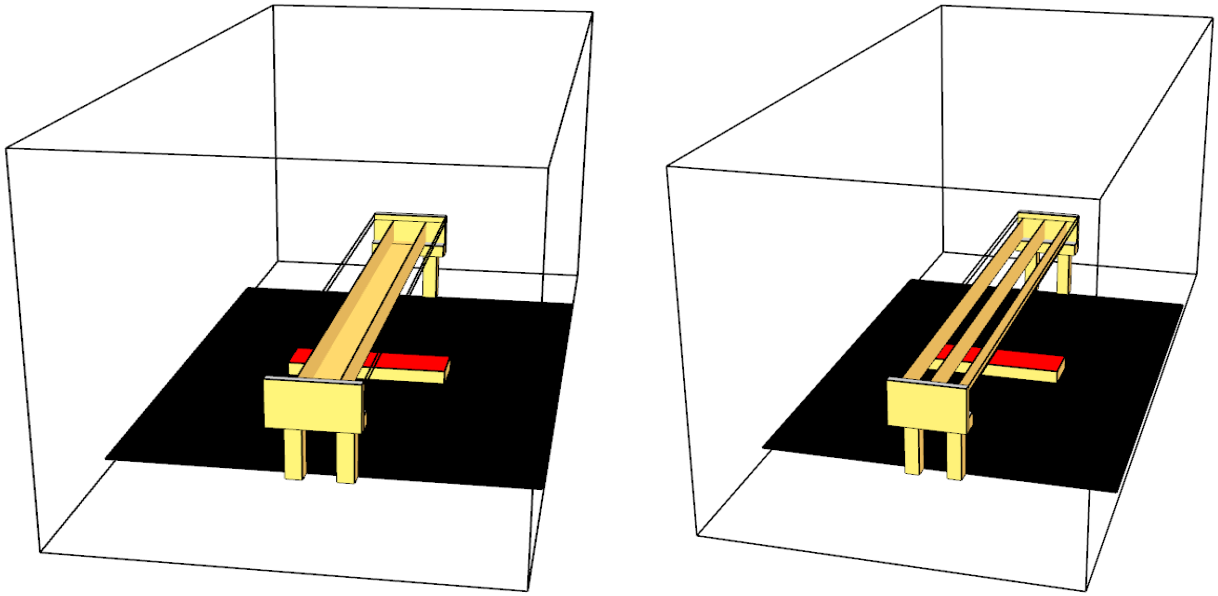

Figure 5-6: The FDS fire model of the a) plate girder and b) tub girder single lane highway bridge (bridge deck removed to show girder detail).

The FDS models of the two single lane highway bridges are shown in Figure 5-6. The model included the pier supports, piers at the two ends, and the road underneath the bridge to ensure proper flow within and around the bridge. In the FDS model of the plate girder bridge, the girders were modeled as the web only excluding the lower flanges, upper flanges and girder stiffeners. Simulations were performed to demonstrate that the exclusion of the flanges does not significantly affect the flow field as well as heat exposure onto the web and concrete deck for the fires considered. In the three-dimensional heat transfer analysis, the heat exposure onto the lower flange, upper flange, and girder stiffeners were obtained through the linear interpolation of the web and concrete deck. In the FDS model of the tub girder bridge, the tub girders were modeled as a rectangular box girder. In order to capture the accurate fire physics the width of the bottom flange were kept similar as the original trapezoidal tub girder. It is believed that the box girder shape will create more confinement and recirculation of the flame at the intersection between the concrete deck and web of the box girder. As result, the fire exposure from the box girder bridge fire scenario will be higher and on the conservative side. In the three-dimensional heat transfer and structural analysis, the original trapezoidal box girder was used. The heat exposure onto the

slanted web was obtained through the linear interpolation of the straight web. The domain was extended in all directions to allow the free flow of gases into and out of the domain.

Table 5-1. Thermo-physical properties of the steel girder, concrete deck and furnace wall materials.

Temperature (K)	**Concrete**			**Steel**	
	k (W/mK)	c_p (J/kgK)	ρ (Kg/m^3)	k (W/mK)	c_p (J/kg-K)
293	1.95	900	2400	53.34	441.15
373	1.76	900	2400	50.67	521.42
453	1.59	980	2363	48.0	631.84
533	1.43	930	2330	45.34	779.24
613	1.29	970	2301	42.68	970.44
693	1.16	1100	2276	40.01	1212.25
773	1.04	1100	2259	37.35	1511.5
853	0.94	1100	2242	34.69	1875.0
933	0.85	1100	2225	32.02	832.69
1013	0.77	1100	2209	29.36	2525
1093	0.71	1100	2192	27.3	745.22
1173	0.66	1100	2175	27.3	435
1253	0.63	1100	2158	27.3	650
1333	0.61	1100	2141	27.3	650
1413	0.60	1100	2125	27.3	650

Table 5-2. Dimension of the computational domain, physical obstructions, heat release rate and fuel type for FDS simulations.

Vehicle Type	Fuel Type	Computational Domain (m)			Fire Dimension (m)			Cell Size (m)	Total no. of Cells
		Height	Width	Depth	Length	Width	Height		
Heavy goods vehicle	Gasoline	88.0	30.0	26.0	10.5	3.0	1.0	0.50	307,632

The time varying heat release rate of the fire was modeled as the ejection of gaseous fuel from the top surface of the vehicle by prescribing the heat release rate per unit area with time. The profiles of heat release rate from burning heavy goods vehicles are shown in Figure 5-4. The fire footprint was based on the size of the vehicle in the fire test [14]. The fuel inlet temperature was set equal to the boiling point of the type of fuel simulated. All FDS simulations were performed using the default turbulence model proposed by Deardorff [17]. Large scale fires result in a significant amount of soot production in the flaming region that blocks radiation from escaping from the fire [18]. Soot blockage increases with fire diameter and results in higher gas temperatures as the fire diameter increases. The level of soot blockage on fire exposure is modeled in FDS using the radiative fraction model approach developed and discussed in the previous chapter. Due to using the radiative fraction modeling approach, the soot and CO yield was set to 0.0 kg/kg. The elevated temperature thermo-physical properties for concrete and steel from the Eurocode [19, 20] were used in the FDS modeling and are given in Table 5-1. Though the temperature rise of the elements in FDS was not used as the thermal analysis, predicting the temperature rise of these surfaces was necessary to obtain reasonably accurate heat fluxes.

FDS simulations results greatly depend on the cell size chosen for the simulation. Floyd *et al.* [21] recommended that the ratio of characteristic fire diameter and cell size, $D^*/\delta x$, should be used for the prediction of the optimal grid size, where δx is the computational cell size and D^* is defined as

$$D^* = \left(\frac{\dot{Q}}{\rho_\infty c_p T_\infty \sqrt{g}}\right)^{2/5} \quad (1)$$

In this study, it was found that there should be 7 to 10 cells across the shorter dimension of the fire to get the converged results. The dimensions of the computational domain, ceiling and burner for all the simulations conducted are provided in Table 5-2. All domain boundaries were set to an open condition. Standard heat fluxes to the solid obstruction (steel web and concrete deck) were extracted from the simulations using a boundary file.

5.3.3 Thermal Model in Abaqus

The three dimensional heat transfer analysis simulations were conducted using Abaqus 6.12 [16]. In reality, during the fire exposure the bridge elements will receive radiation and convection from the fire; radiation from the ground and road; and the bridge elements will re-radiate heat back onto themselves and to the surroundings. In order to include these, a modified user-subroutine DSFLUX was used to import the standard heat fluxes predicted using FDS into Abaqus. The bridge elements are allowed to interact with the surrounding through convective and radiative interaction using the appropriate interactions for convection and radiation. For this, a heat transfer coefficient of 25 W/m^2-K [6] was used along with steel and concrete emissivity of 0.95 and 0.9, respectively [22]. The user-subroutine uses linear interpolation to account for the different meshing between the FDS and Abaqus models. In addition, the routine assigns heat fluxes to structural details that were included in the fire analysis. Specifically, the routine assigns heat fluxes to the flanges and web stiffeners based on interpolation from the predicted heat fluxes.

The thermal analysis of the steel concrete composite girder was carried out using Abaqus element DC3D20. This is a three dimensional 20-noded quadratic heat transfer brick element with a single degree of freedom at each node namely, temperature. The plate girder thermal model has 45,075 nodes and 6,288 solid elements whereas the tub girder thermal model has 29,800 nodes and 4,092 solid elements. Figure 5-7 contains the finite element mesh adapted for the thermal analysis. A convergence study was performed to choose the appropriate mesh that provides both reliable results and less computational time. In the model, thermal resistance between contact surfaces was not considered and the surfaces in thermal contact were forced to have the same temperature using TIE constraints. The thermal analysis on the steel-concrete

composite girder was conducted using temperature dependent thermal properties for steel and concrete. The properties used in the analysis are given in Table 5-2 and were taken from Eurocode 3 [19] for steel and Eurocode 2 [20] for concrete.

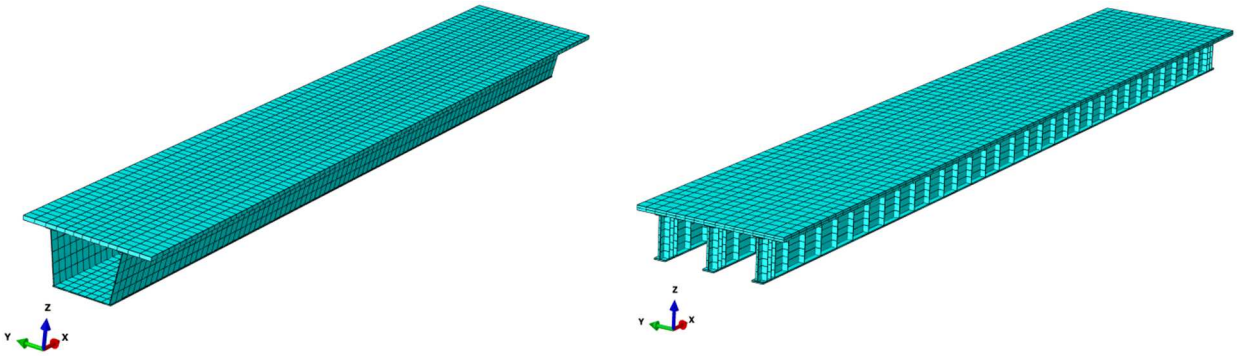

(a) (b)

Figure 5-7: Three dimensional finite element mesh of single lane highway bridge with a) tub girder b) plate girder for thermal analysis.

5.3.4 Structural Model in Abaqus

The structural analysis simulations of the steel girder-concrete deck composite bridges were conducted using Abaqus 6.12. In the simulation, three dimensional solid continuum 20-noded quadratic elements C3D20R were used for the steel girder while 8-noded linear elements C3D8R were used for the concrete deck. Both C3D20R and C3D8R have three degrees of freedom per node namely three translations in the x-, y- and z- directions. These elements are used to model three dimensional solids and are well suited for large deformation, large strain and non-linear problems. Woodworth [27] found that solid elements performed well at very coarse mesh densities reducing the computation time against more common shell elements. The plate girder structural model has 155,112 nodes and 24,349 solid elements whereas the tub girder structural model has 49,341 nodes and 13,215 solid elements. Figure 5-8 contains the finite

element mesh adapted for the structural analysis. A convergence study was performed to choose the appropriate mesh that provides both reliable results and less computational time. The total number of elements used in the structural analysis are higher than the total number of elements used in the thermal analysis as the convergence study reveals that more elements are required to accurately predict the stress and deformation of a structure. Note also that there were two elements across the width of the flange, three elements across the thickness of the flange and concrete deck, and five elements across the height of the web. In the model, the shear studs were not modeled and the surfaces in composite action were forced to have the same degree of freedom using TIE constraints.

The simulation was performed using the non-linear setting with a time step not exceeding 10 s. The mechanical properties namely stress-strain relationships, modulus of elasticity and thermal expansion were taken from Eurocode 3 [19] for steel and Eurocode 2 [20] for concrete. Figure 5-9 contains the stress-strain behavior with elevated temperature for steel. For input into Abaqus, true stresses (σ_n) and strains (ε_n) were computed from the engineering values of stresses (σ) and strains (ε) using

$$\sigma_n = \sigma(1+\varepsilon) \tag{2}$$

$$\varepsilon_n = ln(1+\varepsilon) \tag{3}$$

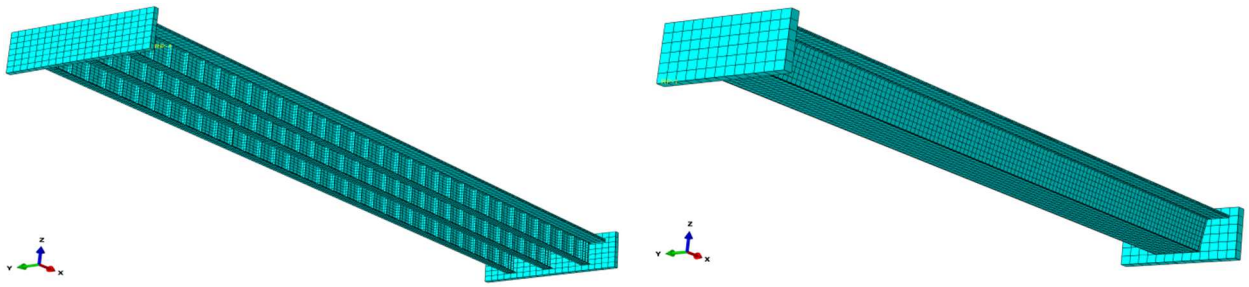

(a) (b)

Figure 5-8: Three dimensional finite element mesh of single lane highway bridge with a) tub girder b) plate girder for structural analysis.

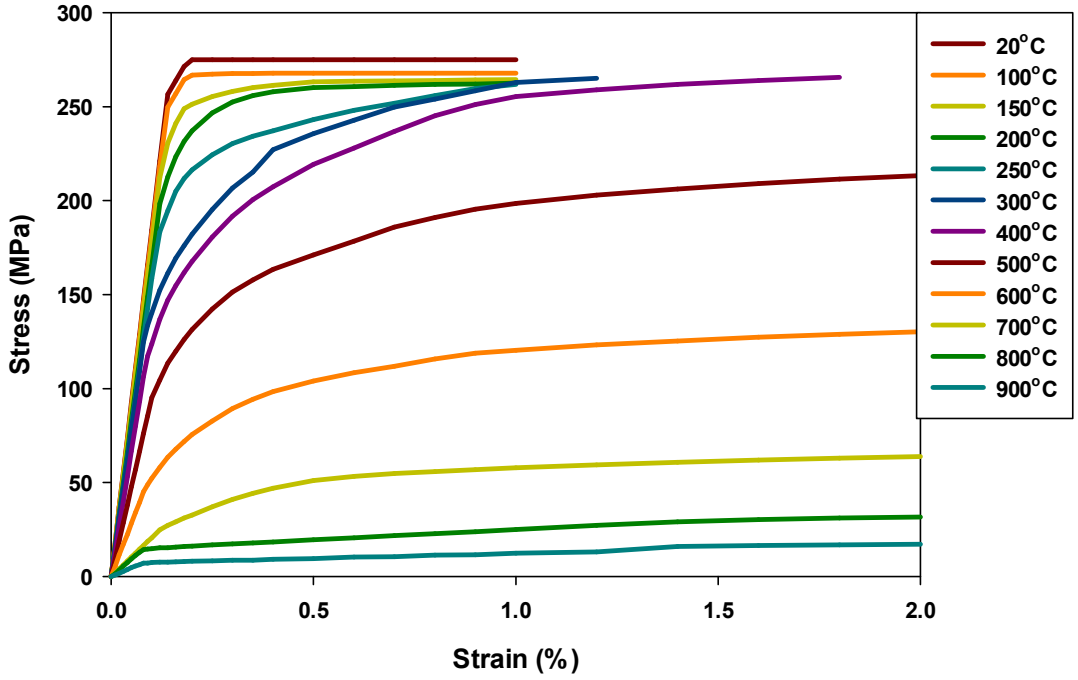

Figure 5-9: Stress-strain relationship for Grade 43A steel as a function of temperature.

The vertical loads on the structure during the fire included the steel girder and concrete deck self-weight; the dead load consisted of the weight of the curbing and rail assemblies and 30% live load according to AASHTO provisions [23]. The self-weight was applied as a gravitational body force. The dead load was estimated to be 22.5 kN/m including the contribution from the tributary area of the concrete slab and the wearing surface of the deck according to AASHTO provisions [23]. For the live load, a uniformly distributed load (9.3 kN/m) representing 0.3 times the load was applied.

In both plate and tub girder bridge model, the cross bracings were not modeled. The effect of cross bracing members were accounted for in the model by restraining the movement of web plate in the transverse direction by setting the displacement in the y-direction, u_y, equal to 0.0. In a similar way, the transverse movement of the concrete slab was restrained to model the effect of restraint due to adjacent spans. To reduce the size of the structural model, the approach and departure span was not included in the model. Their effect was modeled by creating two rigid blocks offset from the bridge at a distance equal to the expansion joint gap (0.072m) from

the outer edge of the girder and deck assembly. The interaction between the steel girder-concrete deck assembly and the rigid blocks were modeled using the Abaqus mechanical contact property option with the normal surface to surface interaction. Due to this, the support ends of the girder were considered as roller to allow freely axial movement until they contacted the rigid blocks. As suggested by Kodur et al. [24], the support end boundary conditions were applied on multiline nodes to reduce the stress concentration.

Table 5-3. Structural properties of steel and concrete with elevated temperature.

	Steel			**Concrete(siliceous aggregates)**	
Temperature (°C)	**Yield strength reduction factor**	**Elastic modulus reduction factor**	**Thermal expansion coefficient**	**Compressive strength reduction factor**	**Thermal expansion coefficient**
20	1.0	1.0	1.2×10^{-5}	1.0	6.19×10^{-6}
100	1.0	1.0	1.25×10^{-5}	1.0	7.49×10^{-6}
200	1.0	0.9	1.29×10^{-5}	0.95	8.67×10^{-6}
300	1.0	0.8	1.33×10^{-5}	0.85	1.01×10^{-5}
400	1.0	0.7	1.37×10^{-5}	0.75	1.18×10^{-5}
500	0.78	0.6	1.41×10^{-5}	0.60	1.39×10^{-5}
600	0.47	0.31	1.45×10^{-5}	0.45	1.63×10^{-5}
700	0.23	0.13	1.49×10^{-5}	0.30	1.62×10^{-5}
800	0.11	0.09	1.41×10^{-5}	0.15	1.44×10^{-5}
900	0.06	0.0675	1.34×10^{-5}	0.08	1.3×10^{-5}
1000	0.04	0.045	1.41×10^{-5}	0.04	1.4×10^{-5}

The structural analysis was completed in two steps. In the first step, the loads consisting of the self-weight, dead loads and live loads were applied to the model. In the second step, the nodal temperature histories generated from the heat transfer analysis were applied. The solution method utilized adaptive damping to aid convergence. Adaptive damping adds small mass proportional forces to aid in numerical convergence when local instabilities are present [25]. The magnitude of the mass was adjusted to ensure that the damping does not affect the global behavior.

5.4 Results

5.4.1 Highway Bridges: Plate Girder Versus Tub Girder

Simulation results are provided in this section and the fire response between tub girder and plate girder single lane highway bridge structures are compared. This was performed to evaluate the effect of girder geometry on the fire response of highway bridges as well as finding a highway bridge design with better fire resistance. The steel girder concrete deck composite assembly was considered to fail when one of the following criteria were met [26]:

i. The vertical mid-span deflection exceeded $L/20$, where L is the span length.
ii. The rate of vertical deflection exceeded $L^2/9000d$.
where, d is the distance from the top of the structural section to the bottom of the design tension surface.
iii. The ultimate strain (ε_{ut} = 20.0% for steel)[34] of the material was exceeded. It was determined by comparing the maximum principal strain of the structure with the ultimate strain of the material.
iv. The von Mises stresses of the element exceeded the material ultimate strength.

5.4.1.1 Fire Dynamics

The effect of girder geometry on the flame dynamics are provided in Figure 5-10. For each simulation case, a plot of the heat release rate per unit volume (HRRPUV) is provided. The HRRPUV plot shows where the fuel burning is occurring and provides a means for visualizing of the flame. In the plots the cutoff value of HRRPUV was set equal to 46 kW/m^3. It was found that the sum of the cells with a HRRPUV value of greater than 46 kW/m^3 represents the volume that includes 95% of prescribed heat release rate.

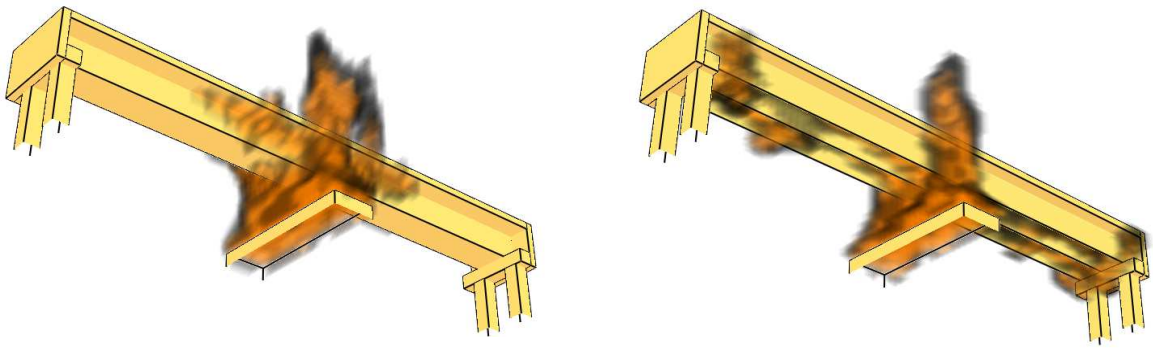

(a) Tub girder (b) Plate girder

Figure 5-10: Flame dynamics of highway bridge structure with a) Tub and b) Plate girder.

As seen in Figure 5-10, the presence of multiple plate girders resulted in the fire scenario where the flames impinge on the concrete deck. After the impingement, the flames were directed toward the ends along the space between the girders and finally flow upward into the ambient after the second impingement into the pier supports. In contrast, the closed box type feature of tub girder resulted in the flames where the majority of the flames impinge and wrap around the bridge with limited flow along the length of the bridge. The difference in flame dynamics caused the steel girder elements to be exposed to different heat flux levels. In the plate girder case, the girder elements were immersed in flames and the heat was transferred from the fire environment to the girder elements from both sides. In contrast, as the interior surfaces of the tub girder were not in contact with the fire environment, only the exterior surfaces were exposed to heat fluxes from the fire environment.

The effect of girder geometry on the transfer of heat from the fire environment to the girder element was further illustrated by comparing the heat to the web of tub and plate girder. Figure 5-11 contains a comparison of the maximum heat flux at mid-span to the web surfaces of plate girder and tub girder. As expected, the web surfaces of plate girders were exposed to same level of heat flux (170 kW/m^2) from both sides. In contrast, only the exterior surfaces of the tub girder web were exposed to heat fluxes (187 kW/m^2) from the fire environment. It is also seen that the predicted heat fluxes to the web of tub girder is 10% higher than those of the of the plate

girders. This is attributed to the more steady behavior of flame dynamics for the case of the tub girder as the flames were less obstructed. However, as seen in Figures 11b and c the high heat flux were confined to the center of the tub girder.

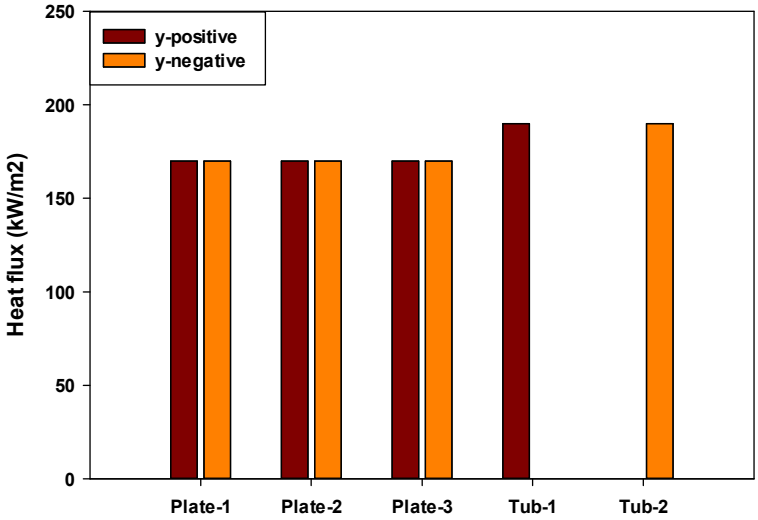

(a)

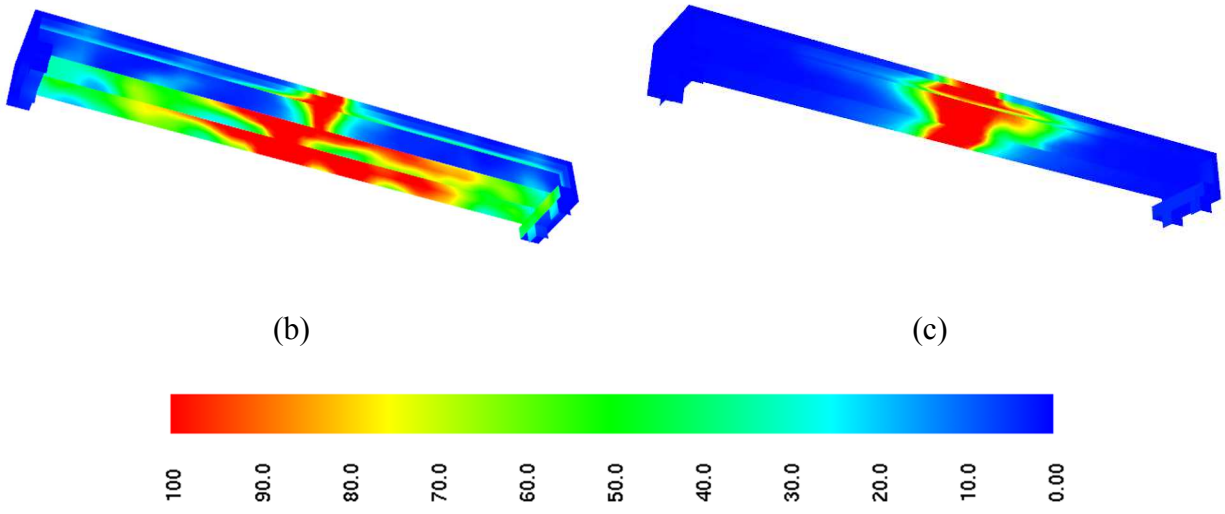

(b) (c)

Figure 5-11: Prediction of the maximum heat flux to the web on a plate and tub girder highway bridge structure.

5.4.1.2 Temperature Response

The influence of girder geometry on the fire response was further evaluated by comparing the element temperature response of plate and tub girders. In order to compare the thermal response, the element temperature averaged over the height at mid-span was plotted as a function of time which is provided in Figure 5-12 and 5-13. Figure 5-12 contains the thermal response prediction for the web of plate girders and tub girder with heavy goods vehicle fire exposure. As seen in Figure 5-12, the web temperature of plate girders 1, 2 and 3 reaches 1026°C, 1052°C and 1004°C; respectively. In contrast, the web temperature of tub girder reaches 887°C which is 19% lower than that of the plate girders. The difference is attributed to the one-sided heating of the web of the tub girder.

Figure 5-13 contains the predictions of bottom flange temperature response averaged over the width with time. Similar to the web thermal response, the bottom flange temperature of the tub girder reaches a value of 867°C. In contrast, the bottom flange temperature of plate girders ranges from 880°C to 1009°C which is 17% higher. As seen in Figure 5-9, at a temperature of greater than 900°C the steel is significantly weakened with no yield strength and the ultimate strength drops to a value of 20 MPa. Figure 5-14 contains a temperature distribution at 1000 s and 1500 s into the fire for the plate and tub girder bridge assembly respectively. The distribution plot shows that tub girder geometry resulted in more localized heating of the bridge elements.

5.4.1.3 Structural Response

A structural analysis was conducted incorporating the element elevated temperatures to compare the response of the plate girder to the tub girder. This included a comparison of the global deflection response as well as the element strain with ultimate strain (ε_{ut}=20%) as recommended by EC3.

The results from structural analysis indicate that the heavy goods vehicle fire exposure resulted in failure of the single lane highway bridge structure with plate girder assembly according to the criteria described in Section 5.4.1. The data obtained from Abaqus have shown that the maximum principal strains at mid-span of the web and bottom flanges exceeded the ultimate strain criterion for the plate girder highway bridge structure. For the tub girder bridge

assembly, the element maximum principal strain does not exceed the 0.2 threshold for the entire duration of the simulation. Figure 5-15 contains the true strain response of the plate and tub girder bridge assembly at simulation durations of 1000s and 1500s, respectively. All strains are scaled to a maximum of 0.2 and the grey region corresponds to the region where the element maximum principal strain exceeds 0.2. It can be seen that for the tub girder, the values of maximum principal element strain were limited to a value of less than 0.1 for the total simulation duration (2400s). In contrast, for the case of plate girders the strain at web exceeds the 0.2 threshold at the mid span of the girder which is in direct contact with the flame. At this location, local buckling is also predicted at the mid span as seen in Figure 5-15.

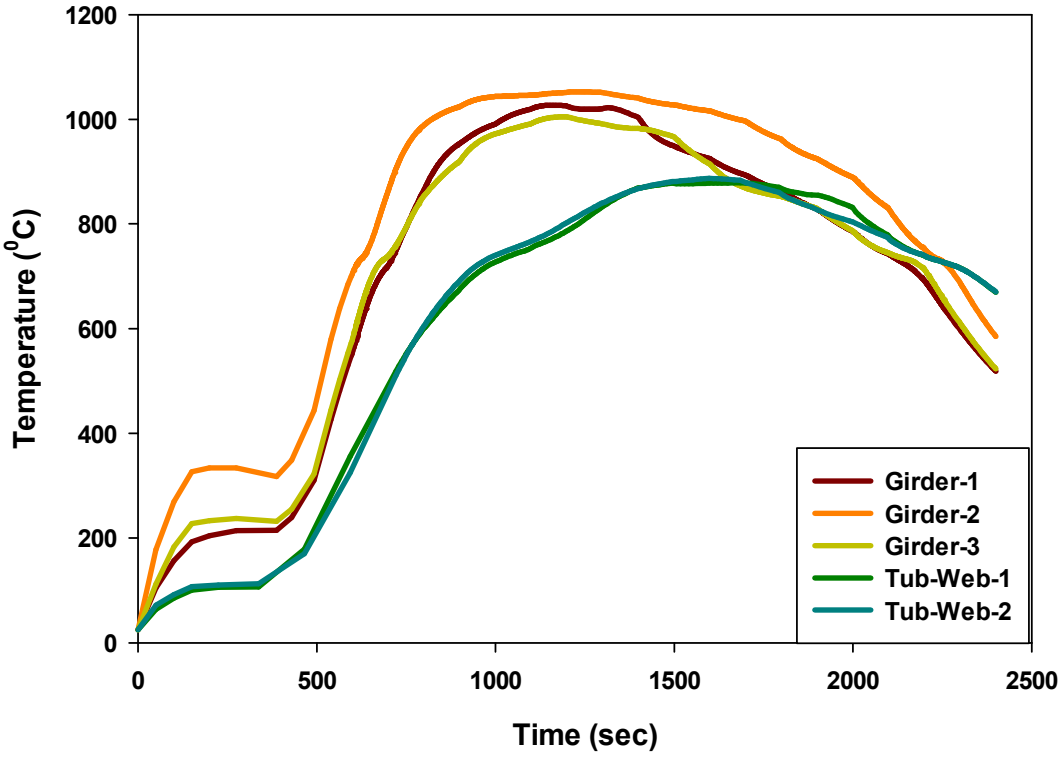

Figure 5-12: Prediction of the web temperature response on a plate and tub girder highway bridge structure.

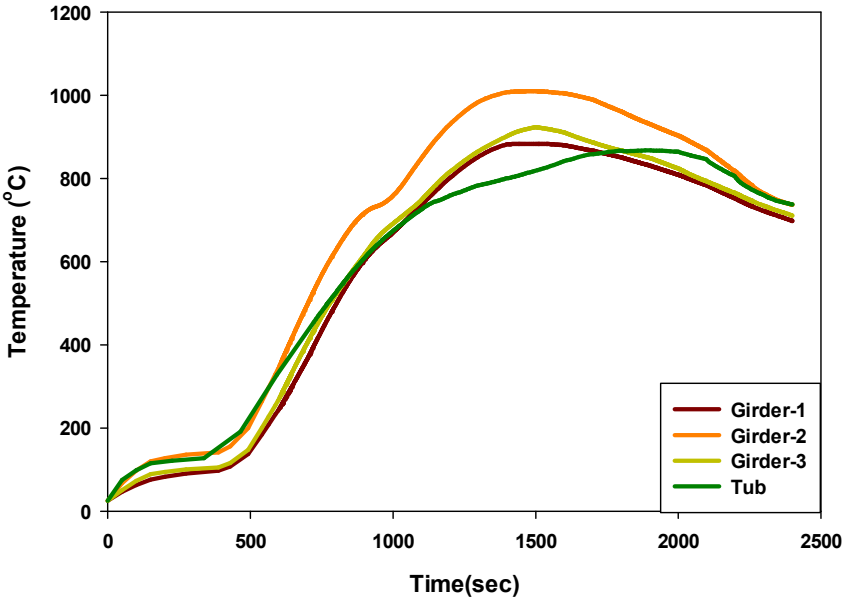

Figure 5-13: Prediction of the bottom flange temperature response on a plate and tub girder highway bridge structure.

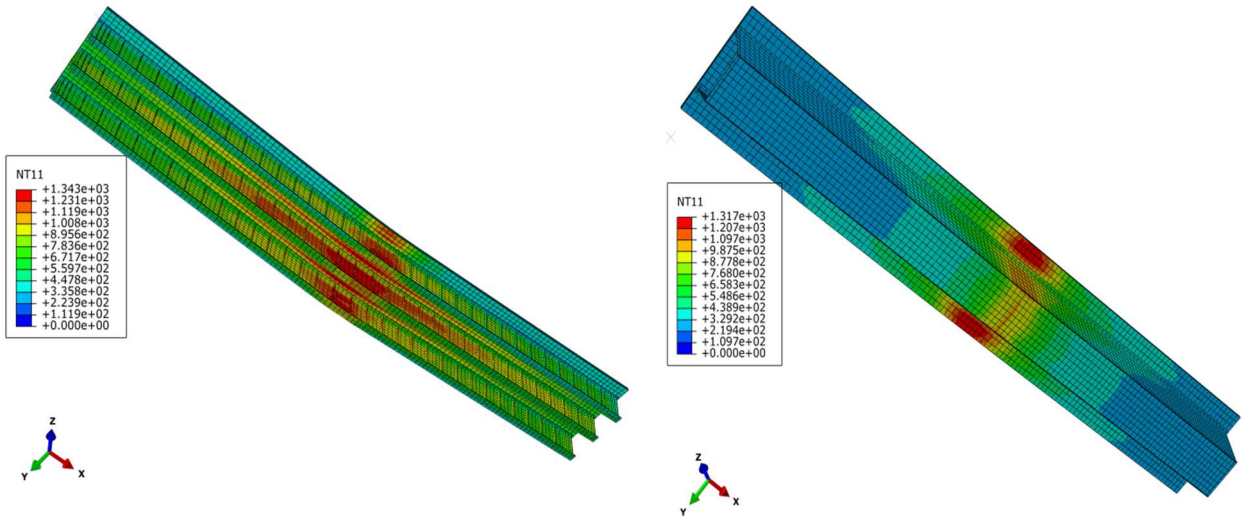

(a) (b)

Figure 5-14: Spatial distribution of temperature along the length of the a) plate and b) tub girder highway bridge structure at a simulation duration of 1000s.

Figure 5-16 contains the mid-span vertical deflection of the single lane bridge assembly with time. The deflections are plotted for the entire duration of the simulation for the tub girder bridge assembly since it did not fail, while the deflections for the plate girder bridge assembly was plotted up to the time of failure. It was seen that for the tub girder bridge the maximum mid-span deflection only reached a value of 0.33 m whereas the plate girder bridge resulted in complete collapse. The localized elevated temperatures produced by the two sided heating caused the strength of the affected region to drop below the point where it can no longer withstand the load. This causes the element to deform excessively under its own weight. Note that the mid-span vertical deflection of tub girder bridge assembly increases upto a simulation duration of 1018s. At this instant of time the tub girder bridge comes in contact with the approach and departure span which exerts an upward bending moment counteracting the increase in downward moment due to the increase in bridge element temperature.

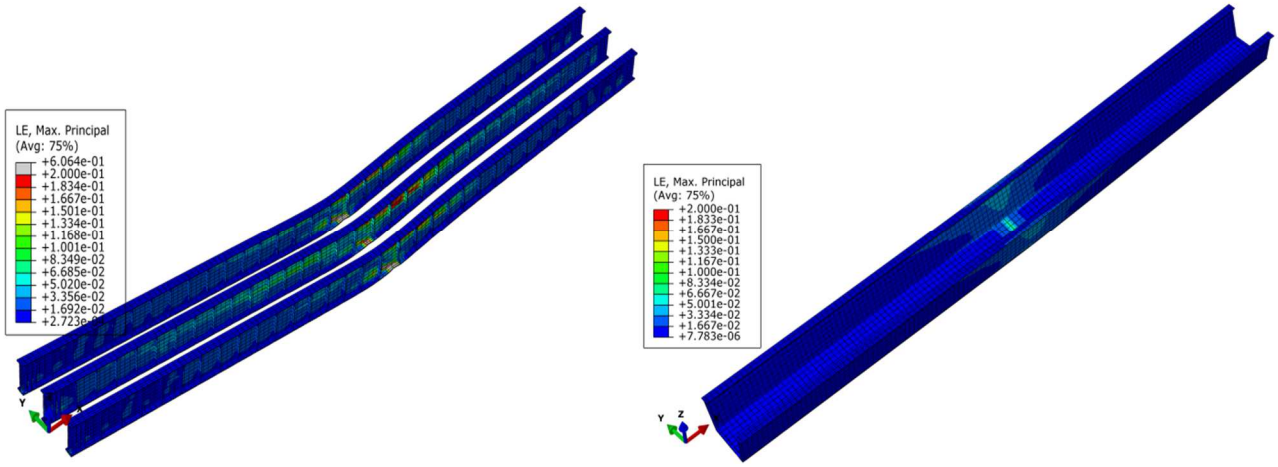

(a) Plate girder (b) Tub girder

Figure 5-15: Strain (maximum principal) contours along the length of the a) plate and b) tub girder highway bridge structure at a simulation duration of 1000s.

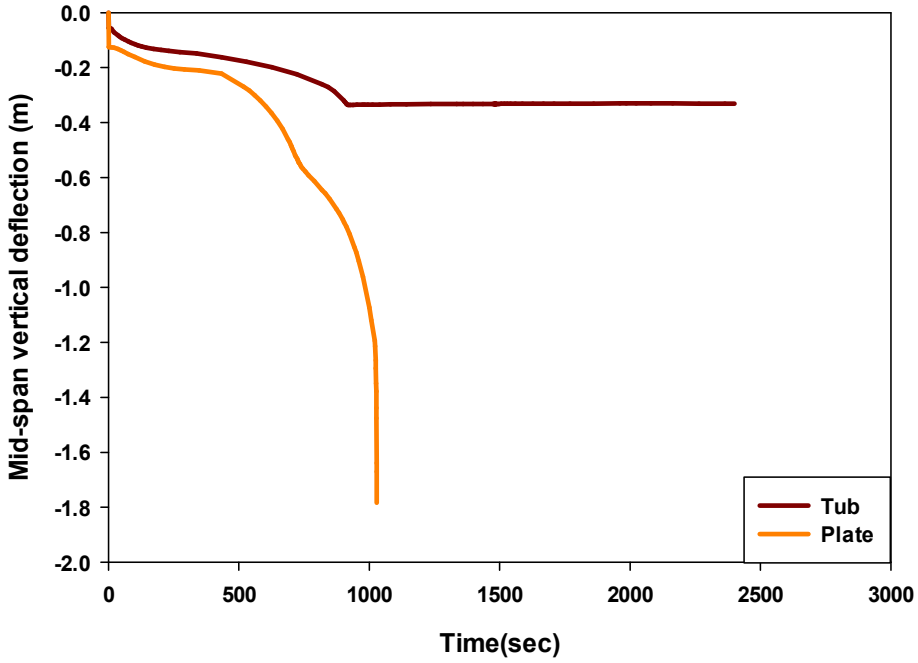

Figure 5-16: Predicted mid-span deflection over time for the steel girder-concrete deck highway bridge structure.

5.4.1.4 Summary

This study has shown that girder geometry affects both the dynamics of the fire as well as the heat transfer to the bridge structural elements which resulted in different fire response. The geometric feature of the plate girders caused the girder elements to be exposed to a high heat load from both sides from the fire environment and failure was predicted to occur at 1000 s into the exposure. Conversely, the closed feature of the tub girder in combination with the higher bending resistance did not resulted in failure from the heavy goods vehicle fire exposure. In the next section, the influence of tub girder geometry was further evaluated by predicting the fire response of a multi-lane highway bridge structure as well as providing additional results on the fire response of a single lane plate girder highway bridge with a flame shield in between the lower flanges.

5.5 Fire Analysis of Highway Bridges with Different Geometry

5.5.1 Plate Girder with Flame Shield

The better structural integrity performance from the tub girder was in part attributed to reducing the surface area heated by the fire environment. In order to minimize the fire exposure for a plate girder bridge, a flame shield made of steel was placed between the bottom flanges of I-section plate girders, as shown in Figure 5-3. The use of a flame shield will prevent the flame from going into the space between the girders and flowing along the bay of the bridge. Instead, it will direct the flame in the axial direction toward the sides of the bridge.

At first, the fire exposure analysis was conducted on the steel plate girder highway bridge structure with flame shield using FDS as described in Section 5.3.2. The presence of the flame shield resulted in the flames that behave as ceiling jet. Some portion of the flame flows outward toward the ends after the impingement at the lower flange of the girder and flame shield. The other portion of the flame flows along the exterior web surface and eventually spills over the sides of the bridge. The most significant impact of using the flame shield is that the interior web surfaces were not in direct contact with the flame. The use of a flame shield resulted in the interior girder web surfaces not being exposed to any heat flux from the fire, but they will experience radiation exchange with adjacent high temperature girders. In order to account for this, a cavity was created in the thermal analysis in Abaqus allowing the radiative interaction between surfaces to occur. Predicted lower flange and web temperatures of plate girders from a heavy goods vehicle fire exposure are provided in Figure 5-17. As seen in Figure 5-17, the lower flange and web temperature rises to a maximum of 870°C and 820°C, respectively, this is 10-20% less than that of the plate girder highway bridge without flame shield.

The influence of the flame shield on the structural response of plate girder highway bridge was also evaluated. Figure 5-18a contains the mid-span vertical deflection of the single lane plate girder bridge assembly with a flame shield with time up to the onset of failure. It can be seen that at exposure duration of 1050s the mid-span vertical deflection of the plate girder assembly increases excessively leading to the ultimate collapse. The structural integrity was further evaluated by comparing the element maximum principal strain with the ultimate strain of steel, ε_u=20% as recommended by EC3. Figure 5-18b contains the strain distribution of the plate girders at 1050s, the time when the highway bridge collapses. The results obtained from Abaqus

indicate that the element maximum principal strain exceeds the ultimate strain criterion after exposure duration of 1050s. Through this analysis, it was determined that the addition of flame shield between the bottom flanges of plate girder is not sufficient to prevent the collapse of the highway bridge structure.

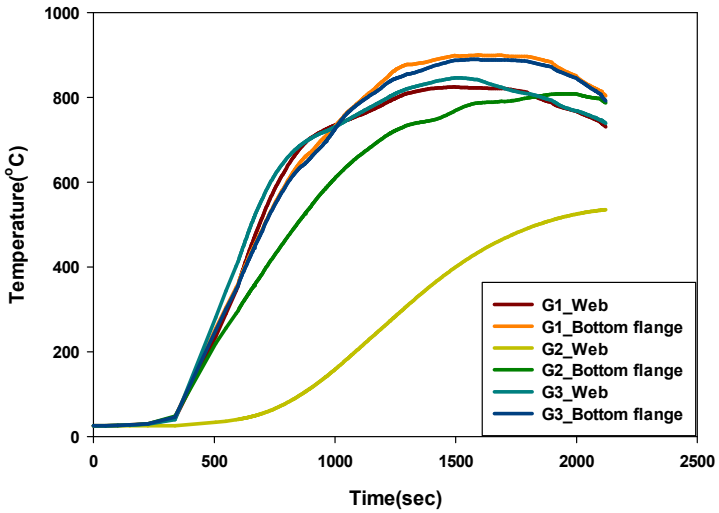

Figure 5-17: Prediction of the element temperature over time for the plate girder highway bridge structure with flame shield.

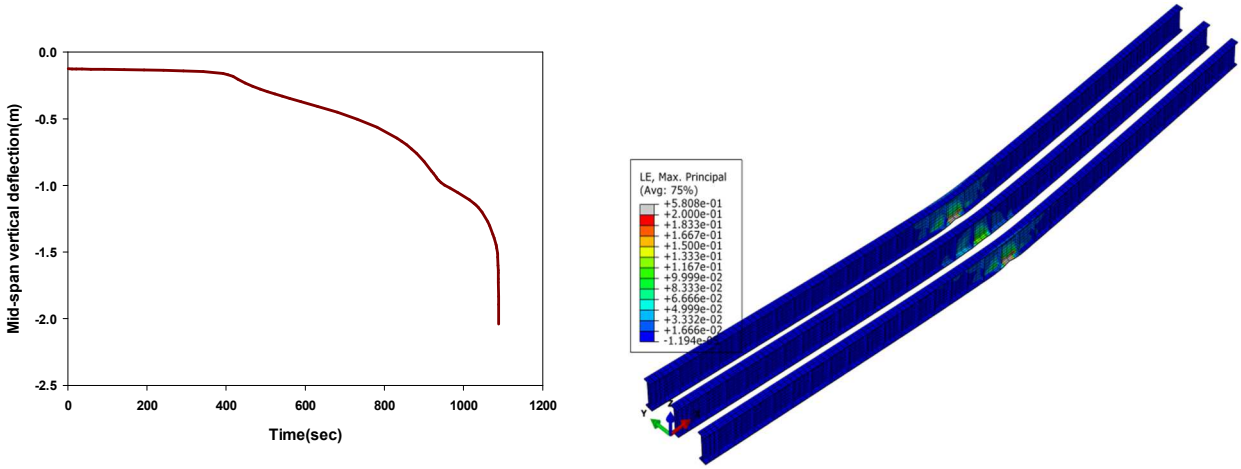

(a) (b)

Figure 5-18: Structural response of a single lane highway bridge with flame shield: a) mid-span vertical deflection and b) logarithmic strain contour at a simulation duration of 1050 s.

5.5.2 Multi Lane Tub Girder Highway Bridge Structure

Highway bridge structures will typically have multiple lanes which requires the use of multiple tub girders. The highway bridge with two or more tub girders includes a bay between adjacent tub girders. This will allow the flame to move freely along the length of the bridge and thus exposing a large area of the highway bridge to a high heat flux. As a result, the fire response of a multi-lane highway bridge consisting of two tub girders with and without flame shield between the lower flanges of the adjacent tub girders was evaluated in this section for the heavy goods vehicle fire exposure. The details of the bridge geometry are provided in Figure 5-3.

The results from the fire analysis illustrates that the presence of multiple tub girders resulted in the flames impinging on the concrete deck between the two tub girders as well as on the bottom flange of the tub girders. After the impingement, the flames were directed along the length of the bridge and impinged onto the pier supports. The continuous flaming in the space between the two tub girders are expected to produce a high heat fluxes onto the web surfaces.

The presence of two tub girders on the thermo-structural response of a multi-lane highway bridge was further evaluated by predicting the tub girder element temperature as well as comparing the element maximum principal strain with the ultimate strain of steel. The thermal and structural analysis simulations were conducted using Abaqus 6.12 as described in Section 5.3.3 and 5.3.4. The thermal model had 62,036 nodes and 8,463 solid elements whereas the structural model had 165,170 nodes and 28,827 solid elements. Different mesh sizes were attempted to choose an appropriate mesh that provides both converged results while minimizing computational time. Predicted lower flange and web temperatures of multi-lane tub girder highway bridges with and without a flame shield from a vehicle fire exposure are provided in Figure 5-19. As seen in Figure 5-19, the interior web temperature reaches a maximum of 920°C as these webs are exposed to a high heat flux from the vehicle fire. The lower flange temperature rises to a maximum of 720°C. As expected, the addition of flame shield between the lower flanges of the tub girders results in interior web temperatures decreasing below 200°C.

The results obtained from Abaqus have shown that the maximum principal strain did not reach the Eurocode recommended ultimate strain failure criteria of 0.2 for the total duration of 2400s for both cases without and with a flame shield. The vertical deflection contours of the

highway bridges are shown in Figure 5-20 after an exposure duration of 1500s. The distribution plot shows that the highway bridge without the flame shield deflects by about 87mm which was reduced to about 0.055 m with the inclusion of the flame shield. The asymmetry of the deflection response is attributed to the asymmetric heating of the bridge girder elements from the fire exposure. Figure 5-21 contains the mid-span vertical deflection response predictions with time for the two cases. It is seen that the highway bridge starts to recover deflection as the fire starts to diminish.

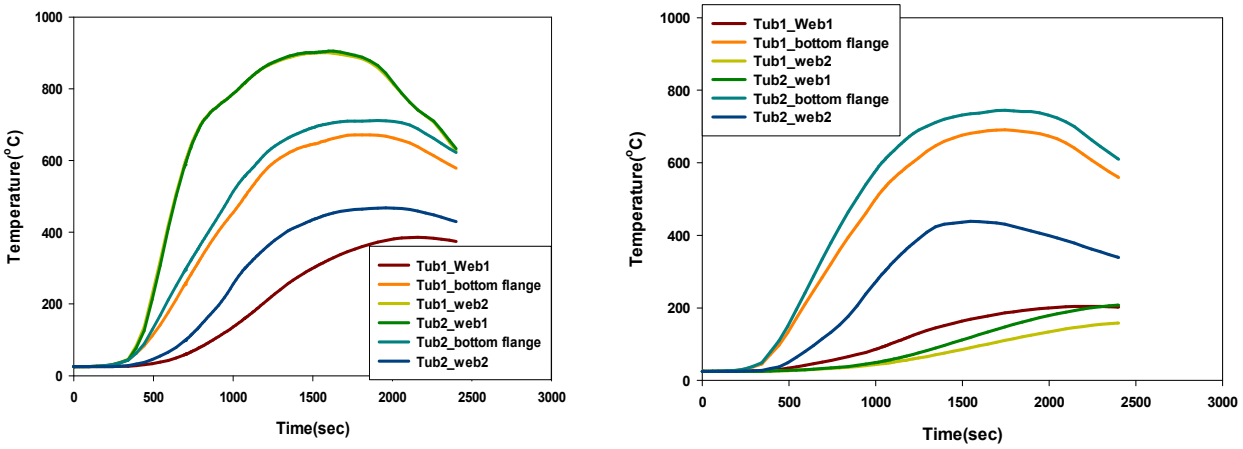

(a) (b)

Figure 5-19: Prediction of the element temperature rise over time for the multi-lane highway bridge structure with two tub girder a) without and b) with flame shield.

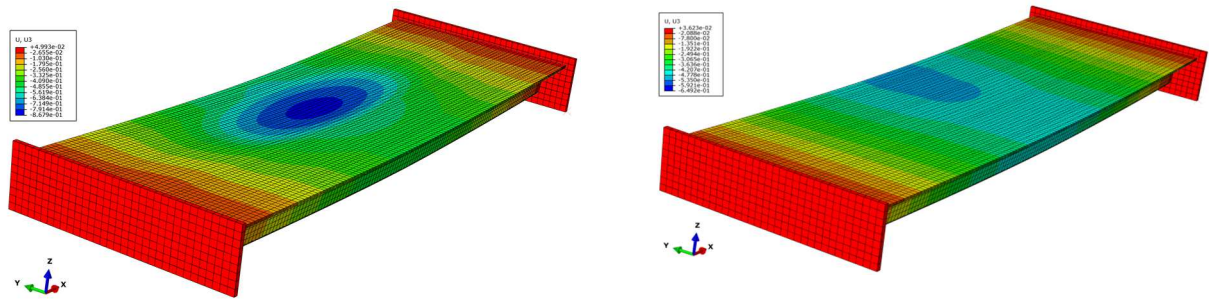

(a) (b)

Figure 5-20: Vertical deflection contours along the length of a multi lane highway bridge structure a) without and b) with flame shield at an exposure duration of 1200s.

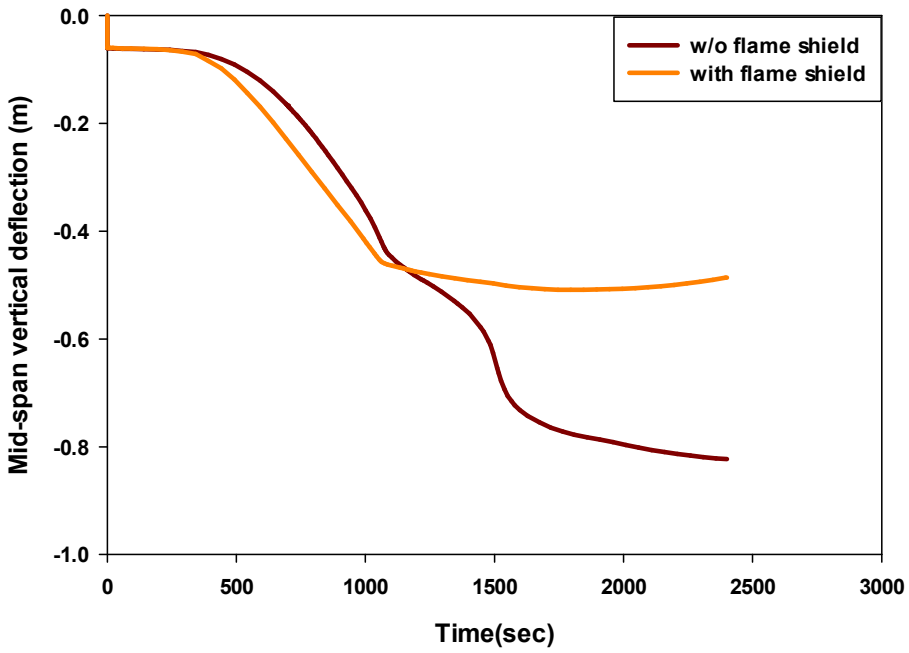

Figure 5-21: Predicted mid-span vertical deflection of a multi-lane highway bridge structure with two steel tub girders.

5.6 Conclusion

A computational study was conducted to determine if steel girders on a bridge could be designed in a way to improve the structural integrity of the bridge during a fire without the need for passive fire protection applied onto the steel surface. Modified bridge girder designs focused on changing the fire dynamics to reduce the thermal exposure onto the girders. This was done by predicting and comparing the fire response of a standard single lane steel girder-concrete deck composite assembly made of three plate girders with bays between girders, a single tub girder, three plate girders with a flame shield, and two tub girders with and without a flame shield. All simulations were performed with a vehicle fire scenario that causes the standard plate girder design to fail. Based on the results, several conclusions were developed from the computational study.

Highway bridges with single and multiple steel tub girders were predicted not to collapse with the heavy goods vehicle fire exposure. However, collapse was predicted for the highway bridges with plate girders.

Placing a flame shield between the lower flanges of adjacent plate girders does not offer any advantage for the fire resistance; the bridge was still predicted to collapse. A flame shield placed between the lower flanges offers some advantage in reducing the internal girder temperature.

The inherent closed box type feature of the tub girder geometry offers advantage in limiting heating the bridge elements from one side and directing the flame outwards the bridge structure. This significantly enhances the fire resistance of highway bridge structure resulting in no collapse following exposure to a heavy goods vehicle fire.

5.7 References

[1] F. P. Bulwa D. (2007, Tanker fire destroys part of MacArthur maze. *2007(29)*.

[2] M. Garlock, I. Paya-Zaforteza, V. Kodur, and L. Gu, "Fire hazard in bridges: Review, assessment and repair strategies," *Engineering Structures,* vol. 35, pp. 89-98, 2012.

[3] N. Y. S. D. o. Transportation. (2008, Bridge fire incidents in New York State (Private Correspondence with Prof M. Garlock). *New York State Department of Transportation*.

[4] Battelle. (2004, Comparative risks of hazardous materials and non-hazardous materials truck shipment accidents/incidents. *Federal Motor Carrier Safety Adminstration*.

[5] N. F. P. A. (NFPA). (2008, NFPA 502 Standard for road tunnels, bridges and other limited access highways. *NFPA*.

[6] E. C. f. S. (CEN). (2002, Eurocode 1 Actions on structures, part 1-2: general actions - actions on structures exposed to fire. *CEN*.

[7] A. Haack, "Fire protection in traffic tunnels: general aspects and results of the EUREKA project," *Tunnelling and Underground Space Technology,* vol. 13, pp. 377-381, 1998.

[8] I. Payá-Zaforteza and M. Garlock, "A numerical investigation on the fire response of a steel girder bridge," *Journal of Constructional Steel Research,* vol. 75, pp. 93-103, 2012.

[9] J. Alos-Moya, I. Paya-Zaforteza, M. Garlock, E. Loma-Ossorio, D. Schiffner, and A. Hospitaler, "Analysis of a bridge failure due to fire using computational fluid dynamics and finite element models," *Engineering Structures,* vol. 68, pp. 96-110, 2014.

[10] J. Glassman and M. Garlock, "High temperatures and bridges: Transverse stiffeners in steel girder fire performance," *Bridge Structures-Assessment, Design & Construction,* vol. 10, pp. 43-52, 2014.

[11] B. Y. Lattimer, C. Mealy, and J. Beitel, "Heat Fluxes and Flame Lengths from Fires Under Ceilings," *Fire Technology,* vol. 49, pp. 269-291, 2013.

[12] P. Hinkley, H. Wraight, and C. Theobald, "The contribution of flames under ceilings to fire spread in compartments," *Fire Safety Journal,* vol. 7, pp. 227-242, 1984.

[13] Y. Hasemi, S. Yokobayashi, T. Wakamatsu, and A. Ptchelintsev, "Firesafety of building components exposed to a localized fire: scope and experiments on ceiling/beam system exposed to a localized fire," *Proceedings of ASIAFLAM,* pp. 351-361, 1995.

[14] H. Ingason and A. Lönnermark, "Heat release rates from heavy goods vehicle trailer fires in tunnels," *Fire Safety Journal,* vol. 40, pp. 646-668, 2005.

[15] K. McGrattan, S. Hostikka, R. McDermott, J. Floyd, C. Weinschenk, and K. Overholt, "Fire dynamics simulator, user's guide," *National Institute of Standards and Technology, Gaithersburg, Maryland, USA, and VTT Technical Research Centre of Finland, Espoo, Finland,* vol. 36, p. 40, 2013.

[16] D. S. Simulia, "Abaqus 6.12 documentation," *Providence, Rhode Island, US,* 2012.

[17] J. W. Deardorff, "Stratocumulus-capped mixed layers derived from a three-dimensional model," *Boundary-Layer Meteorology,* vol. 18, pp. 495-527, 1980.

[18] K. Hiroshi and Y. Taro, "Air entrainment and thermal radiation from heptane pool fires," *Fire Technology,* vol. 24, pp. 33-47, 1988/02/01 1988.

[19] E. C. f. S. (CEN). (2005, Eurocode 3: Design of steel strucutres - part 1-2: general rules - structural fire design. *CEN*.

[20] E. C. f. S. (CEN). (2004, Eurocode 2: Design of concrete structures - part 1-2: general rules - structural fire design. *CEN*.

[21] J. Floyd, G. Forney, S. Hostikka, T. Korhonen, R. McDermott, K. McGrattan, and C. Weinschenk, "Fire Dynamics Simulator Technical Reference Guide-Volume 3: Validation," *NIST Special Publication,* vol. 1019, 2013.

[22] J. R. Howell, R. Siegel, and M. P. Menguc, *Thermal radiation heat transfer*: CRC press, 2011.

[23] L. AASHTO, "Bridge design specifications, customary US units, with 2008 interim revisions," *American Association of State Highway and Transportation Officials, Washington, DC,* 2008.

[24] V. Kodur, E. Aziz, and M. Dwaikat, "Evaluating fire resistance of steel girders in bridges," *Journal of Bridge Engineering,* vol. 18, pp. 633-643, 2012.

[25] X. Dai, Y. Wang, and C. Bailey, "Numerical modelling of structural fire behaviour of restrained steel beam–column assemblies using typical joint types," *Engineering Structures,* vol. 32, pp. 2337-2351, 2010.

[26] D. Wainman and B. Kirby, *Compendium of UK Standard Fire Test Data: Unprotected Structural Steel*: British Steel Corporation, Swinden Laboratories, 1988.

[27] Woodworth M.A. (2013). Fire Hazard Assessment for Highway Bridges with Thermal Mechanical Modeling (Doctoral dissertation, Virginia Polytechnic institute and state university).

[28] Wright W., Lattimer B., Woodworth M., Nahid M., Sotelino E., (2013), NCHRP Project No. 12-85: Highway Bridge Fire Hazard Assessment, Transportation Research Board of the National Academies, Washington, DC (2013)

6 Conclusions and Recommendations

6.1 Conclusions

This thesis presents the fire response of steel girder-concrete deck highway bridge structure with different vehicle and standard fire exposure and girder geometry. Accurate methodologies were created for different fire exposure and these were validated to get accurate results. The fire response study started with a single steel girder concrete deck assembly and continued with full scale highway bridge with plate girders and tub girders. The results provide a better understanding of the behavior of highway bridge with fire exposure. The most important findings are summarized in the following paragraphs.

Furnace exposures with low conductivity furnace linings can be predicted by assigning the standard time-temperature curve to the furnace lining element surface and including heat transfer through radiation exchange between surfaces inside the furnace and convection. In furnaces with low conductivity wall linings containing burners with complete combustion, gas attenuation effects were determined to be small making the radiation exchange between surfaces and convection the dominant modes of heat transfer to the specimen. When implemented into Abaqus, the heat transfer to the specimen and the temperature rise of steel in a floor assembly was predicted to within 10% of experimental data.

Fire environments for hydrocarbon fuel fires with heat release rates of 50kW to 570MW and diameters of 0.3m to 15m can be predicted using FDS by scaling the radiative fraction with fire diameter. The effect of soot formation and oxidation on the gas temperature rise was taken into account varying the radiative fraction with fire diameter. When implemented into FDS, the prediction of gas temperature and velocity as well as heat transfer to objects immersed in flames and ceiling was within 22% of experimental data without the computational expense of models containing detailed soot formation and oxidation.

Steel girder-concrete deck composite assembly highway bridge structures elevated 16m above the road were predicted to not collapse with a vehicle fire such as a bus or a passenger car (heat release rate less than 50 MW) at the mid span of the bridge. However, vehicles such as a box truck or fuel tanker that produce moderate to large heat release rates (100-300 MW) were predicted to cause bridge collapse. Vehicle fires that produce a localized exposure onto the

bridge were determined to cause failure of the highway bridge structure through excessive material softening in the localized heating zone. In contrast, a uniform fire exposure such as a standard furnace exposure was predicted to cause failure of the highway bridge structure through excessive deflection.

The steel girder-concrete deck composite highway bridge structure with single and multiple tub girders were predicted to not collapse with a heavy goods vehicle fire exposure (200MW) due to one sided heating of the bridge elements and higher bending moment capacity of the tub girder. In comparison, a highway bridge structure with plate girders was predicted to collapse with a heavy goods vehicle fire exposure due to exposing both sides of the girders to flames and lower bending moment resistance. The use of a flame shield on an existing plate girder highway bridge to limit the surface area exposed directly to flames was not sufficient to prevent structural collapse due to the radiation exchange between the flame shield and internal surfaces as well as the heat conducted to the beams.

6.2 Recommendations

Based on the findings from this research, the following recommendations are proposed for future research studies.

- More localized fire experiments need to be performed in order to develop benchmark tests for comprehensive models. In particular, experiments are needed to understand the behavior of a loaded steel beam exposed to an open pool fire environment to validate the coupled fire-thermal-structural response. In these experiments, measurements are needed on the girder temperatures, heat fluxes to surfaces, material deflections and strains, and flame locations.
- Highway bridge design steel tub girders should be considered for future bridge construction. Localized fire experiments need to be conducted to validate the unique performance and fire behavior shown in the simulations of highway bridge structures with plate girders and tub girders.
- Further studies should be conducted on the use of flame shields for existing plate girder design bridges for protecting these bridges without applying passive fire protection onto the surface.

- The effects of other bridge geometries and fires need to be further explored in future computational and experimental research studies. This includes bridge elevation above the fire, orientation of the vehicle below the bridge, location of fire on the bridge span, girder cross-section, and girder construction material.
- In this study, the fire response of highway bridges were evaluated through sequentially coupled fire-thermal-structural analysis. Future work is needed to develop a fully coupled fire-thermal-structural model so that the effect of large deflection on the heat transfer to element surfaces can be explored.

Appendix A: Modeling Heat Transfer during Furnace Fire Exposure

[publication information: Nahid, MNH. & Lattimer, B.Y., "Modeling Heat Transfer During Furnace Fire Exposure". ASME IMECE 2012, November 9-15, Houston, Texas, USA]

A.1 Introduction

The fire resistance of a loaded structural member is defined by its response when exposed to a standard fire curve ISO834 [1]. During the evaluation of fire resistance, accurate thermal modeling is critical since the mechanical model will predict the structural response based on the temperature degradation of properties [2]. This signifies the need for an accurate thermal model to predict structure temperatures in a standardized fire resistance test.

Heat transfer from a furnace environment to a test specimen will be due to convection and radiation. The furnace environment is different than an actual fire environment because the heat is being produced using pre-mixed type burners. This results in a clean burning flame with carbon dioxide and water vapor as the major combustion products as well as minimal soot production. If the gas emissivity is not significant, the hot gases inside the furnace will not contribute significantly to the radiation and the radiation will primarily be due to exchange between surfaces inside the furnace. The insulating walls of the furnace will rapidly reach the gas temperatures inside of the furnace. However, test specimens constructed of materials such as concrete and steel have significant thermal inertia, which will cause these surfaces to lag the furnace gas temperatures. Therefore, the furnace walls and specimen surfaces (e.g., concrete and steel) will have different temperatures and will exchange radiation through the participating gas media. As the gas emissivity increases, the participating media will attenuate the radiation and reduce the exchange of radiation.

The net heat transfer to a structural element inside a furnace is

$$q''_{net} = q''_{conv} + q''_{rad} \ldots\ldots\ldots\ldots (1)$$

where the convection is determined by

$$q''_{conv} = h(T_g - T_s) \ldots\ldots\ldots\ldots\ldots (2)$$

A wide range of methods have been used to determine the radiation from the furnace to the structural element. One common method is to use a resultant gas emissivity

$$q''_{rad} = \varepsilon_{res}\sigma(T_g^4 - T_s^4) \ldots\ldots\ldots\ldots\ldots (3)$$

This approach attempts to embody the gas radiation as well as the radiation exchange effects into a single parameter. In Ref. [4], this was determined as

$$\varepsilon_{res} = \frac{1}{\left(\frac{1}{\varepsilon_s}\right) + \left(\frac{1}{\varepsilon_f}\right) - 1} \approx \varepsilon_g \varepsilon_s \ldots\ldots\ldots\ldots\ldots (4)$$

In the majority of the studies, the resultant emissivity was arbitrarily selected to obtain the best predictions of the structural element temperatures [4,5].

Ghojel [3] proposed a heat transfer model to predict the thermal response of a structural member for compartment fires. This model considers the emission and absorption of major constituents of combustion products in the radiative component of heat transfer. According to this model, the radiation through a participating medium is given by Eq. 5.

$$q_r = \sigma\left[\varepsilon_g(T_g + 273)^4 - \alpha_g(T_s + 273)^4\right] \ldots\ldots\ldots (5)$$

Ghojel and Wong [4] modified the model with the incorporation of temperature dependent emissivity. Wong and Ghojel [5] provide an analytical model to calculate the gas emissivity and absorptivity based on a linear regression technique. The calculation of total emissivity of gas is a complex task because of its dependence on the gas temperature, spectral variation, partial pressure of the products of combustion and the thickness of gas layer. The method developed by Ghojel [3] was implemented in the commercial code Abaqus [6] but required the development of special user-subroutines [7]. In these models, they consider the effect of gas only and did not consider radiation exchange between surfaces. Radiation exchange between surfaces is governed by the view factor between surfaces, temperature of these surfaces, and the participating media that the radiation travels through. Radiation exchange between surfaces is known to play an important role in the heating of test specimens. One example of this is the "shadow effect" outlined in the literature [8] to account for radiation exchange between surfaces at lower temperatures than the furnace environment. In addition, Wang [9] proposed an analytical radiation exchange model for the evaluation of the temperature of concave structures. The model is unable to differentiate the temperature experienced by different parts of the concave structure.

In this paper a simple 3D Abaqus model was presented to measure the temperature response of structural member in furnace environments. In the simple 3D Abaqus model the role of gas participating media was not considered. The focus of this paper is to investigate the role of gas participating media on radiation exchange in furnace exposure applications. An analytical model was developed for examining the effect of gas emissivity on the temperature of the enclosure surfaces. Based on these results, a 3D model was generated in Abaqus with the built in cavity radiation option. Results from 3D Abaqus models were compared with existing furnace exposure data on concrete floor sections with a steel support I-beam on the exposed side of the concrete.

A.2 Modeling Approach

In this section an analytical model was developed to investigate the effect of participating media on the surface temperature of a simple enclosure consisting of three surfaces. Details are provided on the Abaqus 3D model used to predict the temperature of structural elements subjected to the standard fire condition.

A.2.1 Radiative Heat Transfer Model

The simple triangular geometry shown in Fig. 1 was developed to study the effect of gas emissivity on the enclosure surface temperature. In this geometry, the steel and concrete surfaces represent the structural member whereas the insulation surface represents the furnace walls. The isothermal gas inside the enclosure is a participating media that can attenuate the radiation exchange between the surfaces. Scattering by the participating media was not considered.

The net heat flux at each surface of the enclosure bounding an isothermal medium of gas is given by the balance between the outgoing flux, composed of emitted and reflected energy from the surface, and the incoming flux resulting from the radiation contribution of all the surfaces and the gas medium.

$$q_k A_k = (q_{o,k} - q_{i,k}) A_k \ldots\ldots\ldots\ldots\ldots (6)$$

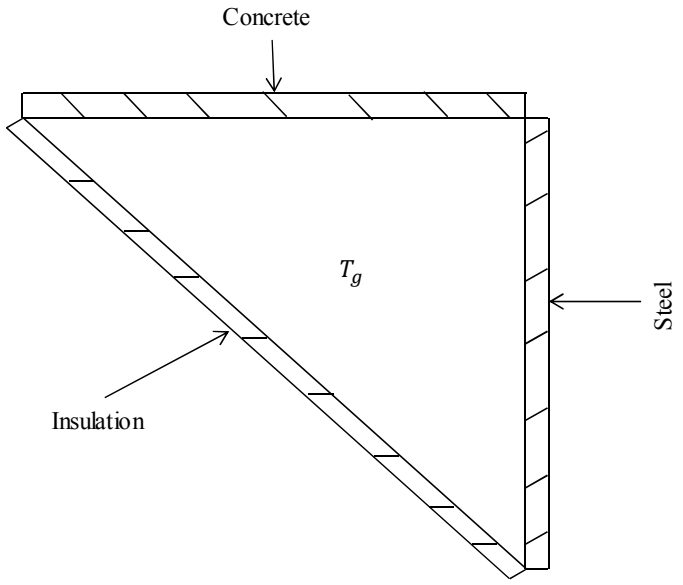

Figure A- 1:Schematic view of three surface enclosure.

For an enclosure consisting of N surfaces bounding a well-mixed gas at uniform temperature T_g, the energy transfer between surfaces is given by Eq. 7 [10].

$$\sum_{j=1}^{N}\left(\frac{\delta_{kj}}{\varepsilon_j}-F_{k-j}\frac{1-\varepsilon_j}{\varepsilon_j}\tau_{k-j}\right)q_j=\sum_{j=1}^{N}[(\delta_{kj}-F_{k-j}\tau_{k-j})e_{b,j}-F_{k-j}\alpha_{k-j}e_{b,j}]\ldots\ldots\ldots\ldots\ldots\ldots(7)$$

Applying Eq. 7 to the simple enclosure in Fig. 1 yields the following equations

for steel,

$$\frac{1}{\varepsilon_s}q_s-F_{s-c}\frac{1-\varepsilon_c}{\varepsilon_c}\tau_{s-c}q_c-F_{s-f}\frac{1-\varepsilon_f}{\varepsilon_f}\tau_{s-f}q_f = e_{b,s}-F_{s-c}\tau_{s-c}e_{b,c}-F_{s-f}\tau_{s-f}e_{b,f}-F_{s-c}\alpha_{s-c}e_{b,g}-F_{s-f}\alpha_{s-f}e_{b,f}\ldots\ldots(8)$$

for concrete,

$$\frac{1}{\varepsilon_c}q_c-F_{c-s}\frac{1-\varepsilon_s}{\varepsilon_s}\tau_{c-s}q_s-F_{c-f}\frac{1-\varepsilon_f}{\varepsilon_f}\tau_{c-f}q_f = e_{b,c}-F_{c-s}\tau_{c-s}e_{b,s}-F_{c-f}\tau_{c-f}e_{b,f}-F_{c-s}\alpha_{c-s}e_{b,g}-F_{c-f}\alpha_{c-f}e_{b,f}\ldots\ldots(9)$$

and for the furnace insulation,

$$\frac{1}{\varepsilon_f}q_f-F_{f-c}\frac{1-\varepsilon_c}{\varepsilon_c}\tau_{f-c}q_c-F_{f-s}\frac{1-\varepsilon_s}{\varepsilon_s}\tau_{f-s}q_s = e_{b,f}-F_{f-c}\tau_{f-c}e_{b,c}-F_{f-s}\tau_{f-s}e_{b,s}-F_{f-c}\alpha_{f-c}e_{b,g}-F_{f-s}\alpha_{f-s}e_{b,s}\ldots\ldots(10)$$

The transmissivities in Eqs. 8-10 are equal to one another and were determined by

$$\tau_g = 1 - \varepsilon_g \ldots\ldots\ldots\ldots\ldots\ldots (11)$$

The simple triangular geometry is infinitely long and the view factor between steel and concrete which are perpendicular to one another was calculated by [10]

$$F_{c-s} = \frac{w_c + w_s - w_f}{2w_c} \ldots\ldots\ldots\ldots\ldots (12)$$

And

$$A_c F_{c-s} = A_s F_{s-c} \ldots\ldots\ldots\ldots\ldots\ldots\ldots (13)$$

The view factor between concrete and insulation surface was calculated by

$$F_{c-f} = 1 - F_{c-s} \ldots\ldots\ldots\ldots\ldots\ldots\ldots (14)$$

The analysis considered sufficiently thin steel such that a lumped capacitance approach was appropriate. To be consistent with the actual scenario the half of thickness of steel was considered in the analytical model. As a result, the outer surface of the steel was assumed insulated and the temperature of the steel was found by

$$\Delta T = \frac{q_s A_s \Delta t}{\rho_s V_s c_{p,s}} \ldots\ldots\ldots (15)$$

The full thickness of the concrete slab was considered in the analytical model. Since the thickness of the concrete is sufficiently high and the conductivity is low, a temperature gradient will exist through the thickness of the concrete slab. As a result, a finite difference discretization approach was applied as shown in Figure 2 to predict the temperature of the concrete. The furnace exposure is at edge cell j and the unexposed surface of the concrete is at edge cell jj.

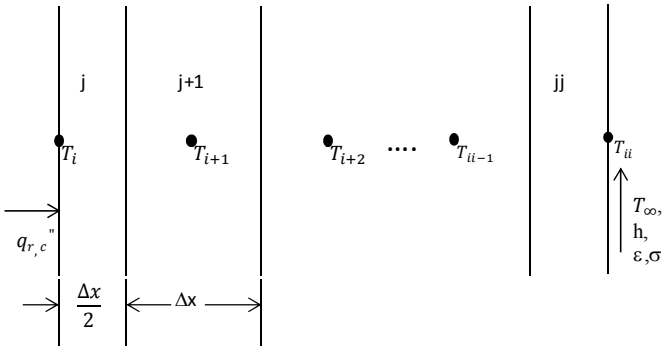

Figure A- 2:Finite difference grid for concrete slab.

Using an energy balance on each cell

$$E_{in} + E_g = E_{st} \ldots\ldots\ldots\ldots (16)$$

the discretization equations were developed. For the cells on the edges and interior of the concrete, the energy balance equation results in the following equations :

For exposed edge cell (j):

$$q_r^{"}A_c - \frac{k_c A_c}{\Delta x}\left(T_i^p - T_{i+1}^p\right) = \rho_c c_{p,c} A_c \frac{\Delta x}{2}\left(\frac{T_i^{p+1} - T_i^p}{\Delta t}\right) \ldots\ldots (17)$$

For interior cells (j+1) to (jj-1)

$$\frac{k_c A_c}{\Delta x}\left(T_i^p - T_{i+1}^p\right) - \frac{k_c A_c}{\Delta x}\left(T_{i+1}^p - T_{i+2}^p\right) = \rho_c c_{p,c} A_c \frac{\Delta x}{2}\left(\frac{T_{i+1}^{p+1} - T_{i+1}^p}{\Delta t}\right) \ldots\ldots (18)$$

For unexposed edge cell (jj):

$$\frac{k_c A_c}{\Delta x}\left(T_{ii}^p - T_{ii-1}^p\right) - hA_c\left(T_{ii}^p - T_\infty\right) - \epsilon\sigma A_c\left(T_{ii}^{p^4} - T_\infty^4\right) = \rho_c c_{p,c} A_c \frac{\Delta x}{2}\left(\frac{T_{ii}^{p+1} - T_{ii-1}^p}{\Delta t}\right) \ldots\ldots (19)$$

A temperature lag exists for about 5 to 10 minutes between the temperature of the furnace wall and the standard ISO-834 curve [11]. After this initial lag, the temperature of the furnace wall follows the ISO-834 curve. For this simple analytical model, the initial lag was neglected and the temperature of the furnace wall was assigned as the temperature of the gas which follows the Standard ISO-834 curve.

Prior to a simulation, inputs were provided on the widths of the steel and concrete as well as the gas emissivity. The insulation exposed surface temperature and the gas temperature were both set to the ISO 834 time-temperature curve. The model was then used to predict the temperature rise of the steel and the concrete with time.

A.2.2 Abaqus Model

A 3D Abaqus model was generated to determine the temperature response of a structural member in the furnace fire tests conducted by Wainman and Kirby [12]. The furnace tests performed by Wainman and Kirby [12] were conducted in general accordance with ISO 834. A series of experiments were performed on concrete slabs with a supporting steel I-beam on the fire side of the concrete. Tests performed in the experimental study included a range of I-beam sizes, composite and non-composites systems, and various boundary conditions.

The furnace was 3m wide, 4.53m high and 2m deep and lined with high temperature refractory insulation. Gas temperature inside the furnace was measured using standard thermocouples.

Using natural gas powered burners; the furnace gas temperature was controlled to follow the ISO 834 time-temperature curve within the acceptable tolerance. Except for the initial 5-10 minutes, the gas temperature inside the furnace will be equal to that measured using the furnace thermocouples. [11] With the exposure duration 25–40 minutes, the gas temperature in the furnace was taken to be equal to the ISO 834 time-temperature curve in the simulations.

A three-dimensional thermal analysis was performed in Abaqus to determine the temperature rise of the concrete and steel I-beam during the ISO 834 furnace exposure. As previously described, the furnace exposure onto the sample is composed of both convection and radiation. The furnace exposure was modeled in Abaqus using the built-in radiation exchange model and an applied convective heat transfer interaction. The convection heat transfer coefficient on the inside of the furnace was 25 W/m^2-K as recommended in the Eurocode [8]. To do the radiation exchange within Abaqus, the walls of the furnace were included in the model as shown in Figure 3. Since the furnace walls were well insulated, the furnace wall temperatures were set equal to the ISO 834 furnace gas temperature. Three-dimensional heat transfer was performed on the concrete on top of the furnace as well as the I-beam mounted below the concrete. On the unexposed side of the concrete, the concrete radiated to the laboratory surroundings and was cooled through convection with the ambient temperature gas at 298K and a convective heat transfer coefficient of 25 W/m^2-K. It was found that the effect of the value of convective heat transfer coefficient on the temperature rise of the structural member is insignificant (1-2%).

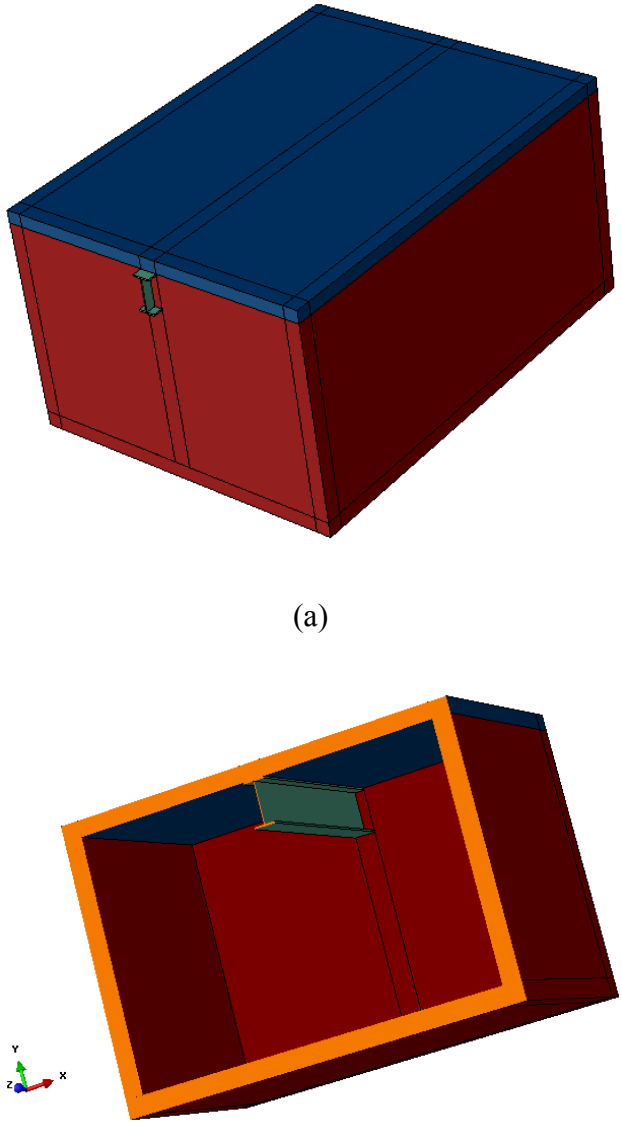

(a)

(b)

Figure A- 3:An a) exterior view and b) interior view of the Abaqus model of the Wainman and Kirby [12] furnace tests.

The thermal analysis was performed using quadratic solid elements, (DC3D20). In the model, thermal resistance between contact surfaces was not considered and the surfaces in thermal contact were forced to have the same temperature using TIE constraints. Temperature dependent thermal conductivity, specific heat for all surfaces for the steel and concrete materials were taken from according to Eurocode [13, 14]. The furnace walls were taken to be insulated

with properties of a typical furnace insulation material [15]. The value of emissivity for concrete, steel and furnace walls were 0.94, 0.9 and 0.9; respectively [10].

A.3 Results and Discussion

The simple three sided enclosure radiation model was used to investigate the effects of gas participating media on the steel and concrete surface temperatures. Based on these results, simulations were performed using the Abaqus 3D model and compared with the test results.

A.3.1 Radiative Heat Transfer Model

The simple enclosure model shown in Fig. 1 was used to quantify the effects of gas attenuation on the temperature rise of steel and concrete. To provide a range of emissivities that are expected in the furnace test, the emissivity of the participating media for the case of furnace fire condition was calculated. As discussed earlier, there is sufficient mixing in furnace environment and the entire gas is isothermal and of uniform composition. Due to the complete combustion from the furnace burners, CO_2 and H_2O are two major gases within the furnace. The emission from the gas mixture was determined by [10]

$$\varepsilon_g = C_{CO_2}\varepsilon_{CO_2} + C_{H_20}\varepsilon_{H_2O} - \Delta\varepsilon \dots\dots\dots\dots (20)$$

The first two terms are the emission contributions of CO_2 and H_2O while $\Delta\varepsilon$ accounts for the reduction in the emittance due to the spectral overlap of the CO_2 and H_2O absorption bands. Using Eq. 20 and charts provided by Siegel and Howell [10], the emissivity of gas was calculated for various percentages of stoichiometric of air since the burners typically operate with excess air of as much as 400%.The calculation was carried out at a pressure of 1 atm. The results are given in Table 5-1. The mean beam length of the participating medium which was isothermal and radiating to its entire boundary was calculated by [10]

$$L_e \approx 0.9\, L_{e,o} \approx 0.9\, \frac{4V}{A} \dots\dots\dots\dots (21)$$

The maximum gas temperature was assumed 1150 K. Based on these results, it was determined that the value of gas emissivity in furnace environment is less than 0.3.

Table A- 1:Calculation of gas emissivity

% of air of stoichiometric ratio	100%	200%	300%	400%
Emissivity of gas, ε_g	0.233	0.159	0.127	0.116

The effect of gas emissivity on the surface temperature of an enclosure was examined using the analytical method previously developed. In the analytical model for the simple geometry shown in Fig 1 the temperature of the furnace wall and the gas medium were assigned the temperature of the standard ISO-834 curve [1]. The model then determined the temperature rise of the steel and concrete for different gas emissivity. The effects of steel and concrete width ratio were also examined.

The time-temperature history of steel and concrete surface is plotted in Fig 4. In these plots the steel to concrete width ratio was 0.1. In actual scenarios, the steel to concrete width ratio is typically less than 1.0. For comparison purposes, the time-temperature history of ISO-834 curve is also plotted in the figures. From the results of Fig 4, it is seen that the time temperature history for both steel and concrete surfaces are lowest with a gas emissivity of 0.0. The value of gas emissivity of 0.0 indicates that the participating media is purely non-absorbing, non-attenuating and transparent. The lower value of temperature of the steel surface demonstrates the presence of a relatively cool concrete surface. In addition, both surfaces have lower temperatures because the gas does not radiate to the surfaces, only the insulated surface. The results also demonstrate that the temperature of both surfaces increase with an increase in gas emissivity. The higher value of gas emissivity indicates the participating media obstructs the geometric exchange between surfaces and temperature rise is driven by the gas. From the results it is also seen that the difference in temperature for both steel and concrete surface are within 3% for gas emissivity values ranging from 0.0 to 0.3.

The effect of the steel to concrete width ratio is shown in Fig. 5 and Fig. 6. In Fig. 5, the temperature rise in steel is provided for steel to concrete width ratios of 0.1, 1.0 and 10 with gas emissivity ranging from 0.0 to 0.3. In Fig. 6, the temperature rise of the steel and concrete is provided for a range of width ratios with the gas emissivity at 0.0. The value of gas emissivity of

0.0 represents that the participating medium is non-absorbing and transparent. As a result the participating medium will have no effect on the temperature rise of steel and concrete. This will allow us to investigate the effect of radiation exchange between surfaces on the temperature rise.

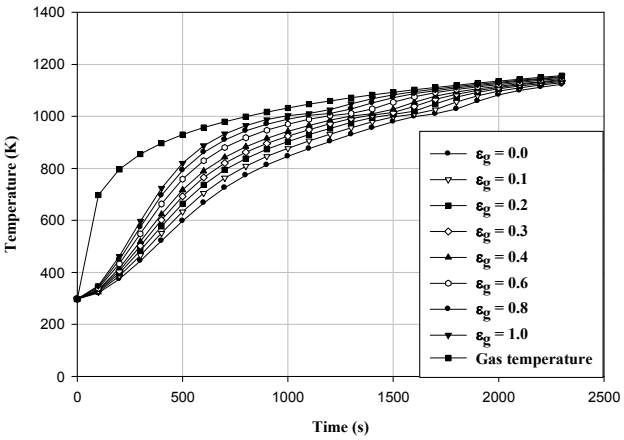

(a)

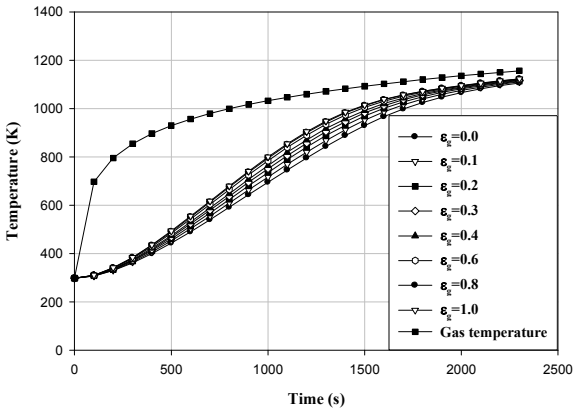

(b)

Figure A- 4:Temperature response of a) steel and b) concrete for different values of gas emissivity with steel to concrete ratio of 0.1.

From the results in Fig. 5, effect of gas emissivity on the temperature rise increases with increase in width ratio. At a width ratio of 0.1 the difference is 3% while at a width ratio of 10 the difference is 10%. As previously mentioned, width ratios of less than 1.0 are common (i.e.,

concrete width much higher than steel width). Therefore, a small error is expected in assuming no gas participating media effects in furnace exposures. The results in Fig. 6 demonstrate the fact that the width of concrete has a significant effect (20% for the cases considered) on the temperature rise of steel with no gas emissivity. This highlights the fact that changes in the geometry of a steel I-beam relative to the size of concrete can have an impact on the radiation exchange with no gas emission effects.

The results of the analytical model indicate that participating gas media will have less than a 10% effect on the predicted temperature of the specimen in an environment produced by furnace burners. In compartment fires where the mixing is not complete and the burning of specimen produces a lot of smoke, the production of smoke increases the emissivity of the participating media and the effect can no longer be neglected. For noncombustible specimens exposed to furnace conditions, the radiation exchange between surfaces is the main factor to consider.

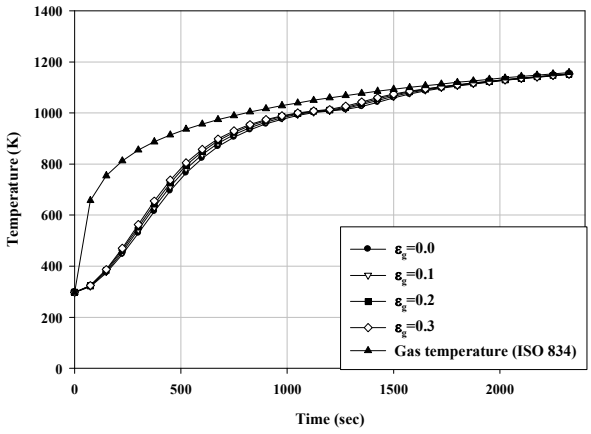

(a)

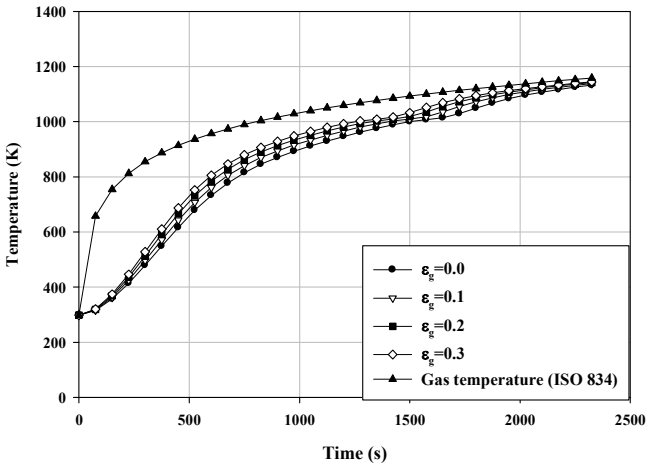

(b)

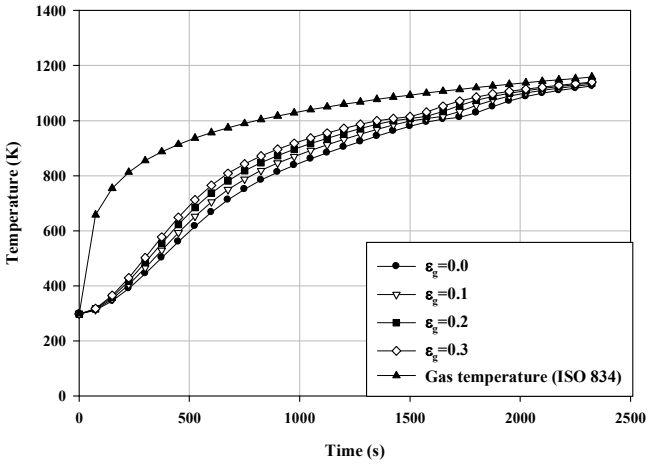

(c)

Figure A- 5:Temperature response of steel for different values of gas emissivity with steel to concrete width ratios of a) 0.1, b) 1.0, and c) 10.0.

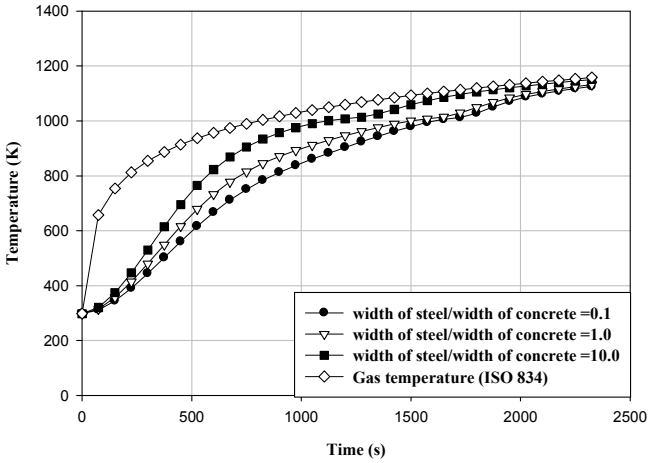

Figure A- 6:The temperature rise of steel for different steel to concrete width ratio with gas emissivity values of 0.0.

A.3.2 ABAQUS Model

The Abaqus 3D model was used to simulate the temperature rise of steel I-beams below a concrete slab. Wainman and Kirby [12] measured temperatures on the lower flange, the web, and the upper flange of a steel beam mounted below a concrete slab during their furnace experiments. In total, they performed 31 tests on beams with various section factors. For each section factor, they performed more than one experiment. In this validation study, tests with steel beam sections of 254x146 and 305x165 were selected to evaluate the ability of the model to predict the thermal response. Details of the steel beams and concrete slab are provided in Table 2.

Table A- 2:Simulation matrix for Abaqus 3D model.

Section serial size (mm)	**Width of section (mm)**	**Depth of section (mm)**	**Thickness**		**Section factor**
			Web	**Flange**	
254 X 146	147.3	259.6	7.3	12.7	196
305 X 165	165.7	307.1	6.7	11.8	212

The final temperature distribution inside the furnace is provided in Figure 7 for the 254x146 beam. The figure clearly shows the distinct difference in temperatures between the concrete slab on top of the furnace, the steel I-beam beneath the concrete, and the furnace walls. In addition, note the temperature variation along the height of the I-beam and the through the thickness of the concrete slab. In the mechanical response, these temperature variations will produce thermally induced moments that will cause bending in the test article.

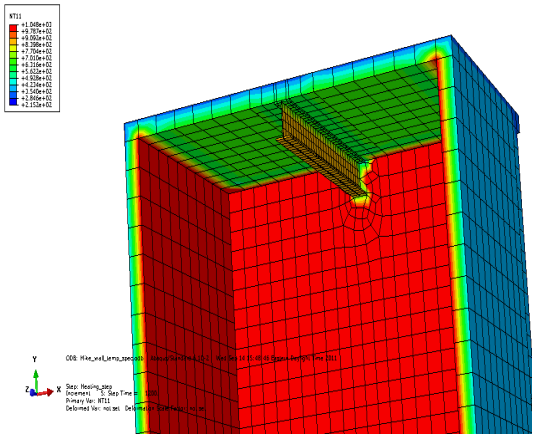

Figure A- 7:Temperature contour of the furnace walls along with the steel I-beam mounted below the concrete slab on top of the furnace.

Fig. 8 and Fig. 9 provide a comparison of the experimentally measured temperatures with the temperatures predicted using the Abaqus model. From a comparison of the temperature rise of the same beam in multiple tests, the temperature response of different parts of the beam varies by 30% from test to test for a single beam type. As a result, the Abaqus simulation results were compared with the upper and lower bound of temperatures of different parts of the beam to determine the accuracy of the modeling. The predicted temperatures agree well with the bounds in the experimental data. All predicted temperatures fall within the band including the lower and upper bound of experimentally measured data except for the case shown in Fig 9b. For the 305 x 165 beam, only two tests were reported while there were 14 tests performed on the 254 x 146

beam. Based on the error estimate from the 254 x 146 beam test, the test repeatability error is 30%. The simulated temperature falls within the error band of 30%.

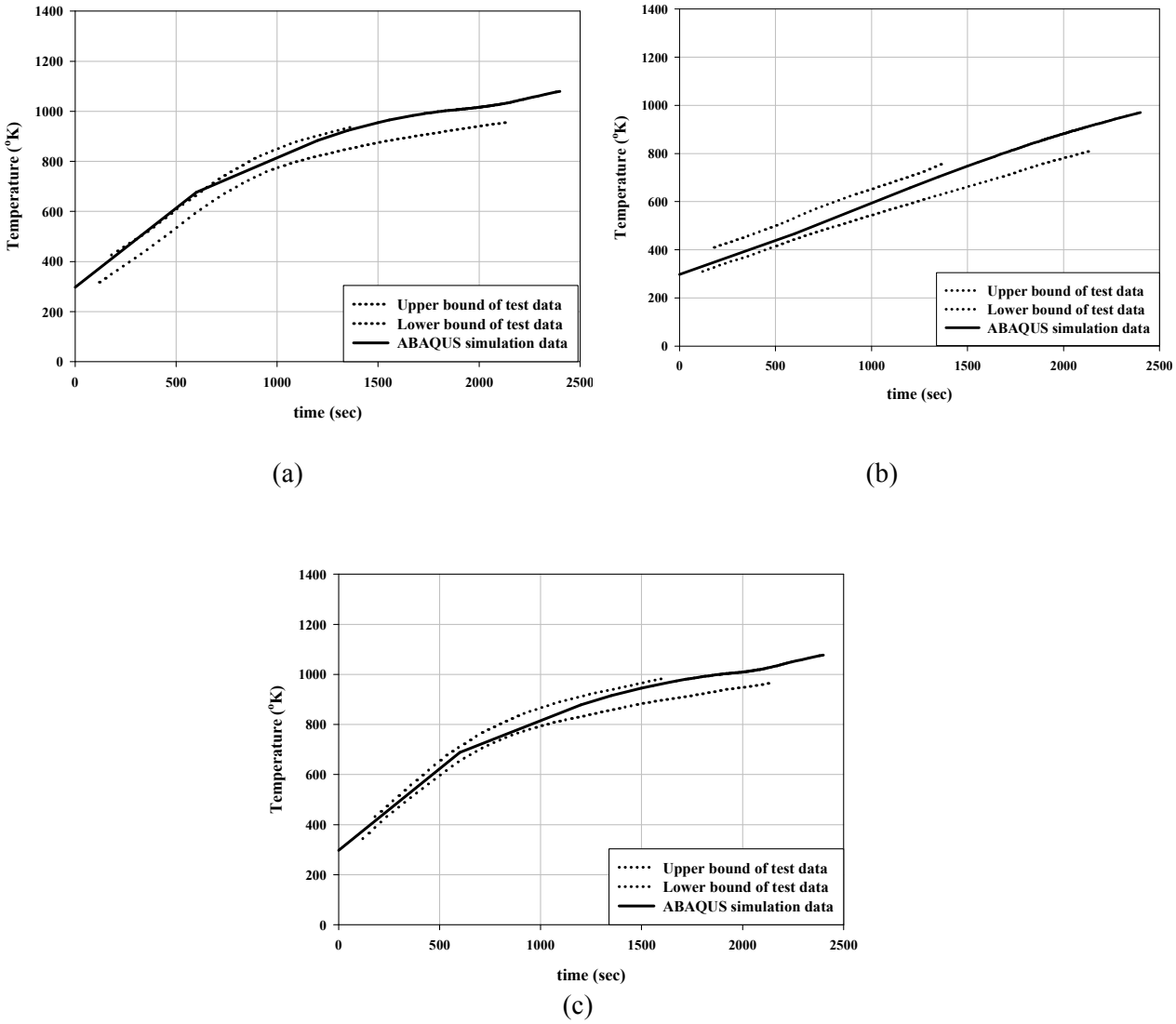

Figure A- 8:Predicted and measured temperature response of the 254 x 146 steel beam a) lower flange, b) upper flange, and c) web when mounted below concrete.

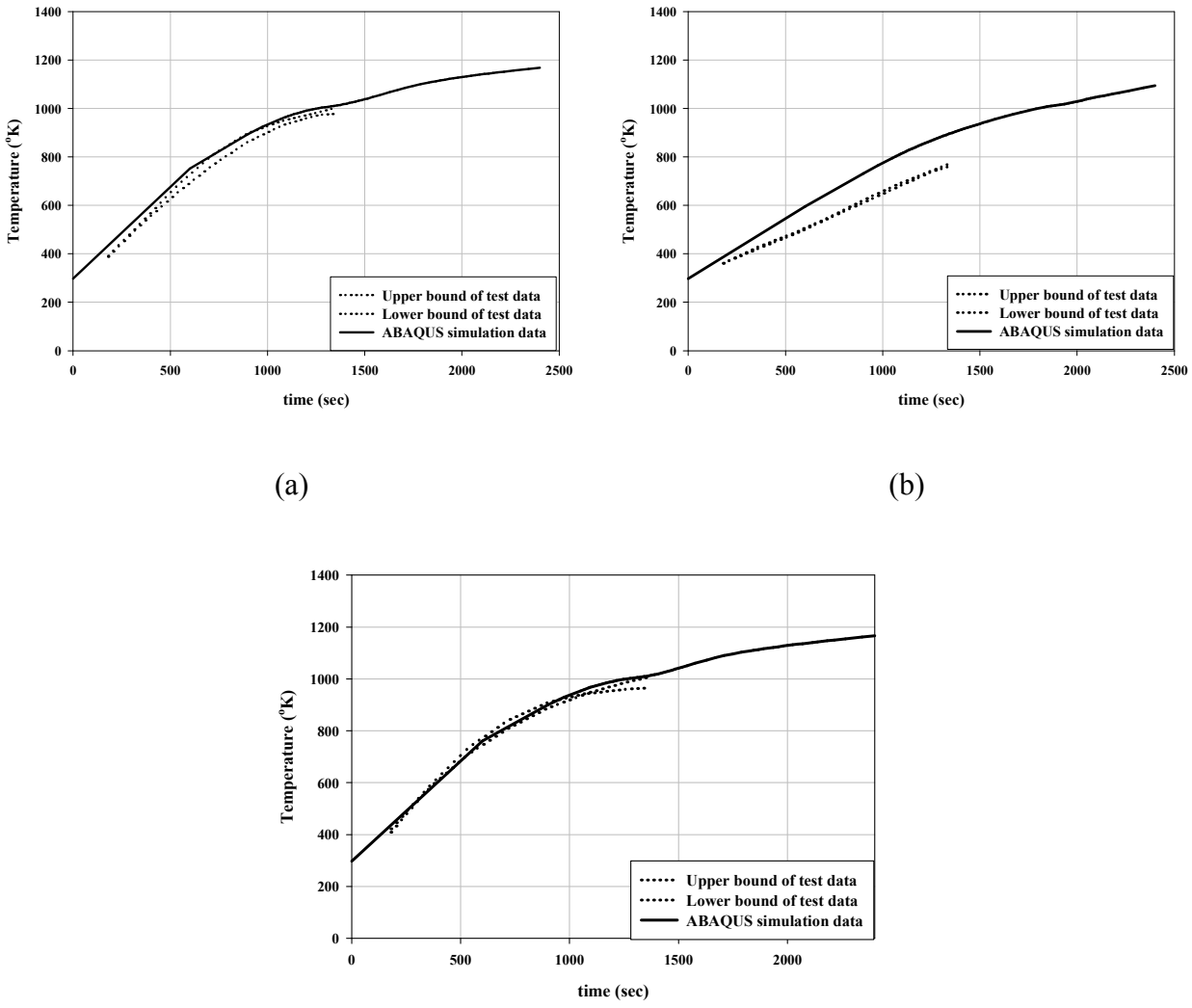

Figure A- 9:Predicted and measured temperature response of a 305 x 165 steel beam a) lower flange, b) upper flange, and c) web when mounted below concrete.

A.4 Conclusions

A radiation exchange model was demonstrated to be capable of predicting the temperature rise of concrete supported by a steel I-beam during a furnace exposure. A simple radiation model was used to determine the dominance of radiation exchange and participating media effects for a range of gas emissivities. Based on expected gas emissivities in a furnace, radiation exchange between the furnace walls and structural elements is the primary contributor to radiation the structural element. If the gas emissivity is increased through soot production

from burning test articles, participating media effects need to be considered. An Abaqus 3D thermal model with radiation exchange was used to predict the temperature response of a structural members under the standard fire condition. The model predictions were within the repeatability error in the experimental results.

A.5 Nomenclature

C Pressure correction

q Heat flux, (W/m^2)

e Emissive power

T Temperature (°K)

A Area (m^2)

F_{k-j} Shape (view) fator for radiation from surface k to surface j

σ Stefan Boltzmann constant ($5.67x10^{-8}$ W/m^2K^4)

ε Emissivity

α Absorptivity

τ Transmissivity

δ_{k-j} Kronecker delta, 1 when k=j

0 when $k \neq j$

ρ Density, (kg/m^3)

c_p Specific heat at constant pressure, (J/kgK)

h Coefficient of convective heat transfer, (W/m^2K)

V Volume, (m^3)

K Conductivity (W/mK)

Δt Time difference

Δx Difference in position

CO_2 Carbon di-oxide

H_2O Water

s Steel

c Concrete

f Furnace

k,j Surface index

i node number

p time increment

b Black body

g Gas

∞ Ambient

r Radiative

o outgoing

A.6 References

[1] ISO-834, 1975, "Fire resistance tests-elements of building construction - Part 1.1: General Requirements for Fire Resistance Testing," International Standard Organization, Geneva, Switzerland.

[2] Kay, T. R., Kirby, B. R., and Preston, R. R., 1996, "Calculation of the heating rate of an unprotected steel member in a standard fire resistance test," Fire Safety Journal, 26(4), pp. 327-350.

[3] Ghojel, J. I., 1998, "A new approach to modeling heat transfer in compartment fires," Fire Safety Journal, 31(3), pp. 227-237.

[4] Wong, M. B., and Ghojel, J. I., 2003, "Sensitivity analysis of heat transfer formulations for insulated structural steel components," Fire Safety Journal, 38(2), pp. 187-201.

[5] Wong, M. B., and Ghojel, J. I., 2003, "Spreadsheet method for temperature calculation of unprotected steelwork subject to fire," The Structural Design of Tall and Special Buildings, 12(2), pp. 83-92.

[6] Hibbitt, Karlsson, and Sorensen, "Abaqus/Standard Version 6.10 EF-1," Hibbitt, Karlsson and Sorensen Inc., Pawtucket, RI.

[7] Cedeno, G. A., Varma, A. H., and Gore, J., "Predicting the Standard Fire Behavior of Composite Steel Beams," R. T. Leon, T. Perea, G. A. Rassati, and J. Lange, eds., ASCE, pp. 53-53.

[8] CEN, 2002, Eurocode 1, Actions on Structures: General actions; actions on structures exposed to fire, European Committee for Standardization, Brussels, Belgium.

[9] Wang, Z.-H., 2010, "Geometric effect of radiative heat exchange in concave structure with application to heating of steel I-sections in fire," International Journal of Heat and Mass Transfer, 53(5–6), pp. 997-1003.

[10] Siegel, R., and Howell, J. R., 2002, Thermal Radiation Heat Transfer, Taylor & Francis.

[11] Lattimer, B. Y., Asaro, R., Ouellette, J., Mealy, C., and Ramroth, B., 2007, "Structural Response of fiber Reinforced Plastic Composites During Fires," The 11th Interflam ConferenceLondon, UK, pp. 653-664.

[12] Wainman, D. E., Kirby, B. R., and British Steel Technical. Swinden, L., 1987, Compendium of U.K. standard fire test data : unprotected structural steel, 1, British Steel Technical, Swinden Laboratories, Rotheram [England].
[13] Institution, B. S., 2001, Eurocode 3: Design of Steel Structures: Part 1.2 General Rules - Structural Fire Design (together with United Kingdom National Application Document), BSI.
[14] Staff, B. S. I., Institution, B. S., and Standardization, E. C. f., 2005, Eurocode 2. Design of Concrete Structures. General Rules. Structural Fire Design, BSI.
[15] 2007, "Thermal ceramics."